SINGLE-PHASE FORCED CONVECTION IN A MICROCHANNEL WITH CARBON NANOTUBES FOR ELECTRONIC COOLING APPLICATIONS

A Thesis
Presented to
The Academic Faculty

by

Carter Reynolds Dietz

In Partial Fulfillment
of the Requirements for the Degree
Master of Science in the
School of Mechanical Engineering

Georgia Institute of Technology
August of 2007

SINGLE-PHASE FORCED CONVECTION IN A MICROCHANNEL WITH CARBON NANOTUBES FOR ELECTRONIC COOLING APPLICATIONS

Approved by:

Dr. Yogendra Joshi, Advisor
School of Mechanical Engineering
Georgia Institute of Technology

Dr. David Gerlach
School of Mechanical Engineering
Georgia Institute of Technology

Dr. Minami Yoda
School of Mechanical Engineering
Georgia Institute of Technology

Dr. Samuel Graham
School of Mechanical Engineering
Georgia Institute of Technology

Date Approved: July 03, 2007

ACKNOWLEDGEMENTS

I wish to thank Dr. Yogendra Joshi, my advisor, for his guidance and support. I also wish to thank Dr. Minami Yoda, Dr. Samuel Graham and Dr. David Gerlach, my three other committee members, for their thoughtful suggestions on various aspects of my research. Finally, I would like to thank Stephan Turano and Jud Ready at GTRI for their involvement in the carbon nanotube growth process, Qihong Nie for his help in constructing and meshing the numerical model, Brent Buchine for his help with obtaining SEM images, Thomas Beechem for his help with Raman spectroscopy measurements and Arnab Choudhury and Zhengchun Peng for their help with manufacturing cover plates from PDMS.

TABLE OF CONTENTS

LIST OF TABLES

LIST OF FIGURES

LIST OF SYMBOLS AND ABBREVIATIONS

Baseline	Devices without carbon nanotubes
C	Gap between tips of CNT array and channel
$c_p{}^w$	Specific heat of water
CNTs	Carbon nanotubes
D_{CNT}	Diameter of a carbon nanotube
D_h	Hydraulic diameter
f	Friction factor
h	Depth of the channel
h^*	Heat transfer convection coefficient
H_c	Optimized height of a fin
H_{CNT}	Average height of an array of CNTs
I	Current
I_{output}	Experimental current output from pressure transmitter
K	Loss coefficient
k_{copper}	Thermal conductivity of the heater
k_{CNT}	Thermal conductivity of CNTs
$k_{silicon}$	Thermal conductivity of silicon
k_{TIM}	Thermal conductivity of the thermal interface material
k^w	Thermal conductivity of water
L	Length of a single channel

$\dot{m}$	Mass flow rate
Nu	Nusselt number
P	Experimentally measured power input to the system
$\Delta P_{channel}$	Pressure drop
ΔP_{total}	Experimental pressure measurement
Pr	Prandtl number
Pr^{w}	Prandtl number for water
q''	Heat flux
Q_{input}	Input heat determined from thermocouple temperature gradient
R_{bulk}	Working fluid resistance
R_{cond}	Conduction resistance
R_{constr}	Constriction resistance
R_{conv}	Convection resistance
R_{loss_1}	Heat loss through insulation
R_{loss_2}	Heat loss from silicon spreading
$R_{microchannel}$	Resistance between silicon surface temperature and inlet fluid temperature
R_{setup}	TIM and copper resistance
R_{TIM}	TIM resistance
R_{Total}	Resistance between backside silicon temperature and inlet fluid temperature
Re	Reynolds number based on hydraulic diameter
S_T	Average pitch of CNT pin-fins
TIM	Thermal interface material

t_{copper}	Thickness of the heater between the thermocouple and TIM
t_f	Width of the channel wall
T_{copper}	Heated region temperature
T_{in}	Inlet water temperature
T_{out}	Outlet water temperature
T_{surf}	Backside silicon temperature
ΔT_{copper}	Heated region temperature rise above ambient
ΔT_{water}	Water temperature rise above ambient
$t_{silicon}$	Thickness of the silicon between the heater and channel surface
t_{TIM}	Thickness of the TIM
$\overline{U}$	Characteristic velocity
V	Voltage
$\overline{V}_{in}$	Average inlet velocity
$V_{\max}$	Maximum velocity between pin-fins
w	Width of a single channel
w_c	Theoretical or optimized width of a single channel
w_w	Optimized width of a fin
$z_{f,d}$	Hydrodynamic entrance length
$z_{h,d}$	Thermal entrance length
α	Aspect ratio
β	Ratio of channel wall width to channel width
η_f	Fin efficiency

ρ^w	Density of water
μ^w	Dynamic viscosity of water
ν^w	Kinematic viscosity of water

SUMMARY

A comparative study was conducted to determine whether it would be advantageous to grow carbon nanotubes on the bottom surface of anisotropically-etched silicon microchannels to facilitate greater heat removal in electronic cooling applications. The effect of the samples was evaluated based on the fluid temperature rise through the channels, the silicon surface temperature increase above ambient, and the pressure drop. The height and deposition pattern of the nanotubes were the parameters investigated in this study. The working fluid, water, was passed through the microchannels at two different volumetric flow rates (16 mL/min and 28 mL/min). Additionally, two different heat fluxes were applied to the backside of the microchannel (10 W/cm^2 and 30 W/cm^2). Extensive validation of the baseline channels was carried out using a numerical model, a resistor network model, and repeatability tests. Finally, the maximum enhancement when using carbon nanotubes under single-phase, laminar, internal, forced convection was investigated using basic principles in regard to the additional surface area created by the carbon nanotubes, as well as their high thermal conductivity. For the devices tested, the samples with carbon nanotubes not only had a higher pressure drop, but also had a higher surface temperature. Therefore, the baseline samples had the best performance. Furthermore, based on a basic principles investigation, the increase to thermal performance gained by increasing the surface area with CNTs is overshadowed by the decrease in mass flow rate for a fixed pressure drop. The analysis suggests that the limiting factor for heat transfer in single-phase, laminar pressure driven flows is not convection heat transfer resistance, but the bulk resistance of the fluid.

CHAPTER 1

INTRODUCTION

1.1 Motivation

According to Moore's Law, the number of transistors on a processor doubles every twelve to eighteen months. Despite initial skepticism of Moore's claim, the semiconductor industry has closely followed this trend. The Dual-Core Intel Itanium 2 processor, the new processor released by Intel, boasts over 1 billion transistors [1]. As the transistor density increases, so does the amount of power dissipated. If heat generated by the transistors is not effectively removed from the vicinity of the chip, chip temperatures will reach destructive values. The International Technology Roadmap for Semiconductors (ITRS) provides both short term and long term power dissipation predictions for high-performance computers. According to these predictions, the power dissipated at the chip level will increase to 65 W/cm^2 from the current value of 61 W/cm^2 within the next five years [2]. The power dissipation then plateaus at a value of 65 W/cm^2 until 2020. This plateau may indicate challenges in effective, low-cost, thermal management techniques. Currently, most cooling techniques for high-performance computers consist of forced air convection through a well-designed heat sink. Due to the thermophysical properties of air, however, forced air convection will no longer be able to effectively dissipate at the chip level the rate of heat predicted to be generated by future processors. Therefore, thermal management of processors is currently of great concern and new cooling techniques are needed to keep pace with the trends for processor power dissipation. Several possible cooling solutions, including two-phase flow, nucleate boiling, stacked microchannel heat exchangers, nanofluids and jet-impingement, have recently been investigated by various authors [3-9]. One proposed method of power

dissipation, for example, incorporates carbon nanotubes (CNTs), an arrangement of carbon atoms with high thermal conductivity, into a silicon microchannel. This silicon microchannel with CNTs removes heat using degassed, de-ionized (DI) water under single-phase, laminar, forced convection conditions. Carbon nanotubes are capable of dramatically increasing the overall surface area within the microchannel due to their small size and high aspect ratio. For consideration, the CNTs are assumed to be 50 nm diameter cylinders, (D_{CNT}), have a height of 120 μm, (H_{CNT}), to grow in a staggered array with a 100 nm pitch, (S_T), and have a clearance of 30 μm, (C), as shown in figure 1. The array of CNTs is enclosed in a rectangular channel that is 4 mm in width, 8.5 mm in length and 150 μm in height. Water is the working fluid and is passed through the channel at a volumetric flow rate of 230 mL/min. Water is assumed to have constant properties, taken at 300 K, and wet the CNTs. The Reynolds number is calculated from equation 1.

$$\mathrm{Re} = \frac{V_{\max} \cdot D_{CNT}}{\nu^{w}} \tag{1}$$

$$V_{\max} = \overline{V}_{in} \cdot \frac{S_T \cdot (H_{CNT} + C)}{[S_T \cdot (H_{CNT} + C) - D_{CNT} \cdot H_{CNT}]} \tag{2}$$

Under these conditions, Re is equal to 0.6 and the flow with be in the Stokes regime. The Hilpert correlation, equation 3, is used to determine the average Nusselt number for a cylinder body in Stokes flow. Assuming that the average Nusselt number for a single cylinder body can be used to represent an entire array of cylinders with the aforementioned geometry, the Nusselt number is equal to 1.5.

$$Nu = 0.989 \cdot \mathrm{Re}^{0.33} \cdot \mathrm{Pr}^{1/3} \tag{3}$$

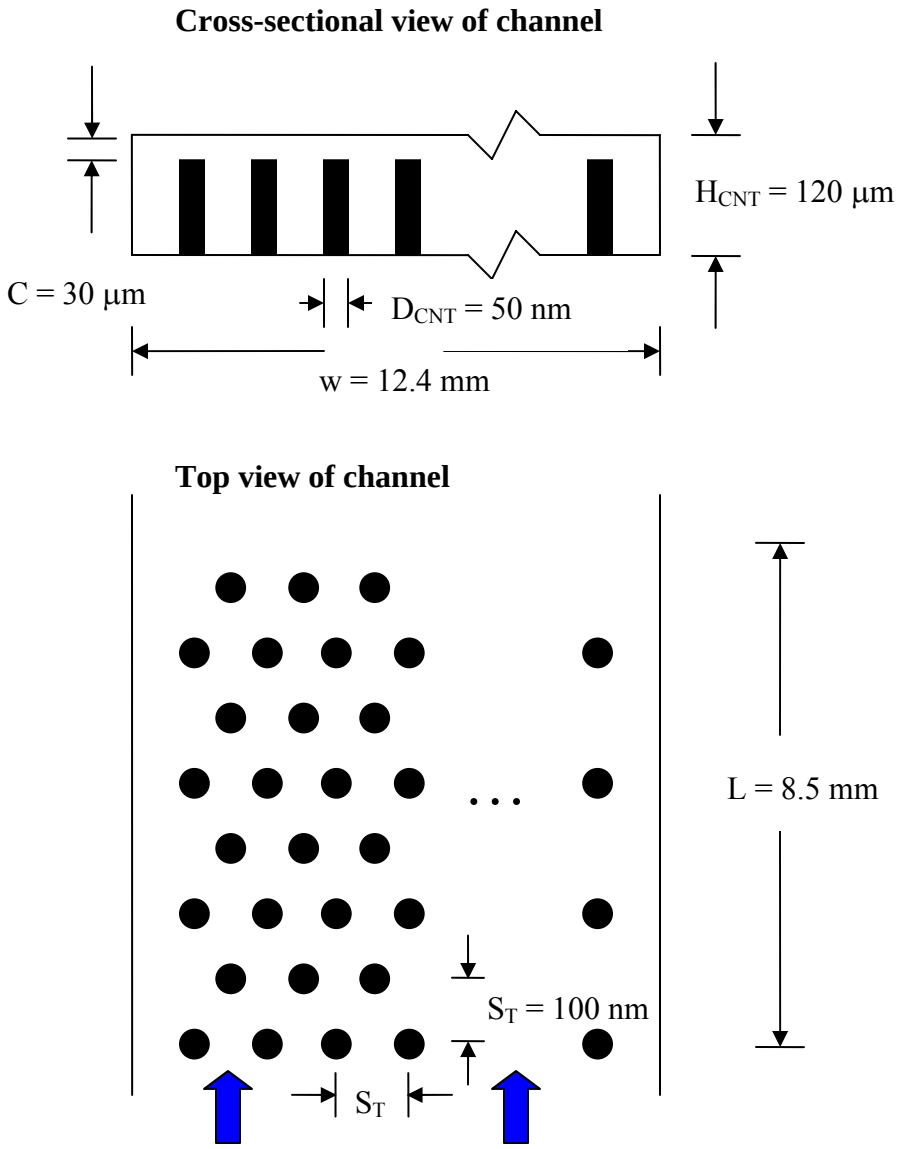

Figure 1: CNT channel geometry

The convective coefficient of heat transfer, calculated from equation 4, is then equal to $1.9*10^7$ $Wm^{-2}K^{-1}$. In comparison, a channel without pin-fins, but with the same overall dimensions (length of 8.5 mm, width of 4 mm and height of 150 μm) and the same flow rate, would have a convective coefficient of heat transfer of $1.1*10^4$ $Wm^{-2}K^{-1}$.

$$h^* = \frac{Nu \cdot k^w}{D_{CNT}} \tag{4}$$

The addition of CNTs potentially could increase the convective coefficient by three orders of magnitude. Therefore, based on this first-order analysis, it is hypothesized that carbon nanotubes will increase the heat removal from the vicinity of the chip compared to the heat removal without carbon nanotubes.

1.2 Literature review

1.2.1 Review of microchannel concepts

Standard semiconductor fabrication techniques were applied to construct the first silicon microchannels in the 1980's. In 1981, Tuckerman and Pease used silicon microchannels, with water as the working fluid, to dissipate power from an electronic chip. The microchannels were etched in a silicon sample with an overall dimension of 1 cm^2. They had a channel width of approximately 60 μm and a parameterized channel height varying between 287 μm and 376 μm. These microchannels effectively dissipated up to 790 W/cm^2 while maintaining a chip temperature below 110 °C [10]. The small characteristic length scale of silicon microchannels prompted the scientific community to investigate the possibility of new transport physics.

Several experimental investigations were then conducted to determine the friction factor and the Nusselt number inside microchannels. The results were often inconsistent. Wu and Little, who studied gas flow inside glass and silicon microchannels with depths between 30 to 60 μm, reported that friction factors exceeded classical behavior for both laminar and turbulent flows and the transition to turbulent flow began at lower Reynolds' numbers, approximately between 400 and 900 [11]. On the other hand, Pfahler et al. studied both gas (nitrogen and helium) and liquid (isopropyl and silicone oil) flow inside silicon microchannels and determined that laminar theory over-predicted the friction factor and that different fluids had different friction factor dependencies on the channel size [12]. Peng et al., who examined water inside rectangular microchannels machined in

stainless steel, found that depending on the channel geometry, classical theory would either over or under predict the friction factor and convective heat transfer coefficient [13]. Peng et al. also agreed with Wu and Little's conclusion that transition to turbulent flow occurred at much lower Reynolds' numbers than predicted by classical theory.

Recent publications contradict earlier studies, suggesting that flow inside microchannels still obey the Navier-Stokes equations. The reported discrepancies can be attributed to either uncertainties in the channel geometry, errors in calculations or measurements as a result of ignoring entrance and exit effects, or inappropriate use of correlations. In 2000, Xu et al. investigated microchannels machined in aluminum with hydraulic diameters between 30 and 350 μm and water as the working fluid [14]. The authors reported that the experimental data were in good agreement with the Navier-Stokes equations as long as the hydraulic diameter was larger than 30 μm. Lee, Garimella and Liu investigated heat transfer and pressure drop in microchannels with de-ionized water as the working fluid for various Reynolds numbers and hydraulic diameters [15, 16]. Their work also confirms the applicability of the Navier-Stokes equations to microchannels and demonstrates that the onset of transitional flow occurs at Reynolds numbers comparable to macro-scale flows. Both [15] and [16] showed good agreement between numerical modeling, experimental results and conventional theory.

1.2.2 Review of carbon nanotube concepts

Carbon nanotubes (CNTs) were discovered in 1991 by Sumio Iijima [17]. CNTs are a particular arrangement of carbon atoms similar in structure to graphene, a two dimensional counterpart of graphite. A CNT is formed when the two-dimensional sheet of graphene is rolled into a seamless cylinder. CNTs can range from ~1 nm to ~100 nm in diameter and have lengths in the micrometer range. Based on the chemical arrangement of carbon atoms, a discrete number of unique CNTs can be formed. Normally, these different types of CNTs are classified by their chiral vector as displayed

in figure 2, which is adopted from a figure in [18]. The chiral vector is related to the circumference of the nanotube, and based on the chiral vector, the nanotubes are categorized as either semi-conducting or metallic. CNTs can also be classified as either single-walled, double-walled or multi-walled. A single-walled CNT is formed by a rolling a single sheet of graphene into a cylinder. Double-walled and multi-walled CNTs are formed by forming concentric cylinders from multiple layers of graphene. Dresselhaus provides a very detailed description of the chemical arrangement of CNTs as well as the phonon transport and related thermophysical properties [18].

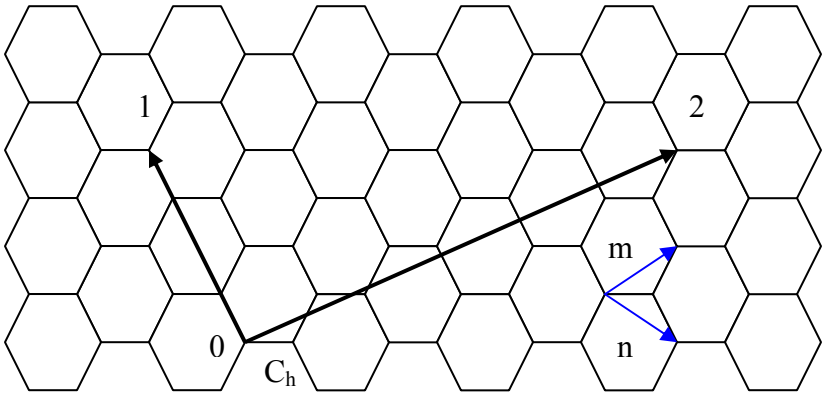

Figure 2: CNT chiral vector
The vertices of the hexagons represent carbon atoms. The chiral vector, labeled C_h, points from 0 to 2. The CNT axis is along the line passing through points 0 and 1. The above CNT is classified as a <5,1> CNT based on the magnitudes of the lattice vectors m and n.

As a result of the unique geometry of CNTs, these structures have excellent electrical, mechanical and thermal properties, as well as desirable chemical and optical properties. In 1999, Hone et al. published theoretical predictions for the thermal conductivity of individual single-walled CNTs [19]. By experimentally measuring the thermal conductivity of a low density mat of carbon nanotubes, Hone extrapolated the thermal conductivity of a single nanotube and placed the value between 1800 and 6000 $Wm^{-1}K^{-1}$ at room temperature. Hone also predicted that a dense mat of single-wall CNTs would have a bulk averaged thermal conductivity around 36 $Wm^{-1}K^{-1}$.

The initial theoretical predictions made by Hone were followed up by equilibrium and non-equilibrium molecular dynamics simulations. Due to the large phonon free mean path in CNTs, Berber et al. showed the thermal conductivity of a CNT to be around 6000 $Wm^{-1}K^{-1}$ at room temperature [20]. In 2002, Hone et al. published experimental results for the thermal conductivity of a dense mat of aligned single-wall CNTs and found the bulk averaged thermal conductivity to be over 200 $Wm^{-1}K^{-1}$, which is greater than originally predicted [21]. Fujii et al. experimentally measured individual single-walled CNTs and found that the thermal conductivity was a function of the nanotube diameter [22]. The authors report that the thermal conductivity at room temperature is above 2000 $Wm^{-1}K^{-1}$.

Overall, there is a great deal of inconsistency regarding the exact value of thermal conductivity for both a single CNT and a mat of CNTs. The inconsistencies can be attributed to difficulties with CNT growth as well as experimental error. Copper, silver and gold, which are some of the best known thermally conductive materials, have thermal conductivities of 400 $Wm^{-1}K^{-1}$, 430 $Wm^{-1}K^{-1}$ and 320 $Wm^{-1}K^{-1}$ at room temperature, respectively [23]. According to [24] and [25], the thermal conductivity of these materials has been shown to decrease as the geometric size approaches the free mean path of the dominate heat carrier, i.e. electrons. Therefore, the literature does support (although it is inconclusive regarding an exact value) that CNTs have an axial thermal conductivity that is greater than other materials at these length scales [26-28]. The thermal conductivity of individual CNTs is comparable to other arrangements of carbon atoms such as in-plane graphite and diamond, which have thermal conductivities of 1950 $Wm^{-1}K^{-1}$ and 2300 $Wm^{-1}K^{-1}$, respectively [23]. Yet, CNTs exist on a much smaller length scale than graphite and diamond.

1.2.3 Review of carbon nanotubes grown in microchannels

At the time of the current study, only a few publications were available regarding CNTs grown inside silicon channels. In 2004, Jakaboski et al. compared devices with CNTs grown on the bottom surface of silicon microchannels and geometrically similar devices without CNTs [29]. The investigation was for single-phase, forced convection with DI water as the working fluid. An experimental study was performed in which the number of channels, hydraulic diameter and the density of CNT deposition were varied. The authors showed that for a laminar flow, the devices with CNTs have a faster thermal response during the transient phases of the experiments, and they also provide a lower steady-state surface temperature. However, no difference was noted between the CNT density deposition and the hydraulic diameters of the channels. Another single-phase heat transfer study in 2005 by Mo et al. showed that CNTs increase thermal performance [30, 31]. In this study, the devices with CNTs were able to dissipate a greater heat load, while maintaining the chip at a lower operating temperature. A fixed pressure drop of 9000 Pa was used, and the flow rate for devices with CNTs was shown to decrease.

Unfortunately, the published results are not conclusive. The results from [29] could be explained by experimental uncertainty and device design. The samples were manufactured so that each silicon device consisted of two separate test samples. One side of the silicon device had the first test sample, which consisted of 6 channels of a given geometry. The other side of the silicon device had a second test sample with 8 channels and a different hydraulic diameter from the first set. The silicon device could be rotated 180° so that both test samples could be tested individually; however, nothing prevented heat and water from flowing into both test samples during the experiments. This could account for why there were no differences observed between the two different test devices. To further investigate the conclusions made in [29], a CNT sample that was previously used in [29] was examined using a scanning electron microscope (SEM). Several of the CNT devices had formation of black silicon (see figure 3), which could

alter the results due to dramatic changes in the surface roughness. The results listed in [30, 31] are also misleading. Although the presence of CNTs were clearly having a thermal impact on the experimental studies, the results could be attributed to how the devices with CNTs and the devices without CNTs were compared. The authors propose that by replacing silicon fins (channel walls) in microchannels with fins formed from CNTs, a thermal enhancement can be achieved. The comparison, however, was done between a device that had CNT fins and a device without any fins, rather than a device with silicon fins. Therefore, the increased heat transfer could be largely attributed to the smaller hydraulic diameter rather than the surface area increase from the CNTs. A comparison between devices with channel walls made of CNTs and devices with channel walls made from silicon is needed to determine if CNTs provide any benefit.

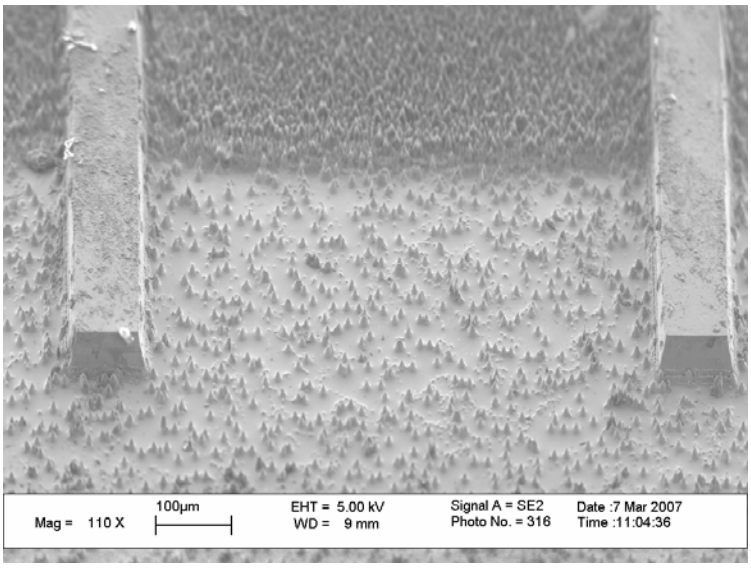

Figure 3: Formation of black silicon

Aside from the previously mentioned works, a few other studies have been conducted with CNTs inside microchannels. Gjerde et al., in 2005, used an electric field to control the growth of CNTs inside a microchannel [32]. The channels were 5 μm in depth, and CNTs were approximately 1 μm in height. A possible fluidic application, in which the CNTs could be used as a check valve, was mentioned, but no experimental

results have been published at this time. In 2006, Joseph et al. examined slip lengths of water in CNT microchannels [33]. The slip length can be amplified by a highly rough, hydrophobic, porous medium, which according to the authors, is exemplified by a CNT array. The authors used a micro particle image velocimetry technique to determine the slip length, which was found to be between 1 and 6 μm. Finally, Stadermann et al. performed an investigation using CNTs inside a microchannel for gas chromatography purposes [34]. Their work showed that the CNT devices were able to separate four-compound test mixtures in less than 1 second. The authors also reported no differences in the height of the CNTs when grown with a chemical vapor deposition process between CNTs grown on a flat substrate and CNTs grown inside a 100 μm deep microchannel.

CHAPTER 2

EXPERIMENTAL DESIGN

2.1 Device design

The devices were originally designed in AutoCAD, shown in figure 4, to create a template for further fabrication on a 100 mm diameter silicon wafer. Each device consists of two plena and three channels. The channels measure 4 mm in width, 8.5 mm in length and 0.150 mm in height. The length and width were determined so that the total surface area would be approximately 1 cm^2, which is the typical dimension of a chip. The channel length was chosen to be much larger than the width in order to ensure that the flow becomes fully developed, both hydrodynamically and thermally. Based on [35, 36], equations 5 and 6 give the hydrodynamic and thermal entry lengths for parallel-plate geometry with an asymmetric heat flux and Prandtl number greater than 3.

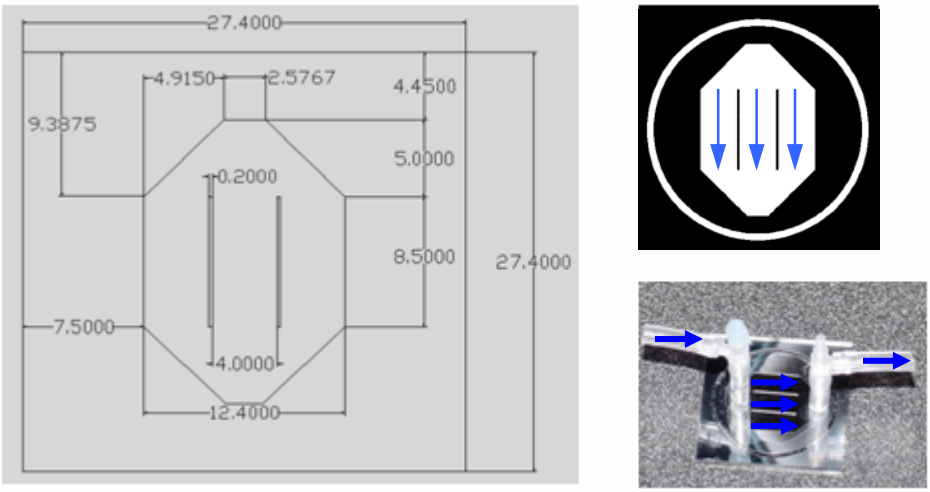

Figure 4: AutoCAD schematic and picture of silicon device
The figure on the left is a schematic of the device. All dimensions are in mm. The figure on the upper right is a template of the device where the white regions are recessed 150 μm into the silicon. The blue arrows represent the flow path of the fluid. The figure on the bottom right is a completed device. The cover plate and the inlet and outlet ports are shown.

$$z_{f,d} = 0.011 \cdot D_h \cdot \mathrm{Re} \quad (5)$$

$$z_{h,d} = 0.011 \cdot D_h \cdot \mathrm{Re} \cdot \mathrm{Pr} \quad (6)$$

For the current channel geometry and the investigated flow rates, the flow will be hydrodynamically fully developed at a maximum distance of 0.28 mm downstream of the entrance (3% of the channel length) and thermally fully developed at a maximum distance of 1.9 mm from the entrance (22% of the channel length).

The assumption of parallel plates is valid if the aspect ratio, the ratio of channel height to channel width, is less than 0.1 [35, 36]. The channels were specifically designed to have a low aspect ratio to avoid possible complications caused by high aspect ratio channels, mainly an increase in flow resistance for the gases during the CNT growth process. In addition, a low aspect ratio permits CNT growth over a large amount of channel surface area, allowing for a greater measurable difference between the samples without CNTs and the samples with CNTs.

To complete the microchannels, a cover plate was attached on top to seal the channels. The fluid is brought into the channels through ports created in the cover plate. Because a cover plate must be attached, a significant amount of silicon was left around the channels and plena to allow enough surface area for bonding. The area needed for bonding imposed a lower limit on the overall device geometry, while the size of the furnace used to grow the CNTs set the upper limit. With these specified dimensions, four devices were manufactured on the same 100 mm diameter silicon wafer.

2.2 Microfabrication outline

Most of the device fabrication was conducted at the Microelectronics Research Center (MiRC) a class 10 clean room at the Georgia Institute of Technology. The remaining fabrication was done in the Manufacturing Related Discipline Complex II building (a.k.a. the J. Erskine Love, Jr. Building) in the Micro Thermal Systems lab, in the Thermal Management and Metrology of MEMS Devices lab and at the Georgia

Technology Research Institute (GTRI). Table 1 shows an overview of the entire process for device fabrication, where the italicized steps are only for the devices with CNTs. Figure 5 pictorially represents each process step. Details for the entire microfabrication process can be found in Appendix A.

Table 1: Fabrication outline

Step Number	**Process**
1	RCA Clean I and II
2	PECVD Oxide Deposition 1
3	Photolithography 1
4	ICP Oxide Etch 1
5	Resist Removal and RCA Clean II
6	Anisotropic ICP Silicon Etch
7	Descum and HF Dip
8	*PECVD Oxide Deposition 2*
9	*Photolithography 2*
10	*ICP Oxide Etch 2*
11	*Resist Removal*
12	*Photolithography 3*
13	*Metallization*
14	*Lift-Off*
15	Wafer Dicing
16	*CNT Growth*
17	Cover Plate Bonding

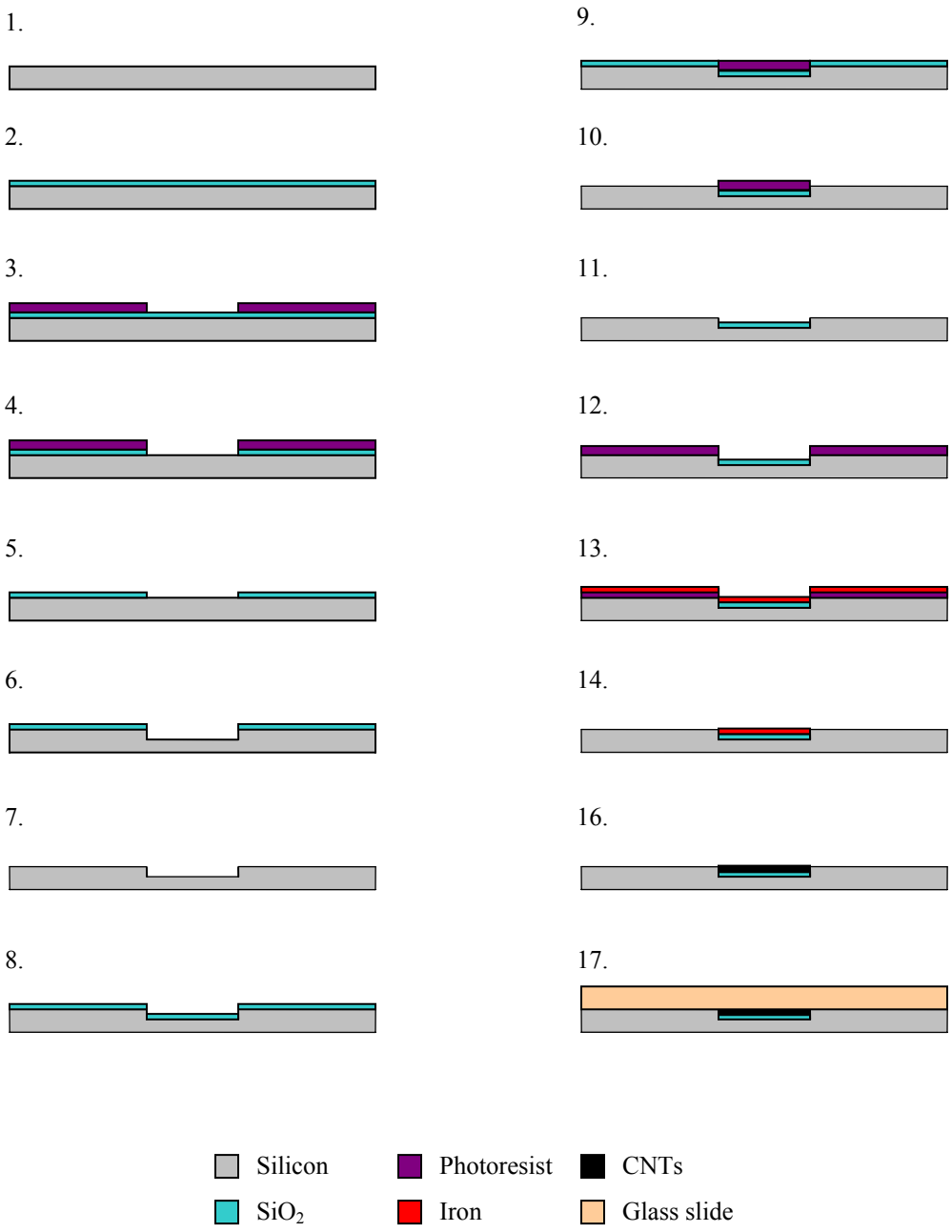

Figure 5: Fabrication outline

A cartoon of the fabrication process is given. The step numbers are in reference to the descriptions given in table 1. Both baseline silicon devices and CNT device underwent the first seven processing steps. Essentially, the first seven steps transfer the channel template, shown in figure 4, to a silicon wafer. Steps 8 through 16 are only for the devices with CNTs. In these steps, 500 nm of silicon dioxide is selectively deposited on the bottom of the silicon channels. Then, 10 nm of iron is selectively deposited directly on top of the silicon dioxide. The CNT growth, step 16, is carried out at elevated temperatures and in the presence of simple hydrocarbon gases.

2.3 Test parameters

There are a total of four parameters investigated in this study: heat flux, flow rate, CNT height and CNT deposition pattern. Two values of the heat flux (10 W/cm^2 and 30 W/cm^2) and two values of the volumetric flow rate (16 mL/min and 28 mL/min) were chosen. CNT height was not able to be investigated systematically because consistent CNT growth was never obtained through the course of this investigation. Further details on the height inconsistency are outlined in section 3.1.1. The evaluated CNT heights were determined based on the growth obtained with the CNT furnace. The final parameter, CNT deposition pattern, has two testing conditions. The first CNT deposition pattern has complete coverage of the bottom surface of the channel and the second testing condition has CNTs partially covering the bottom surface of the channel. For the partially covered CNT devices, the CNTs are patterned into two thin strips, 1 mm in width, and extend the entire length of the channel. The thin strips of CNT coverage are evenly spaced between the channel walls and between each other, and their coverage is 50% of the bottom channel surface area. Figure 6 pictorially represents the coverage area of the CNTs. From the combination of the various parameters, 16 unique testing conditions were analyzed.

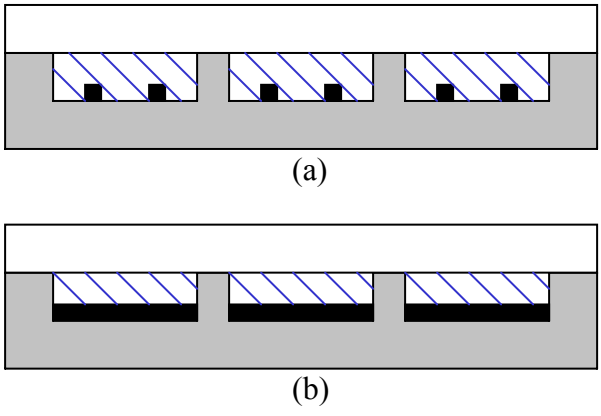

Figure 6: CNT surface coverage
6.a shows a cross section of the microchannels and the corresponding CNT coverage area, represented in black, for the partial CNT deposition pattern. 6.b shows the CNT coverage for the full CNT deposition pattern. The regions hatched in blue represent the working fluid.

2.4 Experimental setup

2.4.1 Test fixture

The test fixture was machined from a clear 12.7 mm (0.5 in) thick polycarbonate sheet ordered from McMaster-Carr to be 76.2 mm by 76.2 mm (3 in by 3 in). Figure 7 is a schematic of the test fixture. A square hole, 19.05 mm by 19.05 mm (0.75 in by 0.75 in), was machined in the center of the plastic to clear a path for the heater.

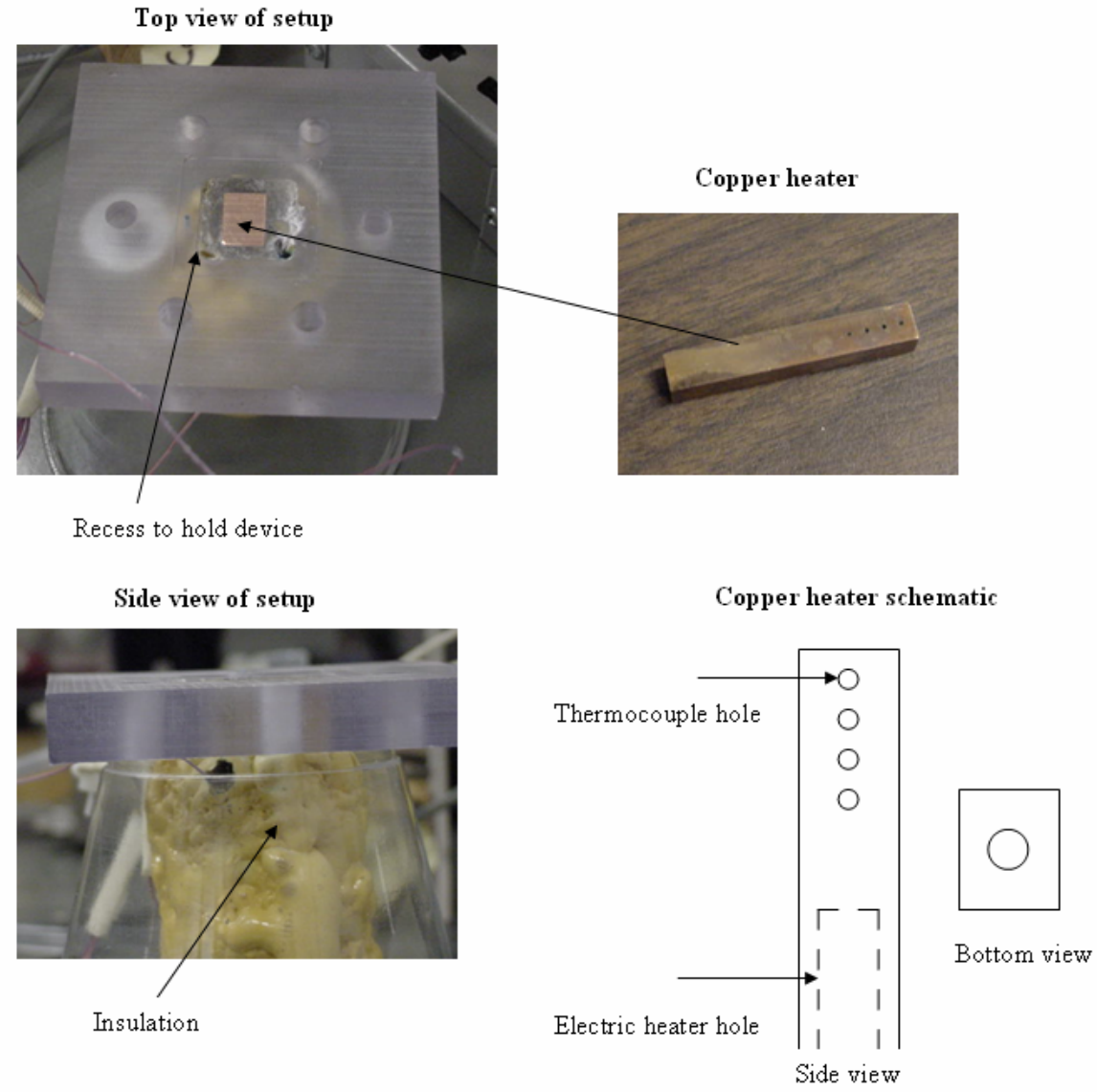

Figure 7: Test fixture schematic

Then, a square recess was created on the top face of the test fixture so that the microchannel could be accurately and repeatedly placed on the heater. The groove was 0.5 mm (0.02 in) in depth and had a cross-sectional area equal to that of the chip (27.6 mm^2). The heater consisted of a cartridge heater ordered from Omega and a machined block of copper 145 ordered from McMaster-Carr. The cartridge heater was 6.35 mm (0.25 in) in diameter and 31.75 mm (1.25 in) in length and was connected to an AC power supply with an adjustable voltage output, ranging from 0 to 140 V. The copper was machined to a length of 76.2 mm (3 in) with a cross-sectional area equal to that of the channel geometry (8.5 mm by 12.4 mm). A 6.35 mm (0.25 in) diameter hole, 31.75 mm (1.25 in) in depth, was drilled in one end of the copper block, and the cartridge heater was inserted into the hole after it had been covered with a boron nitride thermal interface material (TIM) ordered from Chromalox. Four holes, 0.78 mm (0.03125 in) in diameter, were drilled into the copper block at the end opposite of the cartridge heater and along the centerline of the 12.4 mm face. The holes were placed at a spacing of 3.81 mm (0.15 in), with an initial offset from the tip of the heater also equal to 3.81 mm.

Four calibrated type-T thermocouples were initially coated in the Chromalox TIM and then individually inserted into one of the four holes. The thermocouple holes in the copper were then filled with a thermally-conductive, but electrically insulated, two-part epoxy ordered from McMaster-Carr. The thermocouple closest to the tip of the copper provided an approximate surface temperature measurement. This measurement was used as the surface temperature because it yielded a lower experimental uncertainty compared to extrapolating the actual surface temperature. The measurement of this thermocouple is referred to as the heated region temperature. After the epoxy set, a glass slide, cut to the dimensions of a sample, was placed in the recess in the polycarbonate. The polycarbonate test fixture frame was turned upside down so that the glass slide was flat on a table and the polycarbonate block rested on the glass slide. The copper block was inserted into the rectangular hole in the polycarbonate block so that the tip of the copper

block was flush against the glass slide. The entire copper block was then insulated by coating it in polyurethane foam ordered from McMaster-Carr. The glass slide was removed before the insulation fully set. Finally, the square recess in the test fixture for the sample was re-machined so that the copper block, insulation and recess were flush. The alignment between the heater and the device was visually inspected and determined to be satisfactory.

2.4.2 Flow-loop design

An open flow-loop design was employed so that the water would not be contaminated if the CNTs detached from the surface of the microchannel during the experiment. The overall flow loop design can be seen in figure 8, where all the piping consisted of 3.18 mm (0.125 in) inner diameter Tygon tubing ordered from McMaster-Carr. The water was initially contained in a reservoir and was pumped through the setup using a Masterflex peristaltic pump from Cole-Parmer. Due to the strong pulsation of the flow, the water was passed through a pulse dampener. Then, a Rotameter from Cole-Parmer measured the flow rate.

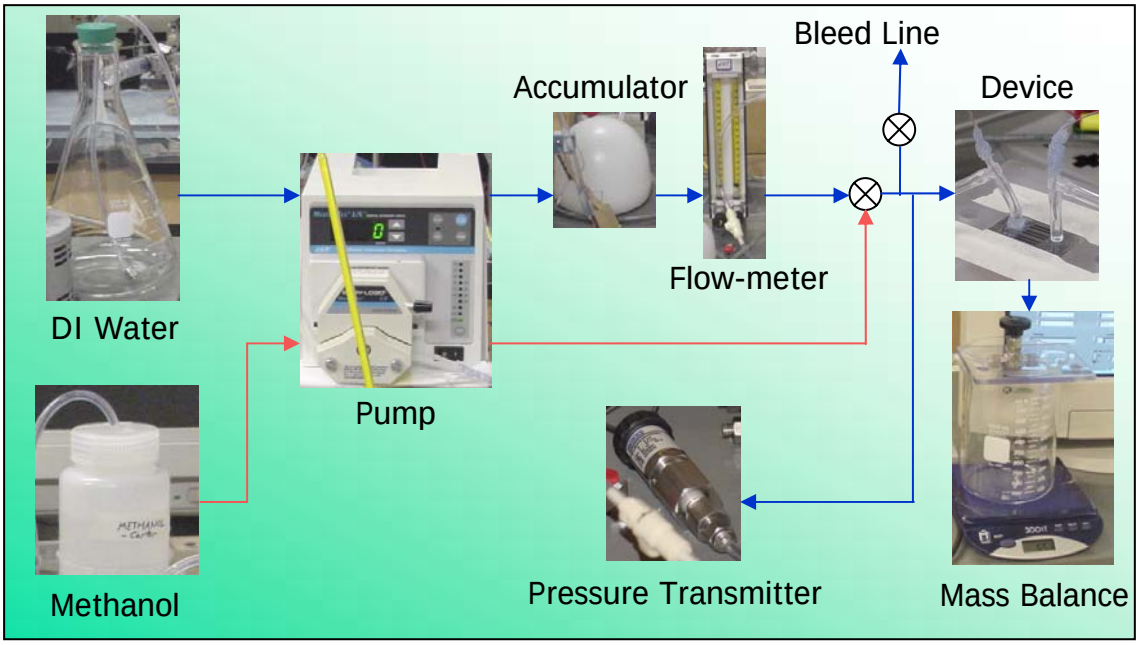

Figure 8: Flow-loop schematic

Following the flow meter, a series of valves ordered from Swagelok were placed in the flow-loop for several reasons. Due to the large surface tension of water, air bubbles can become trapped inside the microchannel and the pressure head required to remove them is too large for the pump to supply. As a result, methanol was initially passed through the setup to remove any bubbles. In order to prevent methanol from flowing through the pulse dampener and the flow meter, a three-way (two inlets, one outlet) ball valve was inserted in the flow path so that either water or methanol could flow through the setup. After the outlet to the three-way ball valve, water was split into two paths with a tee-junction connector. One path was a bleed line and was controlled by a toggle valve, and the other path led to the test fixture and was controlled by a needle valve. Before water entered the sample, a gauge pressure transmitter from Wika with a range of 0 to 34.5 kPa (0 to 7.5 psi) was connected to a second tee-junction in the flow loop. Water then passed through the testing sample and was collected in a beaker. Since the flow-loop was open, the outlet pressure was equal to atmospheric, and consequently, the pressure transmitter reading was also a differential reading.

2.4.3 Testing procedure

DI water was collected in a flask and hooked up to a vacuum pump. The vacuum pump was run for fifteen minutes, to degas the water, because the solubility of air in water decreases with decreasing pressure. However, since the pressure inside the flask was decreasing, the temperature of the water decreased below that of ambient conditions. Therefore, the water was left under vacuum until it reached thermal equilibrium with the environment. As the water was under vacuum, an ice bath was made by combining shaved DI ice and DI water in a heavily insulated coffee mug. The ice bath was used as the constant reference temperature for the thermocouple measurements. The temperature of the ice bath was monitored with a mercury thermometer. The copper heater was then uniformly covered with a 70 μm thick layer of Omegatherm 201, a TIM, ordered from

Omega. The silicon device was placed into a square recess in the polycarbonate block and was taped to the block to minimize the TIM thickness. The inlet tube to the pump was placed in the degassed, DI water and the pump was turned on. The flow rate and the heater were then set to the specified values for that particular experiment. The data acquisition software was started, and data was recorded for five minutes as the water and ice bath reached steady-state. After the initial five minutes, the next ten minutes were spent collecting water in a beaker to measure the mass flow rate. The mass flow rate was measured to limit the uncertainty of the Rotameter, which is discussed in Appendix B. The heater was then turned on, and data was recorded for forty minutes. After forty minutes, the data acquisition software was stopped, and the heater and pump were turned off.

2.5 Data acquisition

2.5.1 Hardware setup and calibration

All experimental measurements were made with Agilent's 34970A data acquisition unit. The diagnostic equipment was wired to an Agilent 34901A multiplexer card for data acquisition. The multiplexer card has 22 separate channels where channels 1 through 20 measure voltages and channels 21 and 22 are designated to measure current. The acquisition unit was interfaced through LabView, which was run on a desktop computer connected to the acquisition unit by a 10833B general purpose interface bus (GPIB) cable also from Agilent. 40 AWG type-T thermocouples were used for all temperature measurements in this study. The thermocouples were calibrated with Omega's CL122 resistive temperature detector (RTD). The RTD has a digital readout resolution of 0.1 °C and has both a cold and hot source for calibrating between -30 and 700 °C. Two sets of thermocouples were calibrated. The first set consisted of the four thermocouples used to measure the temperature inside the copper block. The second set

consisted of two thermocouples measuring the inlet and outlet fluid temperatures and the thermocouple measuring the ambient.

Before the thermocouples were calibrated, they were wired to the multiplexer. The leads on the multiplexer card are copper, so if a type-T thermocouple is directly wired to the multiplexer card, the measured temperature is the temperature difference between the welded junction and the multiplexer card, which is the reference temperature. The multiplexer card has an embedded thermocouple and the data acquisition unit automatically compensates for the temperature at the multiplexer. However, in order to minimize the uncertainty, an ice-bath consisting of shaved DI ice and DI water was used as the junction reference temperature. The thermocouple wiring can be seen in figure 9, where the thicker lines represent 24 AWG type-T thermocouple wire and the thinner lines represent 40 AWG type-T thermocouple wire. Next, each set of thermocouples were calibrated at intervals of 5 °C, between 0 and 95 °C. A calibration curve was then generated.

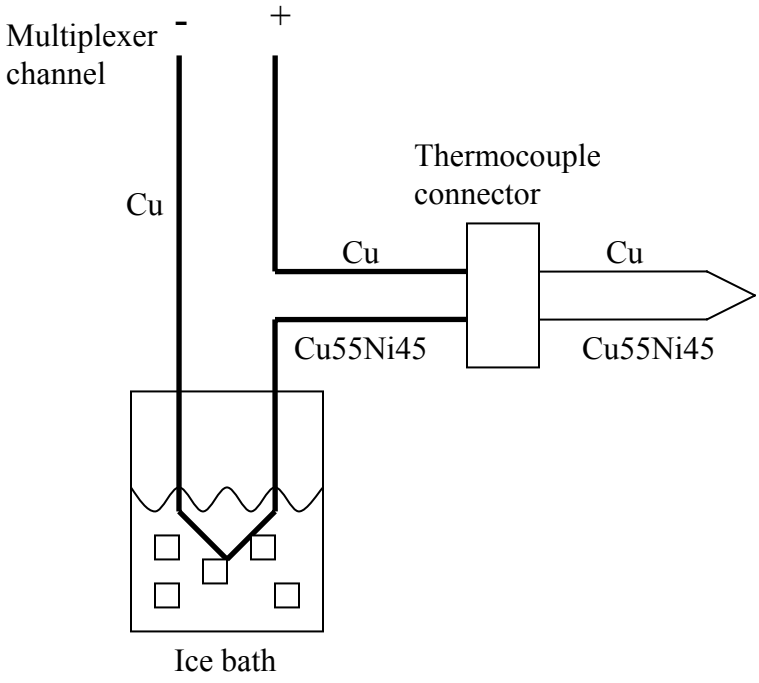

Figure 9: Thermocouple wiring

The pressure transducer was calibrated using Omega's DP1610 high accuracy pressure calibrator. Piping was used to directly connect the pressure transmitter to the pressure calibrator. The pressure transmitter has a linear compensator and a current output. Therefore, any change in pressure is linearly proportional to a change in the current output, and two calibrated points are needed to uniquely determine the calibration curve. The transmitter also has two potentiometers which can be adjusted to define these two points. The calibrator was first set to 0 Pa gauge pressure, and one potentiometer was adjusted so that the current output was 4 mA. The calibrator was then set to a 34.5 kPa (5 psi) gauge pressure, and the second potentiometer was adjusted so that the current output was 20 mA. The linearity of the pressure transmitter was checked by adjusting the calibrator to arbitrary pressures between 0 and 34.5 kPa (5 psi). The calibration curve is given by equation 7, where ΔP_{total} is in psi.

$$\Delta P_{total} = \frac{(5-0)psi}{(0.020-0.004)A} \cdot \left(I_{output} - 0.004\right)A \tag{7}$$

In order to determine the power delivered to the cartridge heater, the root-mean-squared current and voltage were simultaneously measured, as shown in figure 10, and determined by equation 8.

$$P = V \cdot I \tag{8}$$

As seen in figure 10, the voltage leads were connected to channel 12, and the current leads were connected to channel 21 of the multiplexer card. Finally, it should be noted that the flow meter readout was factory correlated, and therefore, no electronic calibration was possible.

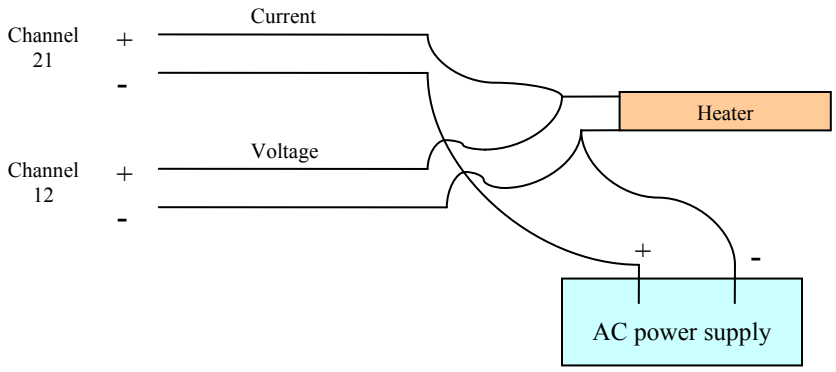

Figure 10: Electric power measurement wiring

2.5.2 Software

LabView was used to record all the relevant experimental measurements. The LabView block diagram, as well as the graphics interface, can be seen in figure 11. LabView received a voltage reading from the type-T thermocouples and then converted that reading to a temperature reading using a seventh order polynomial. The coefficients for the polynomial are given in table 2, where A_0 is the coefficient of the zeroth-order term and A_7 is the coefficient of the seventh-order term. The raw temperature output from the seventh-order polynomial was then adjusted with another subroutine based on the linear calibration that was done previously. The calibrated temperature was plotted in real time for the duration of the experimental run. A final subroutine in LabView was used to calculate and graph the temperature differences between the thermocouples imbedded in the copper block, as well as the temperature difference between the thermocouples measuring the inlet and outlet fluid temperatures. LabView also recorded the root-mean-squared current and voltage supplied to the cartridge heater from the AC power supply. Finally, LabView received a current input from the pressure transmitter, and using the linear calibration curve for the pressure transmitter as determined previously, the pressure was recorded. All the data measurements were recorded continuously at 4.5 second intervals until the software was manually terminated. Finally, the data was output in tabular form to an Excel spreadsheet.

Table 2: Voltage to temperature conversion coefficients

Coefficient (A_n)	Numerical Value (K-V^{-n})
A_0	0.10086091
A_1	25727.94369
A_2	-767345.8295
A_3	78025595.81
A_4	-9247486589
A_5	697688000000
A_6	-26619200000000
A_7	394078000000000

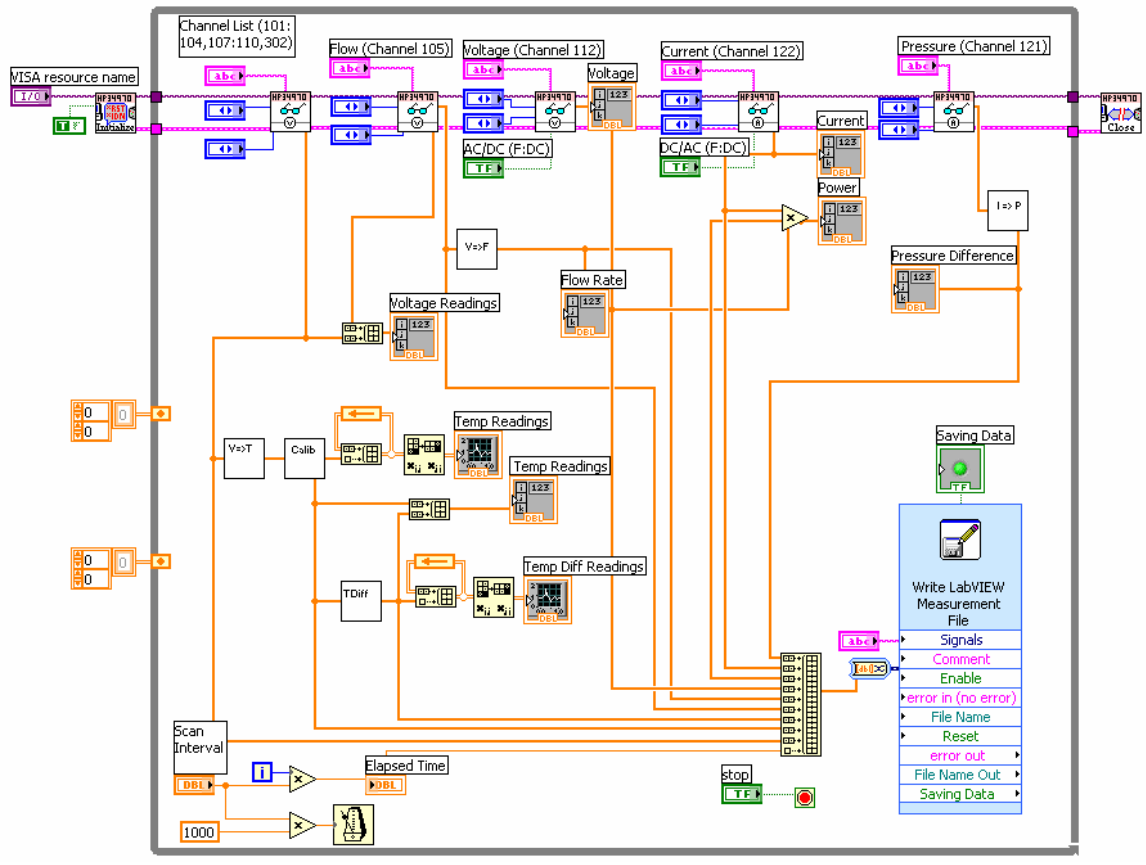

Figure 11: LabView data acquisition diagrams

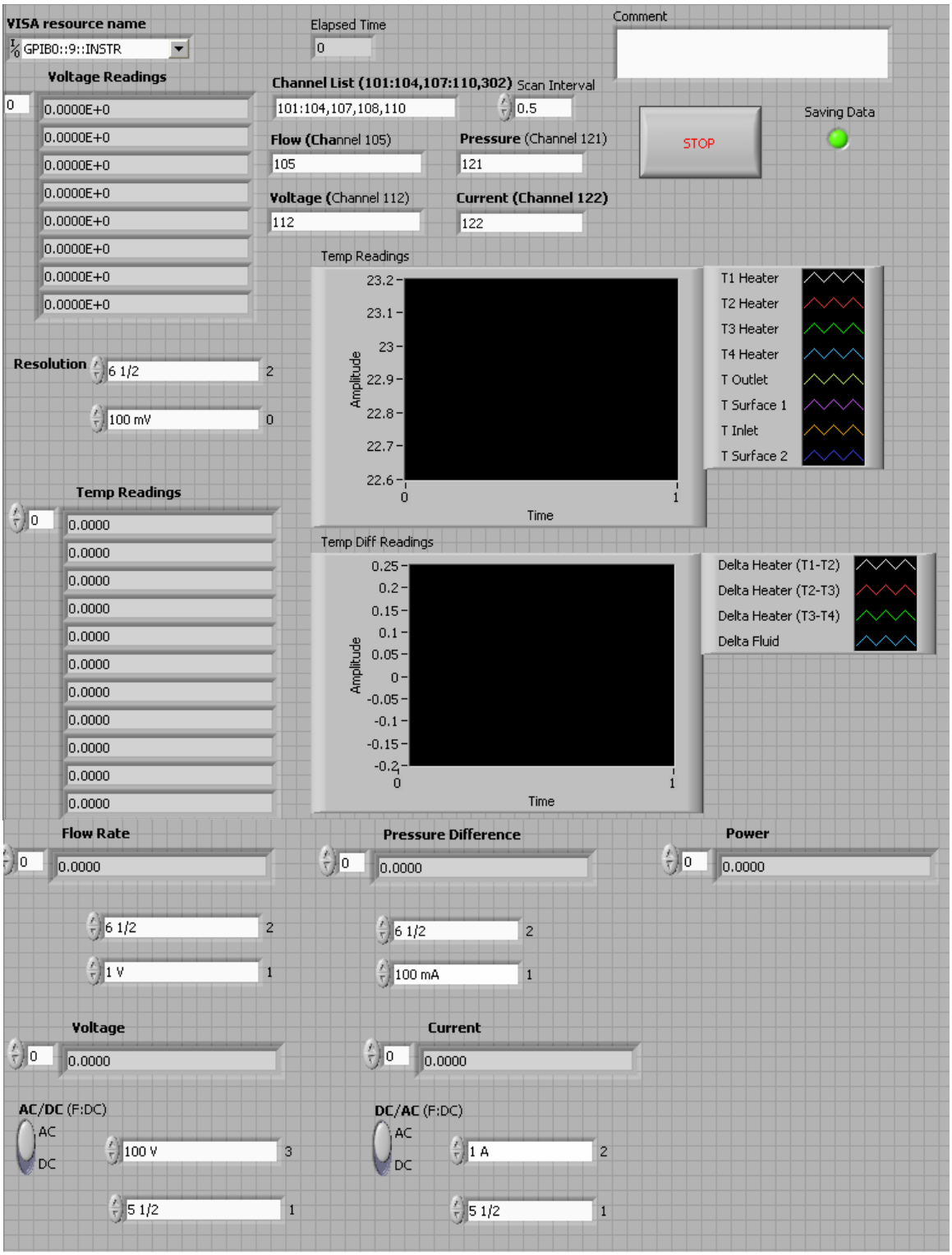

Figure 11: continued

CHAPTER 3

EXPERIMENTAL RESULTS

3.1 Carbon nanotubes

3.1.1 Carbon nanotubes before testing

Two major requirements the CNTs must possess for the current study are: one, they must be tall enough to create a measurable difference, with respect to the pressure drop, between the baseline devices and the devices with CNTs, and two, they need to adhere well to the surface so that they are not dislodged as a result of the shear stress inside the channel. If the CNTs do not create a measurable difference in the pressure drop, then a potential lack of heat transfer enhancement could be attributed to the CNTs not being tall enough, i.e. not having a large enough surface area for heat transfer. If a pressure drop increase is witnessed and a thermal enhancement is not, a stronger conclusion about the effects of CNTs in a microchannel can be drawn. Unfortunately, the details of the CNT growth process are not very well understood. Therefore, a trial-and-error methodology was performed over a wide assortment of growth parameters. The different growth parameters are listed and discussed in detail in Appendix C.

One of the major difficulties in growing the CNTs was the dramatic difference in their height when the recipe was used on a plain wafer versus when the recipe was used on a wafer that had etched microchannels. This occurrence is in contrast to the work reported in [34], where no difference was noticed between a plain wafer and an etched wafer. For this study, the plain wafer was a silicon wafer with 500 nm of SiO_2 deposited on the surface. 10 nm of iron was then deposited on top of the SiO_2 and the wafer was

diced into 1 cm squares. The diced samples were placed in the Easy Tube furnace, and the template recipe listed in section A.8 was used with a growth time of 20 minutes and a temperature of 720 °C. The heights were determined by a LEO 1530 scanning electron microscope (SEM) with the help of Mr. Brent Buchine. The resulting height of the array of CNTs was measured to be 120 μm, which is shown in figure 12. However, when identical growth parameters were used on a sample fabricated according to Appendix A with SiO_2 and Fe deposited on the bottom of the channels, the result was non-aligned growth with a height of approximately 2 μm. The non-aligned growth is shown in figure 13. The CNTs grown on a flat plate were always at least a factor of two taller compared to CNTs grown in microchannels. This was witnessed for multiple samples. Several factors can be attributed to the difference in growth profiles: surface roughness as a result of the etching, polymer contamination from the lift-off process, and increased flow resistance due to the etched channels. Determining the sensitivity of the growth to these factors is outside the scope of this research, but these factors are suggested for future investigations in microchannels with CNTs grown on the surface. Furthermore, the repeatability of growing CNTs with the same height was very low regardless of whether the growth was done on a flat plate or inside microchannels. For samples taken from the same wafer, the height of the CNTs would vary greatly for the same growth parameters. For example, three samples from the same wafer had heights of 40 μm, 80 μm, and 120 μm, when grown under the exact same conditions.

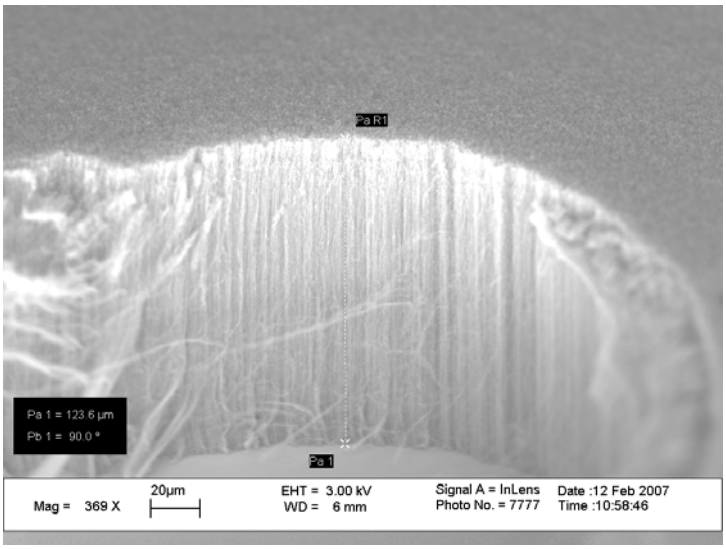

Figure 12: Height of CNTs grown on a flat silicon substrate
The CNTs are 124 µm tall. The silicon wafer is at the bottom of the figure.

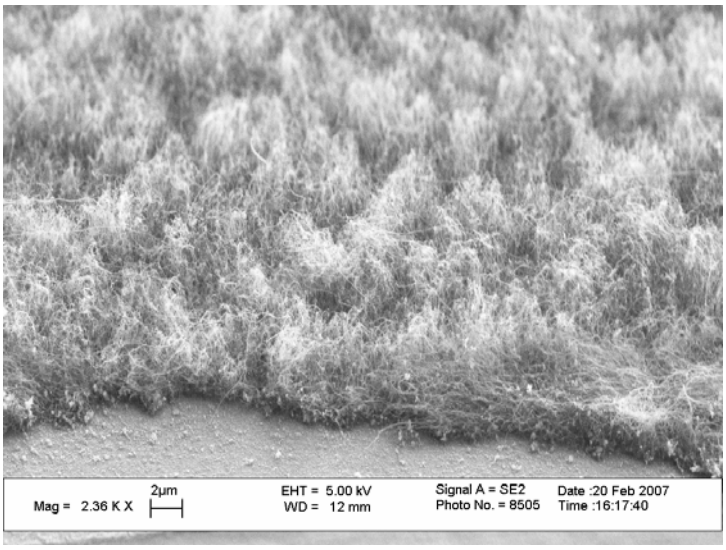

Figure 13: Height of CNTs grown inside microchannels
The CNTs are approximately 2 µm tall. Also, the CNTs are not vertically aligned as they were in figure 12. The silicon wafer can be seen at the bottom of the figure.

As stated previously, two different CNT deposition patterns were used. Figures 14 and 15 show both the partially covered pattern and the fully covered pattern, respectively. The samples with the fully covered pattern were grown on SiO_2, with iron

as the CNT catalysis, using a CVD method with a growth time of 30 minutes and a growth temperature of 820 °C.

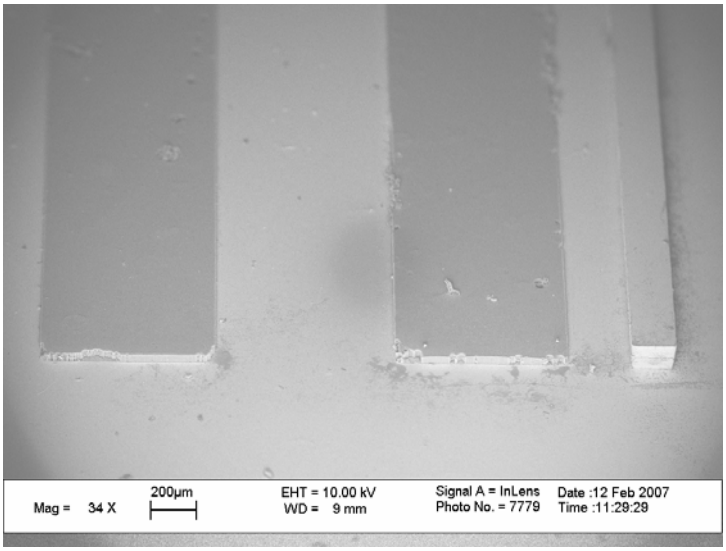

Figure 14: Partial coverage CNT pattern
The two rows of CNTs, each 1mm in width, can be seen. The silicon channel wall is on the right side of the figure.

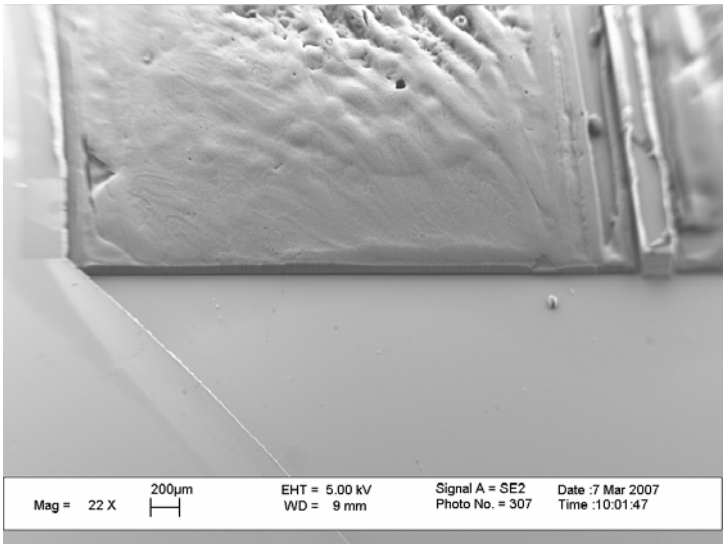

Figure 15: Full coverage CNT pattern
CNTs cover the bottom channel surface from wall to wall. The silicon channel wall is shown on the right of the figure.

Three samples were manufactured; their resulting heights were 40 µm, 80 µm, and 120 µm and, they can be seen in figure 16. The CNT height was determined to be fairly

uniform by measuring at several locations; however, clear topographical changes can be seen in figure 17. There was a consistent vacancy of CNTs adjacent to the channel walls. This is attributed to an error in the photolithography alignment. Only one sample with the partially covered pattern CNTs was produced. This sample was also grown on SiO_2, with iron as the CNT catalyst, using the CVD method but with a growth time of 20 minutes and a growth temperature of 720 °C. The resulting height, seen in figure 18, was 50 μm.

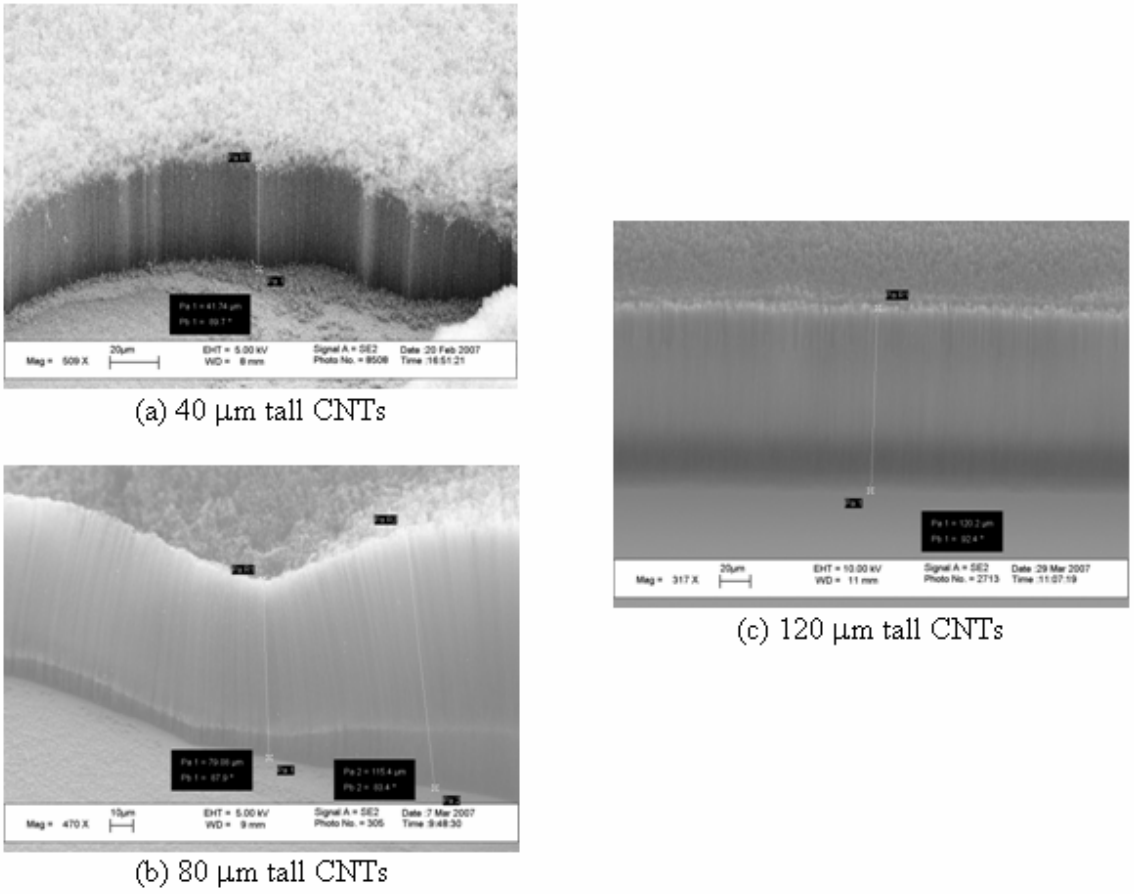

(a) 40 μm tall CNTs

(b) 80 μm tall CNTs

(c) 120 μm tall CNTs

Figure 16: Variability of CNT height

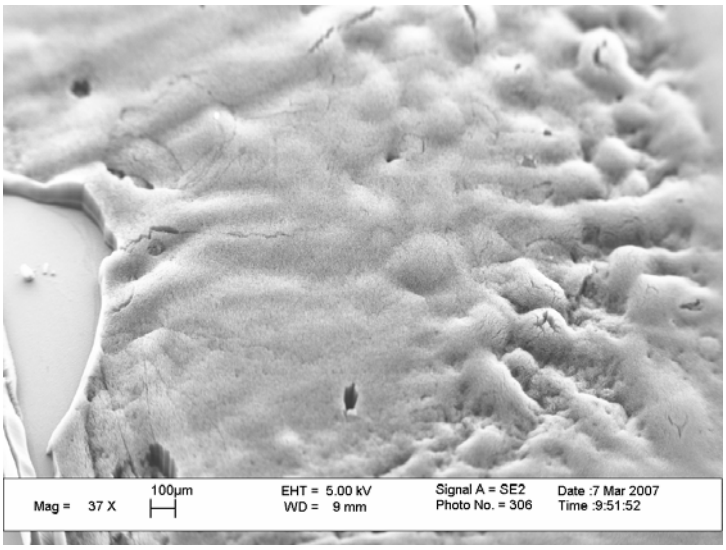

Figure 17: Topography of CNTs

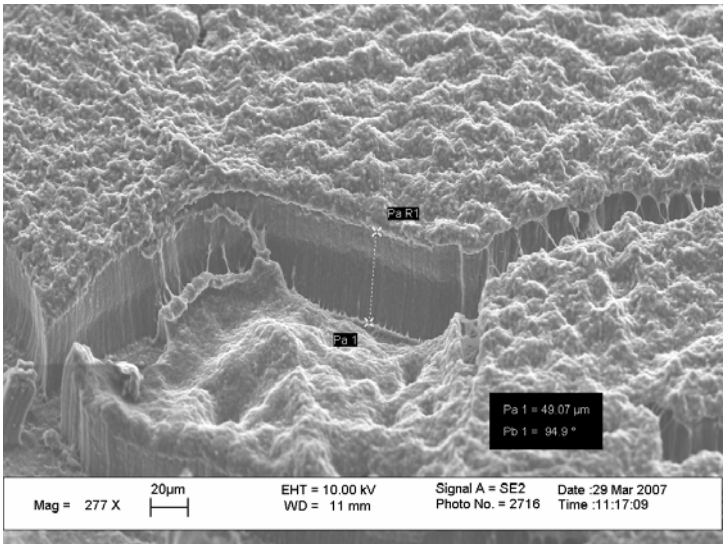

Figure 18: Height of CNTs with partial coverage

After the height of the CNTs was determined, a Raman spectroscopy measurement, along with a high magnification SEM image, was made to determine if the structures are indeed CNTs, and if they are single-walled or multi-walled. The Raman spectroscopy excites the CNT sample with a specific wavelength. The wavelength is shifted due to inelastic scattering of the sample, and the output is recorded. Graphite, as

well as CNTs, will display a peak due to its chemical arrangement at a wavenumber of approximately 1580 cm^{-1}. A graphitic defect peak, due to impurities in the chemical arrangement of carbon atoms, will also appear at an approximate wavenumber of 1350 cm^{-1}. If a large majority of the CNTs present are single-walled, then the peak ratio between the graphitic peak and the defective peak will be at least 12:1 [18]. Figure 19 has a peak ratio of approximately 1.3:1, and therefore, the majority of the tubes are not single-walled. Since graphite will also exhibit a similar peak ratio as the one shown in figure 19, a high magnification SEM image was taken to show that CNTs are indeed present. Figure 20, taken at 85 K magnification, shows the presence of CNTs. The bright dots are residual catalysis particles.

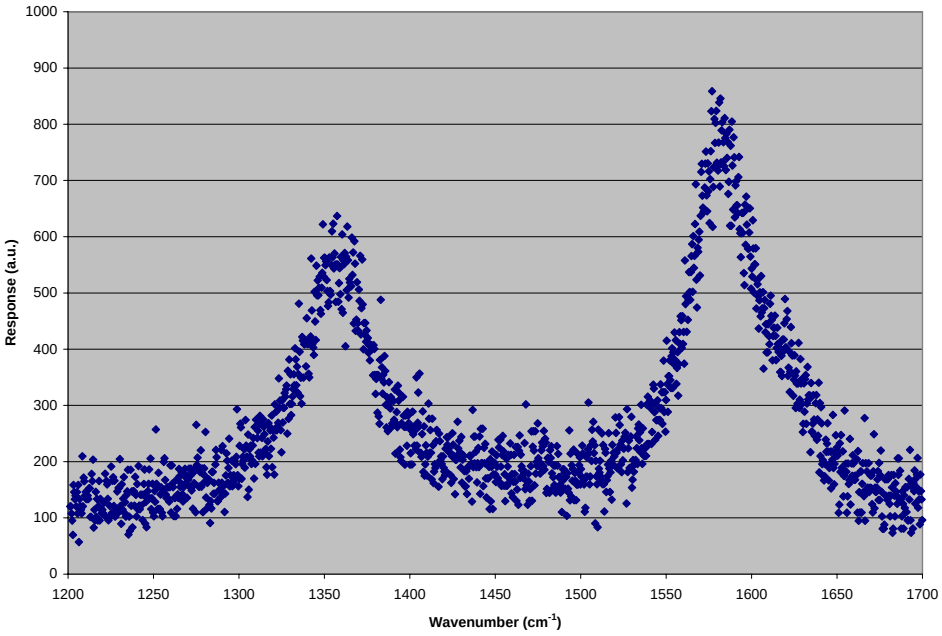

Figure 19: Raman spectroscopy measurement

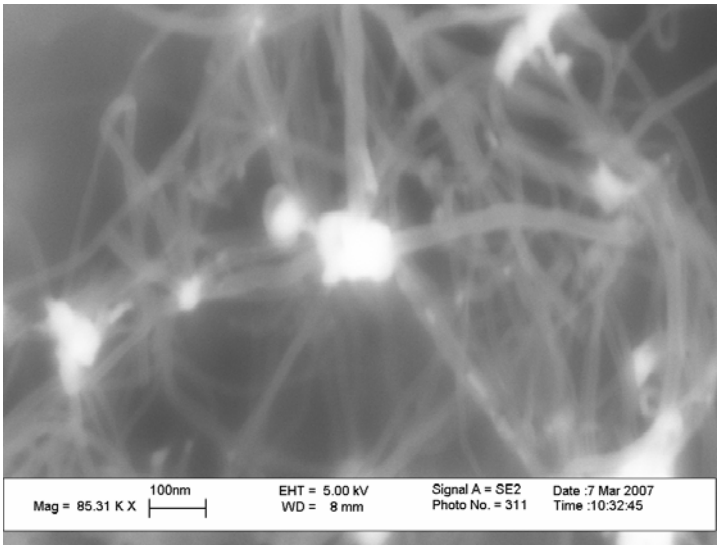

Figure 20: Individual CNTs

3.1.2 Experimental effects on carbon nanotubes

After the tests had been run, SEM images were again taken of the devices with CNTs. The images show that there was good adhesion between the CNTs and the surface. CNTs did not noticeably become dislodged from the surface as a result of the shear stress imposed by the fluid as seen in figure 21. However, the 120 μm tall CNTs were no longer vertically aligned. Although some tubes remained at their pre-testing height, many tubes have buckled. The CNTs tended to form clumps and permanently adhered to one another, which gave rise to the noticeable craters depicted in figure 21. This phenomenon was not as noticeable for the samples with shorter (~40-50 μm tall) CNTs as shown in figure 18. The CNTs appeared to have clumped together as seen from the structure of the free ends of the CNTs; however, only in a few areas have the CNTs buckled. Finally, since the CNTs are cantilevers, the free end of the CNT may bend in the direction of the flow. Unfortunately, the orientation of the CNTs could not be observed during testing.

The CNT buckling and clumping is attributed to capillary and van der Waals forces. At the conclusion of testing, the sample was allowed to dry before it was placed

in the SEM. Presumably, as the water evaporated, the capillary forces pulled the CNTs together. This phenomenon was also witnessed in [29]. However, the current investigation could not directly determine if water penetrated the CNT array. When methanol was flown to flush the system, air bubbles were released from CNT array, but no air bubbles were noticed when water was used to flush the system.

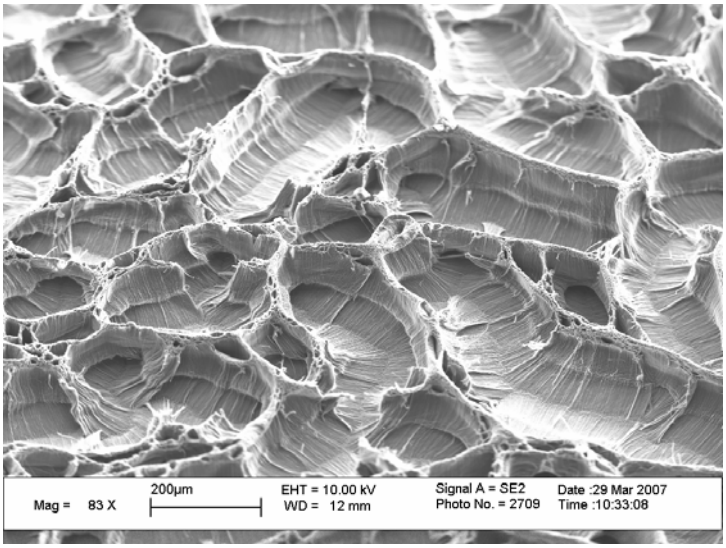

Figure 21: CNT clumping after wetting

Therefore, if water does not penetrate the CNT array, the clumping could be a result of the evaporation of methanol. Regardless of which fluid caused the CNTs to group together, the CNTs remained fixed due to the strong van der Waals forces that existed between tubes. On account of this, any hydraulic device involving CNTs must remain constantly wetted, or else the properties and the functionality of the device may be jeopardized.

3.2 Numerical modeling

Modeling was used to validate the accuracy of the baseline experimental results, in terms of the outlet water temperature, the silicon surface temperature and the pressure drop. The geometrical modeling and meshing was done in Gambit. The assistance of

Mr. Qihong Nie in the Gambit pre-processing is acknowledged. The mesh was then transferred to Fluent, a computational fluid dynamics software package, for numerical simulations. The model had a grid consisting of 8,866,587 computational cells and 1,675,444 nodes. A mixed mesh of tetrahedral and triangular cells was used with a mapped-scheme. The fluid was discretized with a standard scheme for the pressure and a first order upwind scheme for the momentum and energy equations. The pressure and velocity were coupled with the simple method.

The model consisted of the fabricated device, the fluid passing through the device, the polycarbonate test fixture and part of the copper heater. The model is depicted in figure 22. The flow boundary conditions were as follows: a variable inlet velocity input based on experimental test case of interest, a zero pressure at the outlet and no-slip and no-penetration boundary conditions at all liquid-solid interfaces. The thermal boundary conditions were an inlet fluid temperature of 296.1 K, a variable heat flux applied on the copper heater, adiabatic walls on the sides of the copper heater, an assumed typical natural convective heat transfer coefficient of 5 $Wm^{-2}K^{-1}$ around all outer surfaces of the model and an ambient temperature of 296 K. Zero contact resistance was assumed between the copper heater and the silicon. All material properties were assumed to be constants and were taken from [23]. The fluid properties were taken at the mean inlet and outlet temperatures that were measured during the corresponding experimental runs. The model was run four separate times, one for each of the testing conditions. The input parameters for the model are listed in table 3, and a set of representative results for the 30 W – 16 mL/min testing condition are shown in figures 23 through 25.

The pressure profile, figure 23, shows that, as expected, the maximum pressure occurs at the inlet to the channels. The fluid velocity profile at a cross-section taken 75 μm above the silicon surface, seen in figure 24, shows that the maximum velocities are at the inlet and outlet to the manifolds. Also, the flow is not uniformly distributed between the channels. 38% of the fluid flows through the center channel, while 31% of the fluid

flows through each of the two outer channels. The non-uniformity is further seen in a contour plot of the channel surface temperature in figure 25. The maximum surface temperature occurs at the exit of the top and bottom channels. The non-uniformity in the flow creates a lower temperature at the outlet of the middle channel compared to the outlet of the other two channels. The results in comparison to the baselines experimental results for all testing conditions are given in section 3.3.3. Since the TIM material was not modeled due to computational limits, and it significantly contributes to the thermal resistance, the heated region temperature was extrapolated from the model so that it could be compared to the experimental results. The thermal resistance of the TIM was multiplied by the heat rate through the TIM to determine the temperature drop across the TIM. This temperature drop was added to the local backside temperature of the silicon predicted by the model. The sum of these two temperatures is an estimate of the heated region temperature as predicted by the numerical simulation.

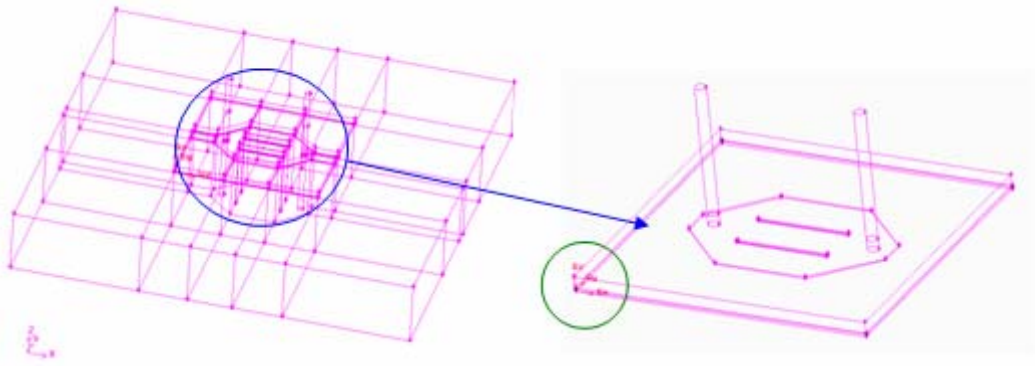

Figure 22: Numerical model diagram

The complete model is shown on the left. The silicon device, water flow path and cover plate are enhanced and shown on the right. The coordinate axes are circled in green on the figure on the right. The z-axis points in the axial direction of the inlet and outlet ports. The x-axis is along the bulk flow direction. The origin is taken at the corner and on the backside of the silicon device.

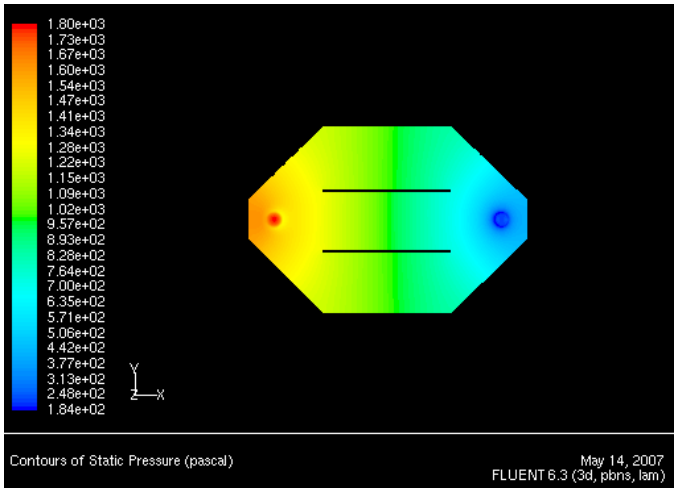

Figure 23: Numerical pressure contours

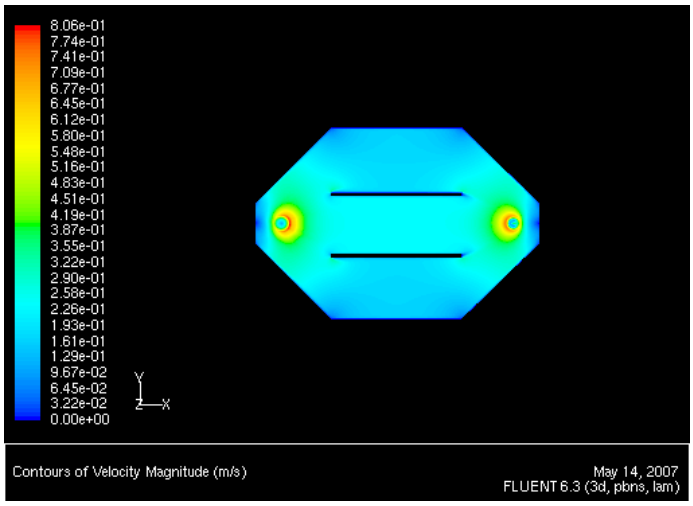

Figure 24: Numerical velocity contours

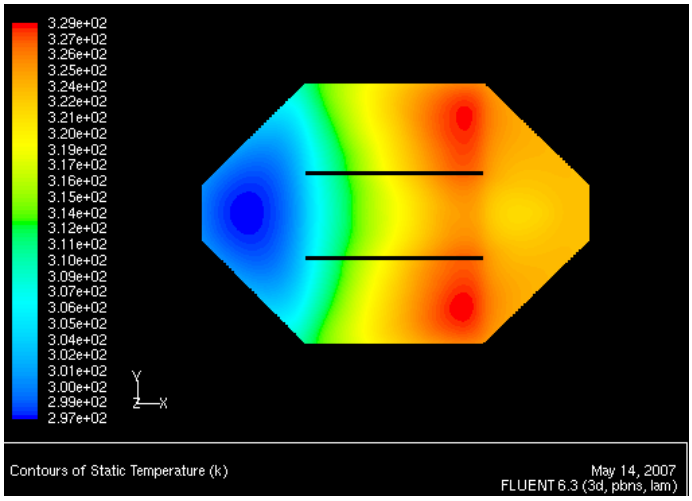

Figure 25: Numerical surface temperature contours

Table 3: Numerical model input parameters

Parameters	Numerical Run			
	1	2	3	4
$\overline{V}_{in}$ (m-s^{-1})	0.332	0.332	0.603	0.603
T_{in} (K)	296.3	296.1	296.1	296.1
μ^{w} (N-s-m^{-2})	0.000749	0.000857	0.000885	0.000813
ρ^{w} (kg-m^{-3})	993.2	996.5	997.2	995.3
k^{w} (W-m^{-1}-K^{-1})	0.625	0.613	0.611	0.618
$c_{p}{}^{w}$ (J-kg^{-1}-K^{-1})	4180	4179	4180	4179
$q^{"}$ (W-m^{-2})	272296	92030	92030	272296

3.3 Experimental data

The baseline devices and the devices with CNTs were evaluated by comparing the water temperature rise, the heated region temperature increase above ambient and the pressure drop. The device with the lowest heated region temperature increase and lowest pressure drop would be the most beneficial for electronics cooling applications.

3.3.1 Experimental uncertainty

Uncertainty in the experimental measurements for water temperature rise, heated region temperature rise and pressure drop were determined by the propagation of uncertainty method outlined in [37-42]. The largest uncertainties were due to the variation in thermal interface material (TIM) thickness, variations in the input volumetric flow rate and variations in the input heat flux. Geometric variations and equipment noise had a minimal effect on the uncertainty of the desired measurements. Furthermore, since all diagnostic equipment was calibrated, the bias error was minimized. Table 4 lists the

uncertainties with a 95% confidence level (P = 95) for each measurement and each testing condition. Details on the uncertainty calculations are given in Appendix B.

Table 4: Experimental uncertainties (P = 95)

Testing Condition	Water Temperature Rise (K)	Heated Region Temperature Rise (K)	Pressure Drop (kPa)
10 W 16 mL/min	0.6	2.0	0.4
30 W 16 mL/min	1.8	6.2	0.4
30 W 28 mL/min	0.8	5.8	1.1
30 W 10 mL/min	0.3	2.0	1.1

3.3.2 Resistor Network model

A resistor network model pertinent to this experimental setup was developed by expanding the resistor-network model created by Phillips for cold-plate heatsinks [43, 44]. The resistor network model relates the fluid inlet temperature to the heated region temperature based on the geometry and thermophysical properties of the setup. Figure 26 is a pictorial representation of the resistor-network.

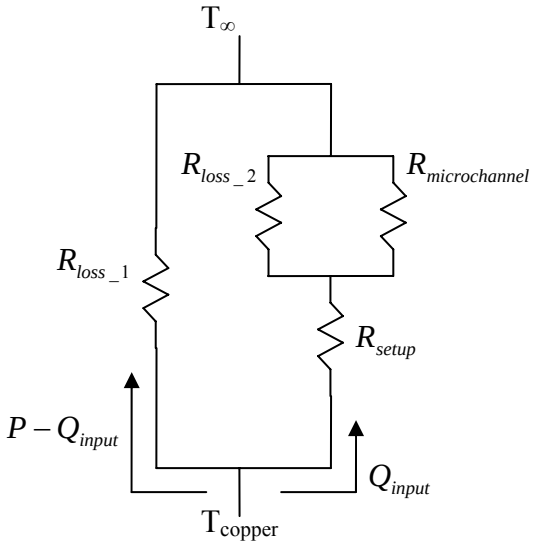

Figure 26: Thermal resistance model

$R_{microchannel}$ is the resistance Phillips developed and is determined by equation 9. The individual resistances were calculated using equations 10 through 12, where equation 11 is calculated with a Nusselt number of 5.39, which is the value for infinite parallel plates that are asymmetrically heated with a uniform heat flux [23].

$$R_{microchannel} = R_{cond} + R_{conv} + R_{bulk} \tag{9}$$

$$R_{cond} = \frac{t_{silicon}}{k_{silicon}} \tag{10}$$

$$R_{conv} = \frac{w + t_f}{h^* \cdot w + 2 \cdot h^* \cdot h \cdot \eta_f} \tag{11}$$

$$R_{bulk} = \frac{L \cdot \left(w + t_f\right)}{\dot{m} \cdot c_p{}^w \cdot \rho^w} \tag{12}$$

$R_{microchannel}$ includes contributions from conduction through the silicon, convection of the working fluid and the heating of the working fluid as the fluid passes along the length of the channel. R_{setup} is due to the conduction through the setup and is given by equation 13.

$$R_{setup} = \frac{t_{copper}}{k_{copper}} + \frac{t_{TIM}}{k_{TIM}} \tag{13}$$

R_{loss_1} accounts for the heat loss to the ambient through the heater insulation. R_{loss_2} accounts for the heat loss to the ambient by lateral diffusion through the silicon and then conduction to the plastic block. Both heat loss resistances are determined by fitting the analytical model to the experimental data. The heat loss resistances are constant, with the assumption of constant thermophysical properties, regardless of the input parameters. Therefore, a single experiment can be run to determine the two heat loss resistances, and the resulting values should predict the experimental data for all other testing conditions. The final expression for the rise of the heated region temperature is given by equation 14.

$$\Delta T_{copper} = q'' \left[0.04 \frac{W}{m^2 K} + \left(R_{setup} + \frac{R_{microchannel}}{0.046 \frac{W}{m^2 K} \cdot R_{microchannel} + 1} \right)^{-1} \right]^{-1} \quad (14)$$

The pressure drop is governed by equation 15, where f and D_h are calculated from equations 16 and 17 respectively.

$$\Delta P_{channel} = f \frac{\rho^w \cdot L \cdot \overline{U}^2}{2 \cdot D_h} \quad (15)$$

$$f = \frac{96}{\mathrm{Re}} \quad (16)$$

$$D_h = \frac{4 \cdot w \cdot h}{2(w + h)} \quad (17)$$

The friction factor is estimated from the derivation for laminar flow between infinite parallel plates [23]. The Reynolds number is given by equation 18.

$$\mathrm{Re} = \frac{\rho^w \cdot \overline{U} \cdot D_h}{\mu^w} \quad (18)$$

The pressure drop from equation 15 is only for the channels. However, the experimentally measured pressure drop consists of the pressure drop across the inlet and outlet manifolds and other piping in addition to the channels. In order to compare the analytical pressure drop to the experimental, the pressure drop across the manifolds was taken from the numerical model because the loss coefficient for this particular channel inlet and outlet design is unknown. Furthermore, the pressure drop of the additional piping was experimentally measured with a pressure transmitter by allowing the flow to bypass the channel. The pressure drop for the bypass at a flow rate of 16 mL/min and 28 mL/min was 0.9 kPa and 1.6 kPa, respectively. The pressure values from the manifolds and additional piping were added to the solution to equation 15 so that the experimental values could be compared.

3.3.3 Baseline repeatability

Three different baseline samples were tested a total of sixteen times to check the repeatability of the experimental setup. Figure 27 graphically represents the measured water temperature rise, as well as, compares this to the numerical simulations and resistor network predictions. The different testing conditions are organized by color, and the different results are organized by shape. The resistor network model is represented as a 'square' data point. The uncertainty of the resistor network model was discussed in section 3.3.1. Since the propagation of uncertainty method requires a known functional relationship between the measured quantity and the system inputs, the uncertainty was calculated using equation 14 as the known function.

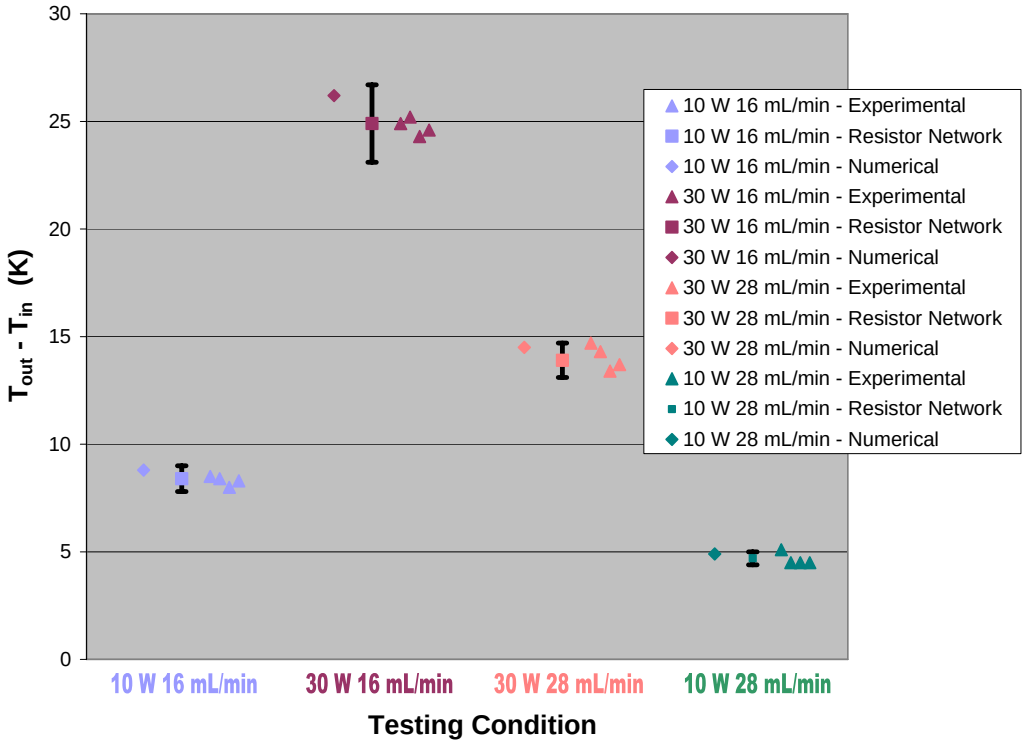

Figure 27: Baseline agreement – water temperature rise

The numerical model result is the 'diamond' to the left of the resistor network model. The numerical model over-predicts the water temperature rise compared to the

resistor network model for every testing condition; however, the numerical model is within the uncertainty of the resistor network model. The over-prediction of the water temperature rise is attributed to the assumption of thermally fully-developed flow. The resistor network model assumed that the flow is thermally fully-developed; however, the numerical model does not. The thermally developing region has a higher convective heat transfer, and therefore, more heat would be transferred to the fluid.

The experimental data are displayed to the right of the analytical result and are represented with 'triangle' data points. The experimental data vary within the experimental uncertainty predicted by the propagation of uncertainty method.

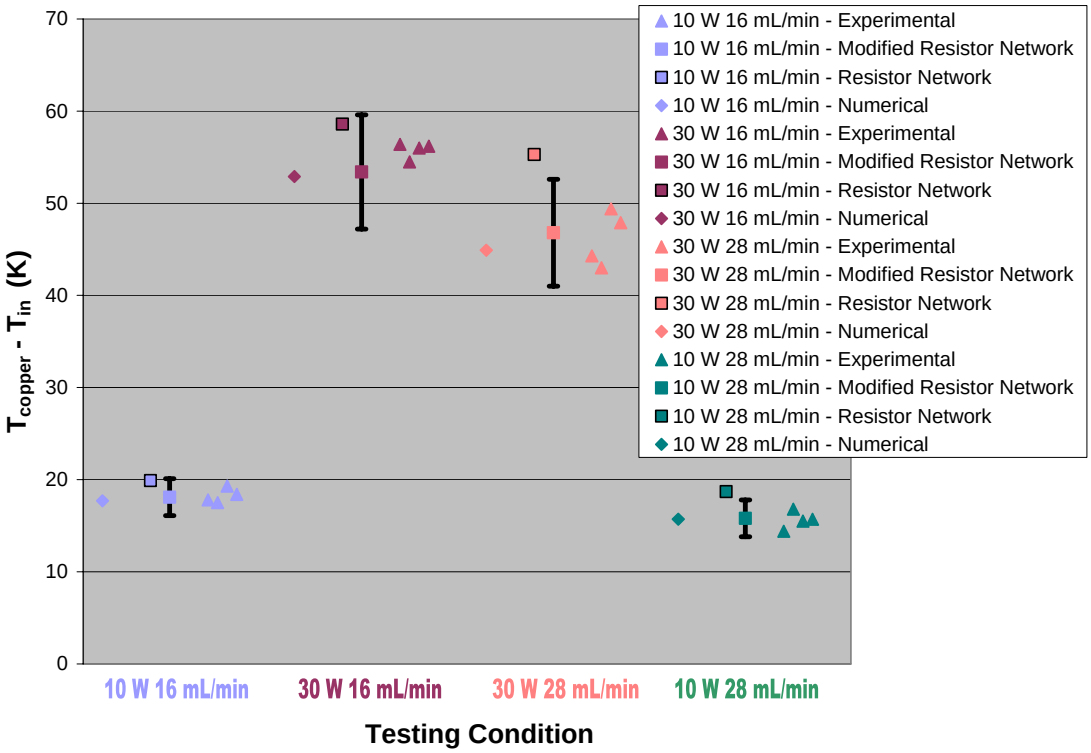

Figure 28: Baseline agreement – heated region temperature rise

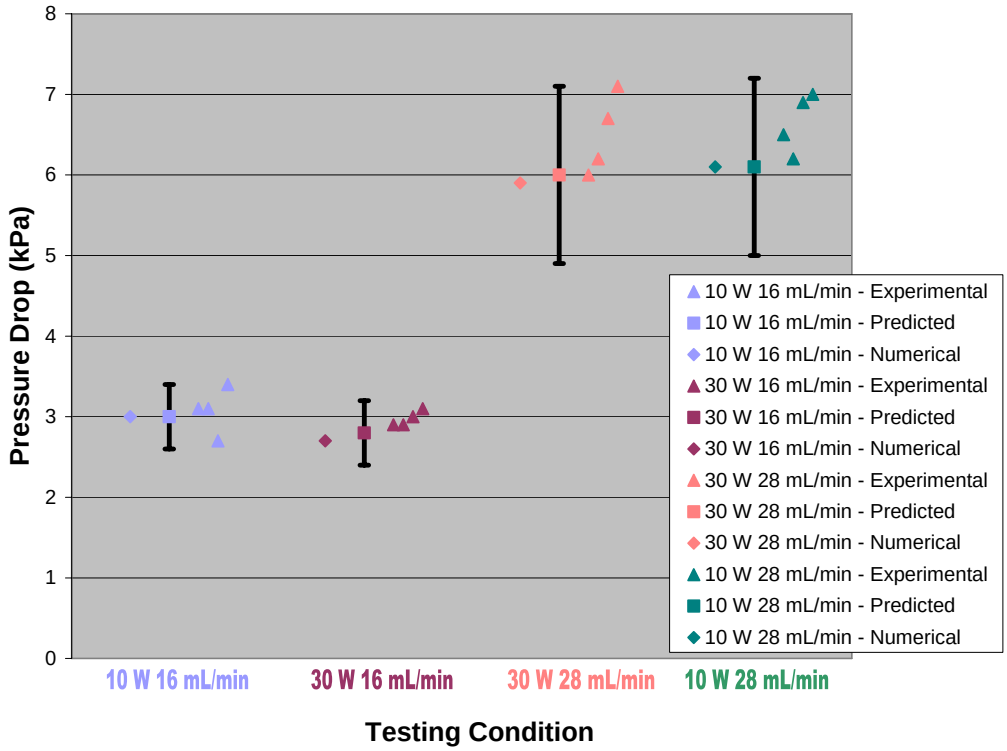

Figure 29: Baseline agreement – total pressure drop

Overall, there is good agreement between the numerical model, resistor network model and the experimental results for all testing conditions. Furthermore, the experimental results fall within the predicted uncertainties. Therefore, any data point from the devices with CNTs that falls significantly outside of these uncertainty bands can be attributed to the presence of CNTs inside the microchannel. Figures 28 and 29 display the heated region temperature rise and the system pressure drop, respectively. The plots are organized in a similar fashion as the water temperature rise; however, a second resistor network model data point is represented in figure 28. The resistor network model outlined in section 3.3.2 only accounts for heat transfer to the working fluid from the channels. The corresponding value is represented by the square data point outlined in black. In reality, heat is transferred to the working fluid from both manifolds. The numerical model predicts that for the 16 mL/min flow rate testing conditions, 10% of the total heat transferred to the water is transferred from the inlet manifold. A negligible

amount of heat is transferred to the working fluid from the outlet manifold. The 28 mL/min flow rate tests, on the other hand, had significant heat contributions to the working fluid from both the inlet and outlet manifold.

The rate of heat transfer to water predicted for all testing conditions based on the section of the silicon device is outlined in table 5. Since for the 16 mL/min flow rate testing conditions only the inlet manifold contributed to heat transfer, the surface area of the inlet manifold was added to the total effective surface area for convective heat transfer. For the 28 mL/min flow rate testing condition, the total effective surface area included the channels, as well as both the inlet and outlet manifolds. The square data points in figure 28 represent the resulting values, when the inlet manifold surface area is taken into account for the 16 mL/min flow rate experiments and when the inlet and outlet manifold surface area is taken into account for the 28 mL/min flow rate experiments. Good agreement between the numerical model, the modified resistor network model and experimental results is observed. Also, the experimental data fall within the predicted uncertainty. Table 6 lists the ratio of energy gained by the fluid to the energy input to the electric heater, along with the associated uncertainties for the resistor network predictions. All experiments had an energy ratio of at least 88%. Lastly, table 7 compares the ratio of energy gained by the fluid to the energy input into the silicon device, i.e. after factoring out the heat lost through the heater insulation, between numerical model and the resistor network model.

Table 5: Numerical model predictions of heat transferred to working fluid

	Heat transferred based on section (W)			
Testing Condition	Channels	Channel walls	Inlet manifold	Outlet manifold
10 W 16 mL/min	7.7	0.3	1.1	0.3
30 W 16 mL/min	22.7	0.9	3.2	0.9
30 W 28 mL/min	23.3	1.0	2.5	1.2
10 W 28 mL/min	7.9	0.3	0.8	0.4

Table 6: Experimental energy ratio

Testing Condition	Calorimetric Energy (W)	Power Input (W)	Ratio (%)	Uncertainty (%)
10 W 16 mL/min	9.2	10.1	90.0	6.0
30 W 16 mL/min	27.2	30.2	90.0	5.0
30 W 28 mL/min	27.5	30.2	91.0	5.0
10 W 28 mL/min	9.3	10.1	92.0	5.0

Table 7: Energy ratio comparison between numerical and resistor network models

Testing Condition	Numerical Model	Analytical Model
10 W 16 mL/min	97.0 %	96.0 %
30 W 16 mL/min	97.0 %	96.0 %
30 W 28 mL/min	98.0 %	97.0 %
10 W 28 mL/min	97.0 %	97.0 %

3.3.4 Comparison among devices

Three different CNT samples were tested. The first consisted of 50 μm tall CNTs that only partially covered the bottom surface of the channel. The second consisted of 40 μm tall CNTs, while the CNT height for the third sample was 120 μm. For both the

second and third samples, the CNTs fully covered the bottom surface of the channel. The samples were run for each testing condition, and figures 30 through 49 display the results. The graphs are grouped by testing condition. Figures 30 through 34 are dedicated to the 10 W, 16 mL/min testing condition, figures 35 to 39 are for 30 W, 16 mL/min testing condition, figures 40 to 44 are for 30 W, 28 mL/min testing condition, and finally, figures 45 to 49 are for 10 W, 28 mL/min testing condition.

The first graph for each testing condition compares the water bulk temperature rise using the raw data from the three CNTs samples, as well as a representative baseline sample. The second graph in each set compares the averaged steady-state water temperature rise values for the CNT samples and the predicted value from the resistor network analysis, with corresponding uncertainty bars. For every testing condition and for every sample, the transient behavior and water bulk temperature rise values are within experimental uncertainties. This result is in contrast to the experimental data provided in [29], which showed that devices with CNTs have a higher thermal transient response than baseline devices. The conflicting result is accredited to the experimental uncertainties, formation of black silicon and differences in the experimental configuration. Also, the devices have a similar water temperature rise because there is a constant heat flux applied to the device. Since the heat loss is minimal, the majority of the heat will be transferred to the working fluid regardless of the thermal resistance between the heated region temperature and the working fluid. In similar fashion to the first graph, the third graph for each testing condition compares the heated region temperature rise using the raw data from the three CNTs samples and a representative baseline sample. The fourth graph displays the steady-state heated region temperature values of the CNT devices and those predicted from the resistor network model. Except for the 10 W, 16 mL/min testing condition, the device with the 120 μm CNTs had a measurably higher heated region temperature. Although the other two CNT samples show a trend of higher heated region

temperatures, they are within the experimental uncertainty for the baseline testing conditions.

The fifth, and final, graph in the set depicts the steady-state pressure drop. Once again, the three CNT samples are compared to the predicted pressure drop value for each testing condition. The 50 μm, partially covered CNT sample had a similar pressure drop as the baseline for all testing conditions. The 40 μm, fully covered CNT sample had a larger pressure drop compared to the baseline, roughly by a factor of two. The 120 μm, fully covered CNT sample had the largest pressure drop, which was an order of magnitude larger than the baseline. Finally, the pressure drop for the 28 mL/min testing conditions was too large to run experiments for the 120 μm, fully-covered CNT sample. The inlet port to the channels fractured at 12 psi. As a result, pressure drop data were not obtained, and the thermal performance data for the 28 mL/min testing were taken from a sample that had 80 μm tall CNTs with full coverage of the bottom channel surface area.

The pressure drop results are expected. As the percentage of volume occupied by the CNTs increases, the pressure drop also increases. The 50 μm, partially-covered CNTs only occupy 16.5% of the total channel volume. As a result, the presence of these CNTs is not significant, leading to a pressure drop comparable to the baseline. The 40 μm, fully-covered CNTs occupy 26.7% of the total channel volume. This decrease in hydraulic diameter has a noticeable effect on the pressure drop. Finally, the 120 μm, fully-covered CNTs occupy 80% of the total channel volume. The pressure, which is strongly dependent on the hydraulic diameter for pressure driven flows, caused the channels to fracture.

The CNTs do not increase the convective heat transfer. They either exhibit no benefit or they decrease the thermal performance depending on their height. The results show that the higher the percentage of channel volume occupied by the CNTs, the higher the heated region temperature. Therefore, the CNTs are adding thermal resistance to the

system due to either contact resistance between the CNTs and the silicon, and/or the hydrophobic nature of CNTs. Intuitively, if the fluid does not wet the CNTs, the thermal resistance would increase. If the additional thermal resistance is solely due to contact resistance, then the increase in heated region temperature should be linearly proportional to heat input to the system, i.e. the contact resistance should be independent of CNT height. However, this is not the case. For the 40 μm, fully covered CNT sample, the CNTs added between 0.2 K/W and 0.4 K/W resistance to the system. The 120 μm, fully-covered CNT sample, on the other hand, added between 0.75 K/W and 1.4 K/W to the system. [45] found that the contact resistance between an array of CNTs and the growth surface is negligible; however, the catalysis material is not mentioned. Depending on the catalysis used, this may also explain why the resistance added by the CNTs is not independent of the CNT height. Also, [46] concluded that a large temperature drop occurs at the CNT-liquid interface because the energy contained in the high-frequency phonon modes needs to be shifted to low-frequency modes before it can be conducted to the fluid. Therefore, the higher heated region temperature could potential be due to the poor coupling of phonon modes between the water and the CNTs, in addition to the hydrophobic nature of CNTs.

Finally, comparable performance was witnessed between the 50 μm, partially-covered CNTs and the 40 μm, fully-covered CNTs. This result requires explanation. For the data to be consistent, the fully-covered CNT device is expected to have a worse thermal performance compared to the partially-covered CNT device because the occupied volume is greater for the fully-covered CNT device. The data collected only reflect the temperature changes in the system. The heat transfer coefficient is inferred from these temperature measurements. The fully-covered CNT sample, in actuality, has a smaller hydraulic diameter compared to the partially-covered CNT sample. Therefore, the estimated convective heat transfer coefficient is larger for this sample compared to the partially-covered sample. This would automatically lead to a decrease in surface

temperature, regardless of the thermal performance of the CNTs. As a result, the fully-covered CNT sample appears to have a better thermal performance, compared to the partially-covered CNT sample, when in actuality, this observed increase in thermal performance is due to the decrease in hydraulic diameter and not a surface area increase or thermal conductivity effect of the CNTs.

Based on the heated region temperature and the pressure drop, the baseline sample had the best performance. The addition of CNTs not only increased the pressure drop, as expected, but also increased the heated region temperature. When the CNTs occupy less than 20% of the channel volume, their effect on the pressure drop and heat transfer is negligible. As the CNT occupation volume increases, the effects of CNTs on the pressure drop and heated region temperature noticeably increase. It is anticipated that this is caused by the fluid largely bypassing the CNTS because the flow impedance is far greater through the CNTs than over them. Even if water penetrated into the CNT array, it is unlikely to wet them due to their hydrophobic nature [33]. This would lead to a decrease in expected heat transfer performance. Furthermore, the flow rate of the water would be reduced because the pressure drop through the CNTs has to match the pressure drop for the gap above the CNTs. A low water flow rate would lead to reduced heat removal. Therefore, unless the fluid wets the CNTs and a high flow rate can be achieved throughout the CNT array, CNTs will not improve the thermal performance of a silicon microchannel.

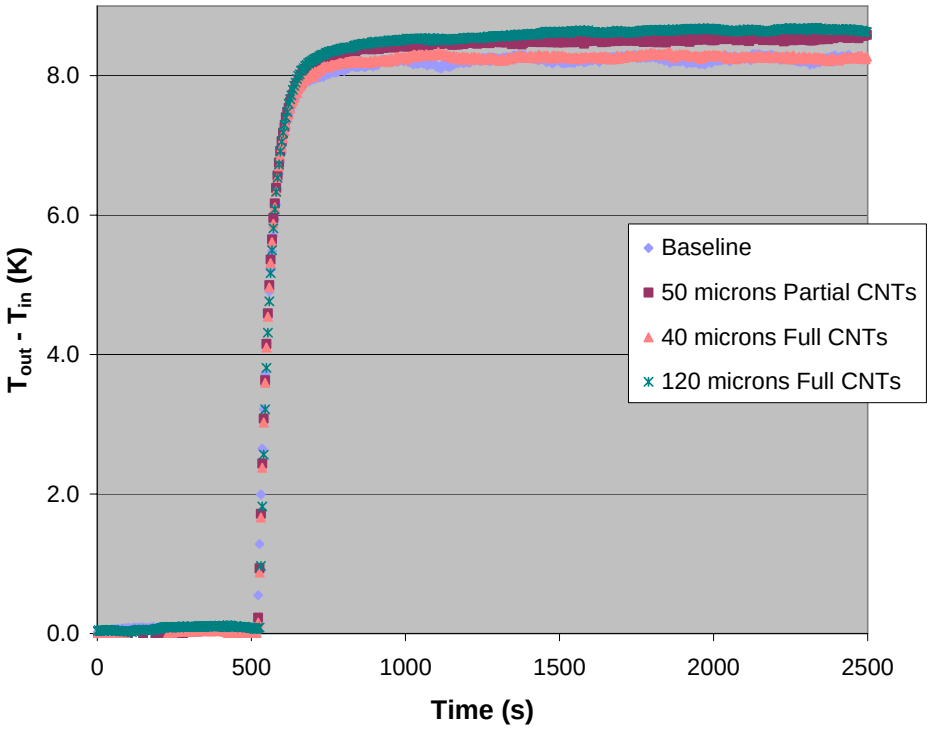

Figure 30: 10 W – 16 mL/min: transient water temperature rise

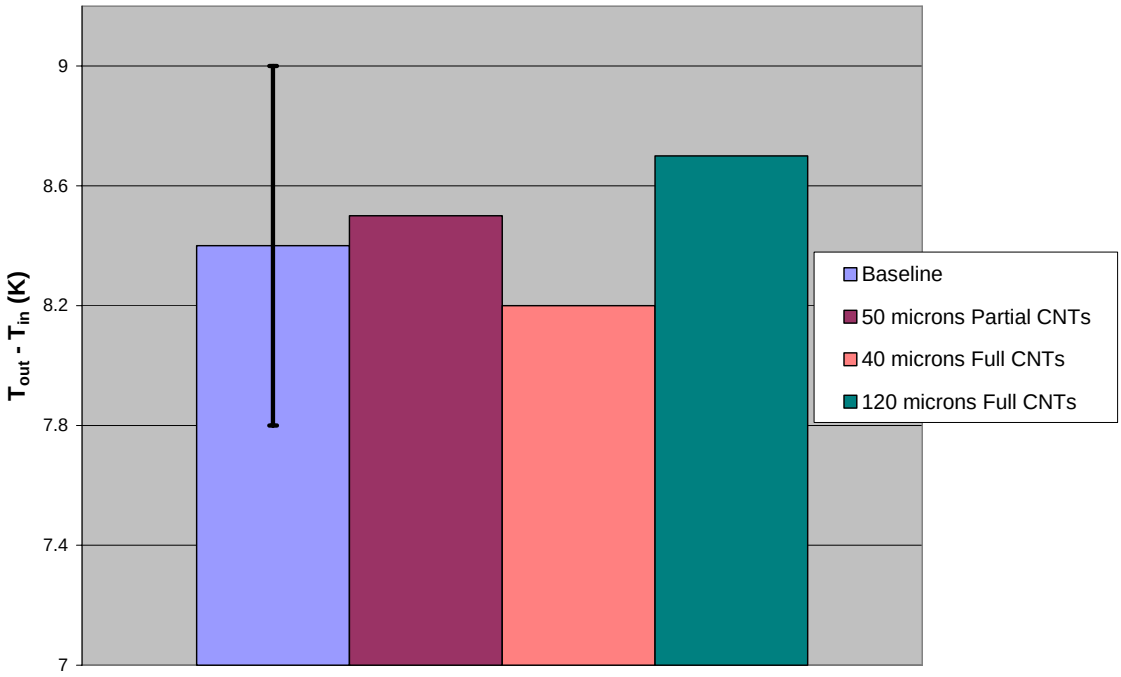

Figure 31: 10 W – 16 mL/min: steady-state water temperature rise with associated uncertainty band

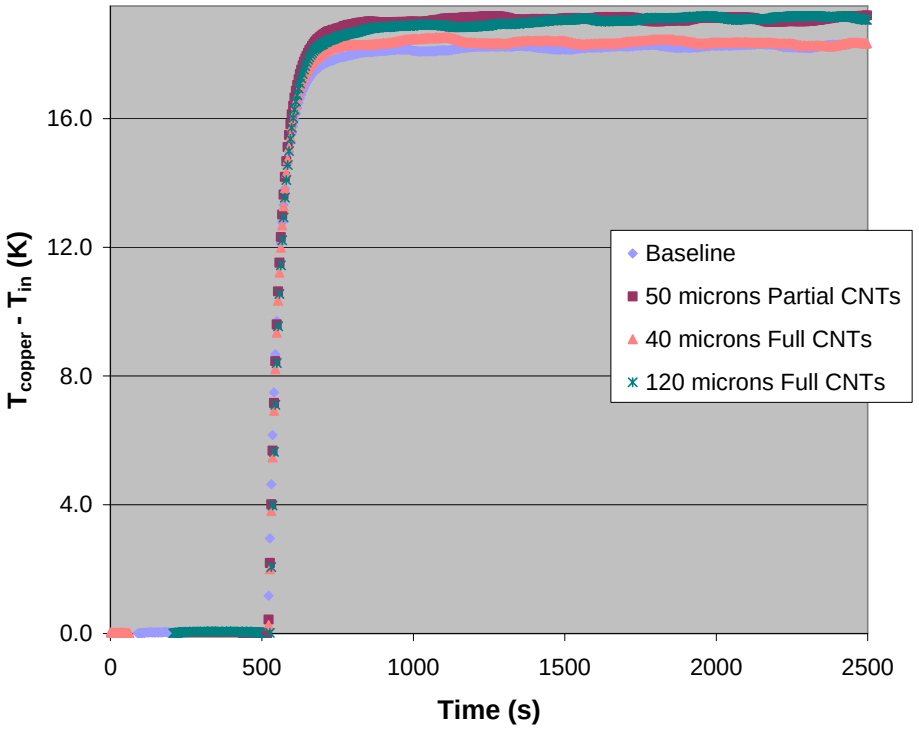

Figure 32: 10 W – 16 mL/min: transient heated region temperature rise

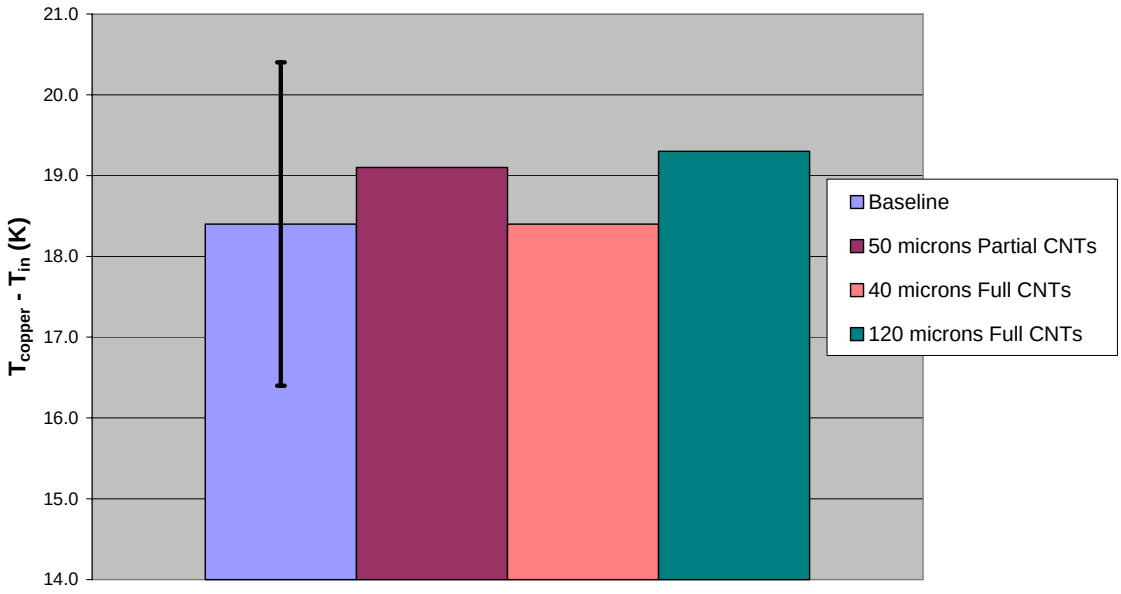

Figure 33: 10 W – 16 mL/min: steady-state heated region temperature rise with associated uncertainty band

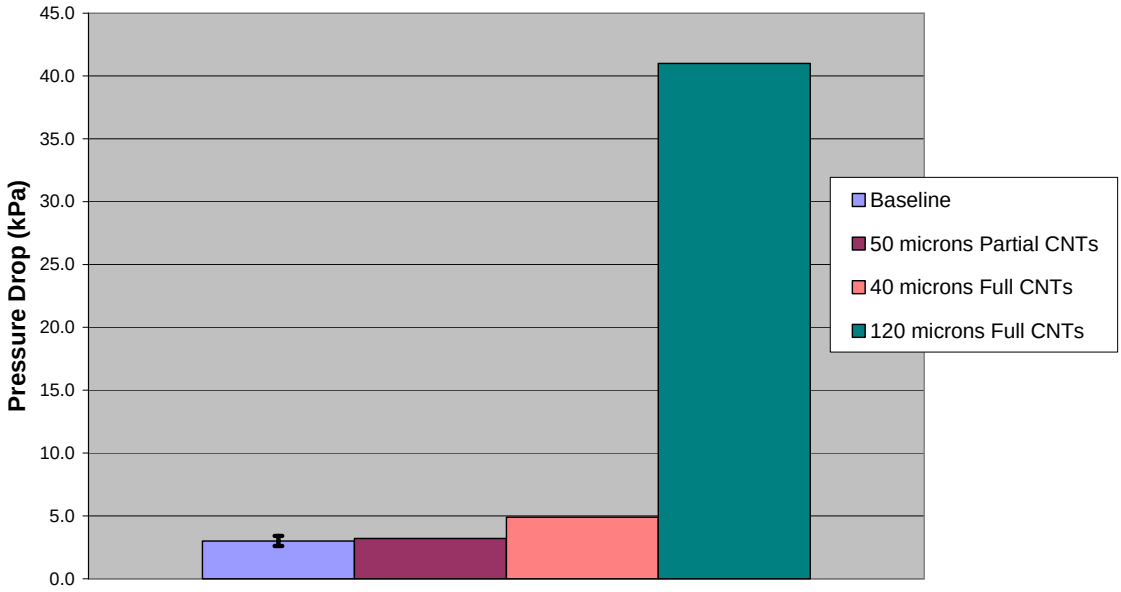

Figure 34: 10 W – 16 mL/min: steady-state total pressure drop with associated uncertainty band

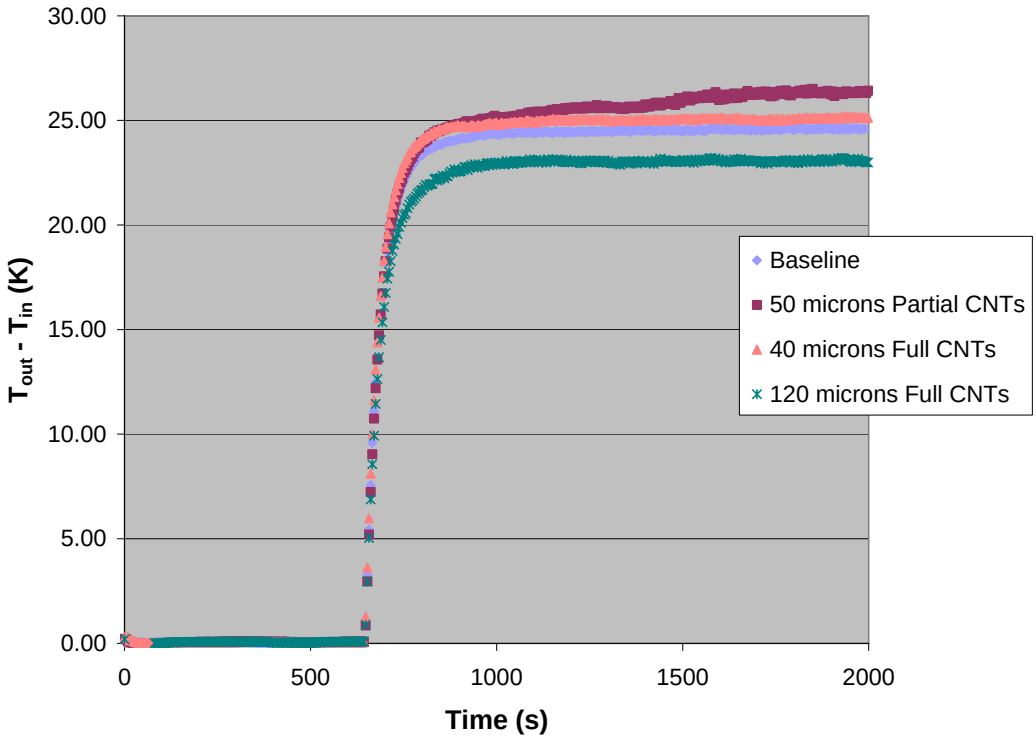

Figure 35: 30 W – 16 mL/min: transient water temperature rise

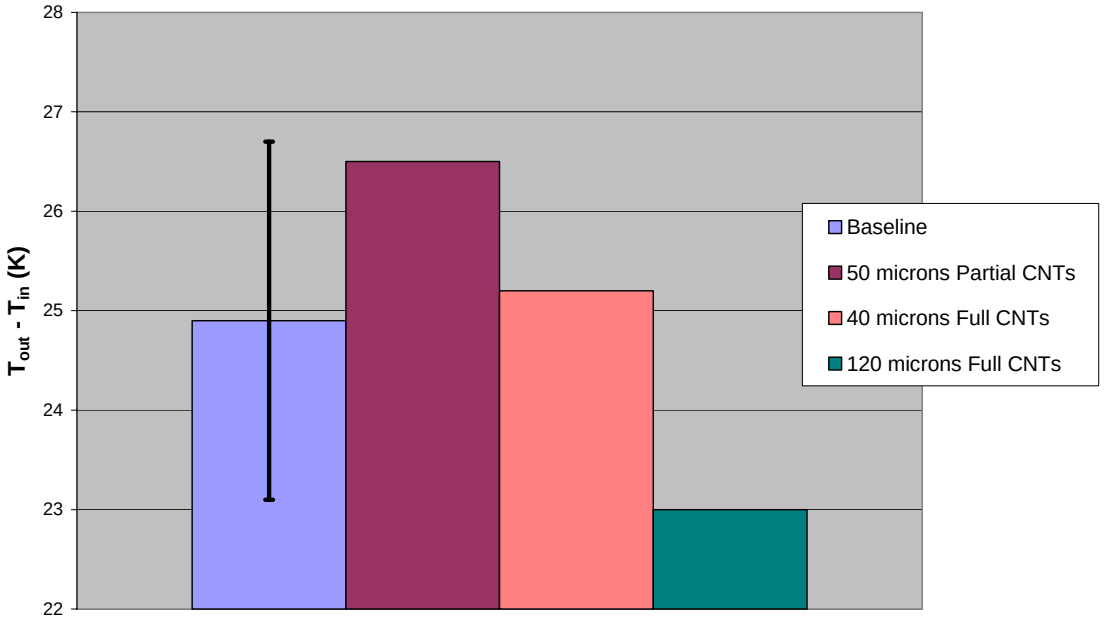

Figure 36: 30 W – 16 mL/min: steady-state water temperature rise with associated uncertainty band

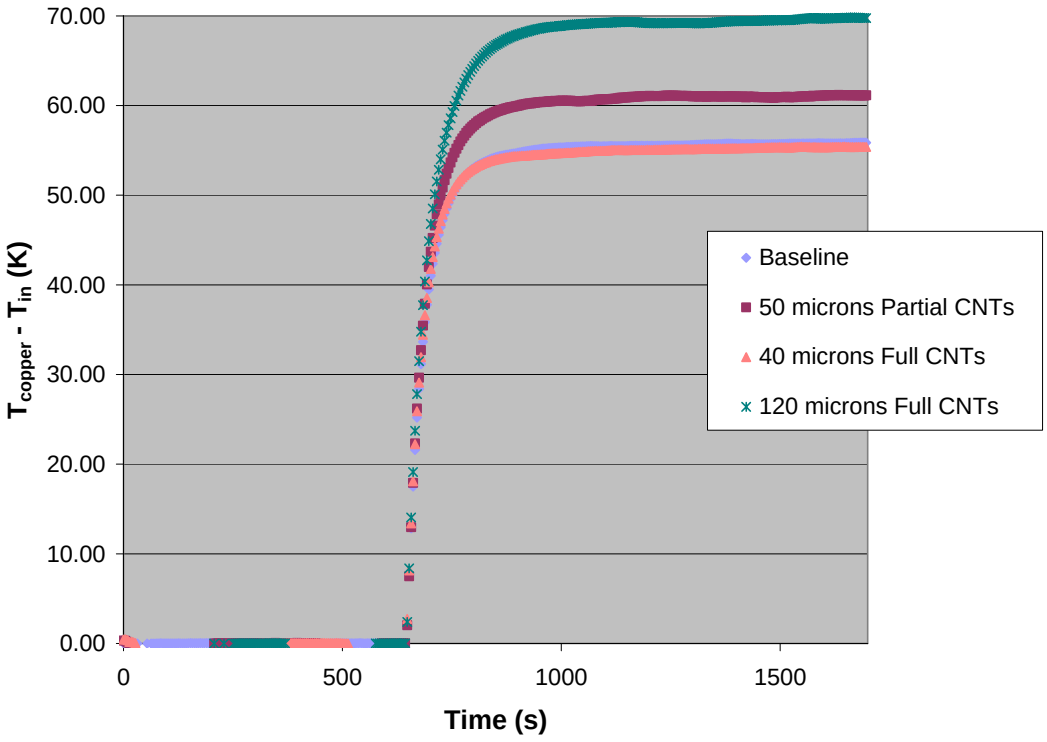

Figure 37: 30 W – 16 mL/min: transient heated region temperature rise

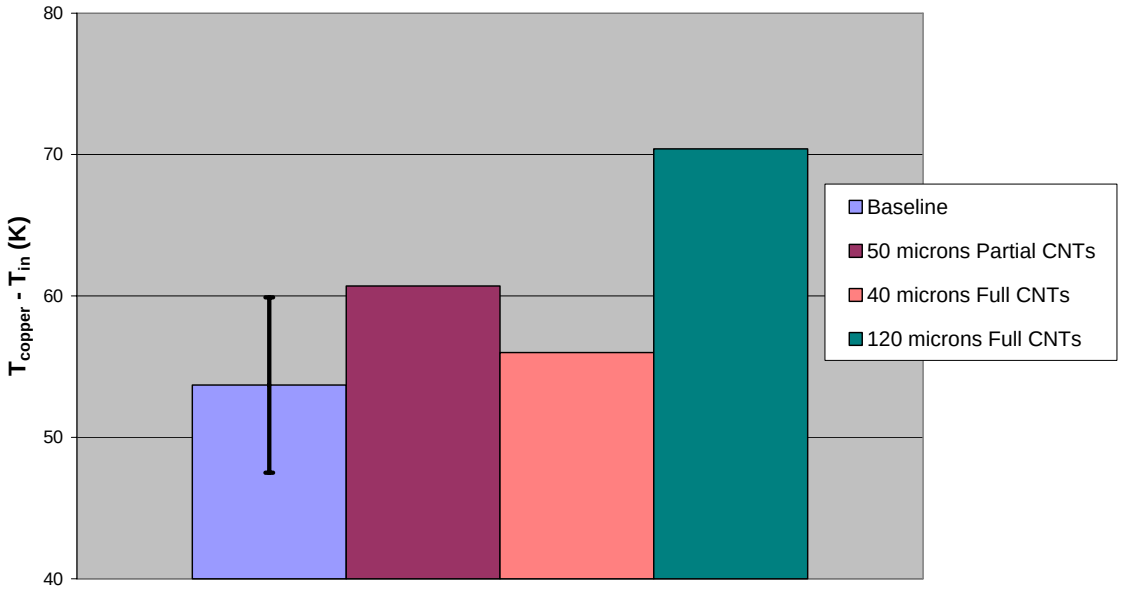

Figure 38: 30 W – 16 mL/min: steady-state heated region temperature rise with associated uncertainty band

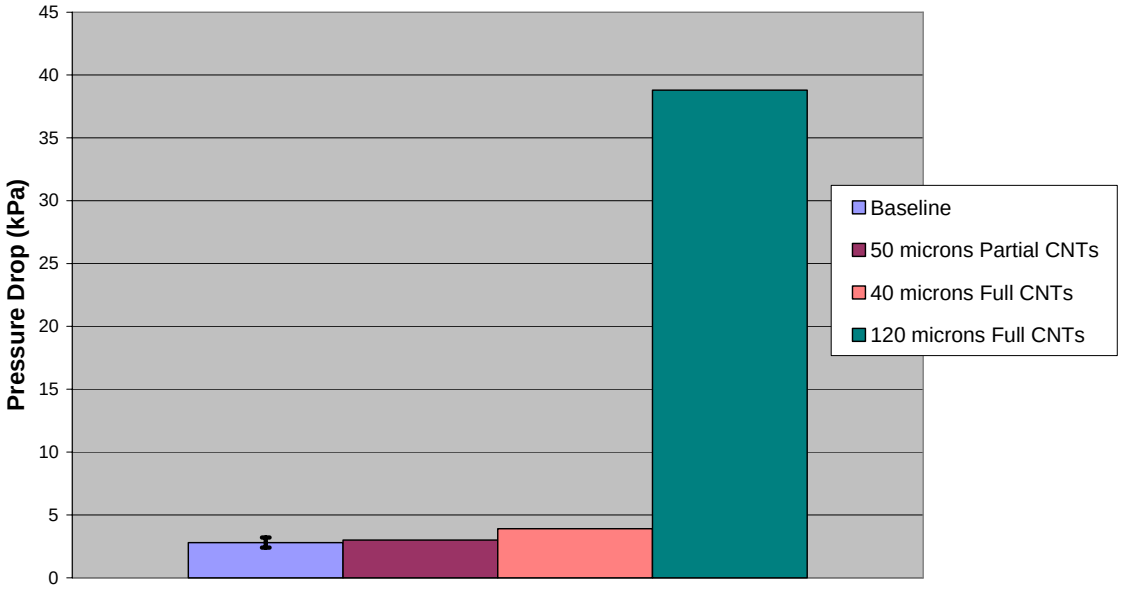

Figure 39: 30 W – 16 mL/min: steady-state total pressure drop with associated uncertainty band

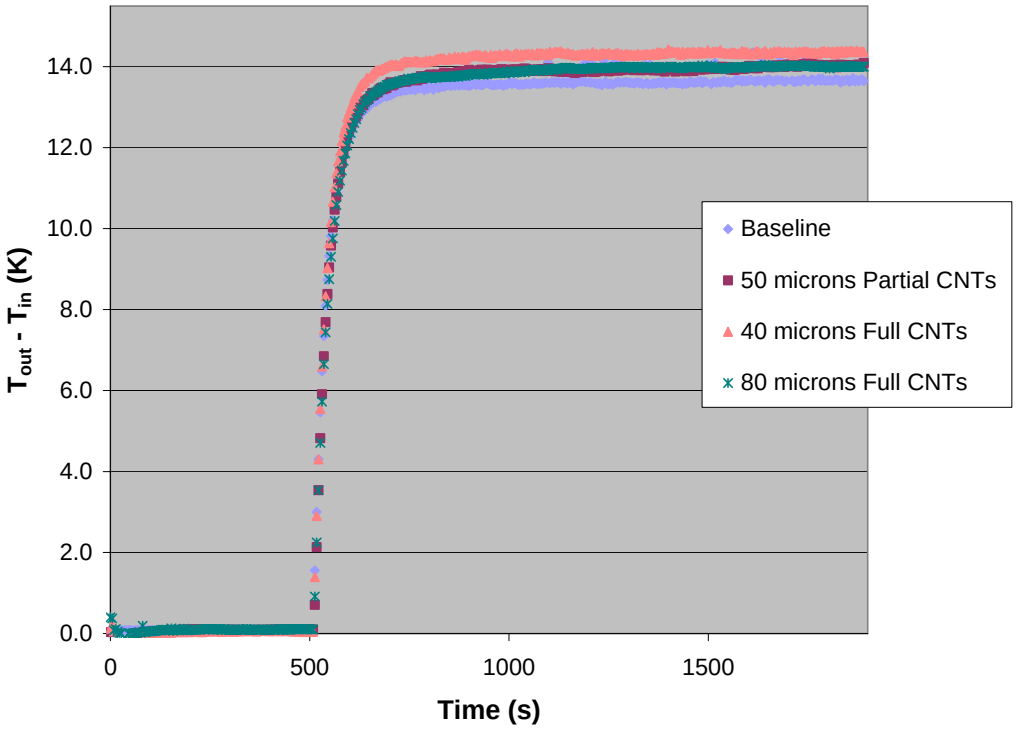

Figure 40: 30 W – 28 mL/min: transient water temperature rise

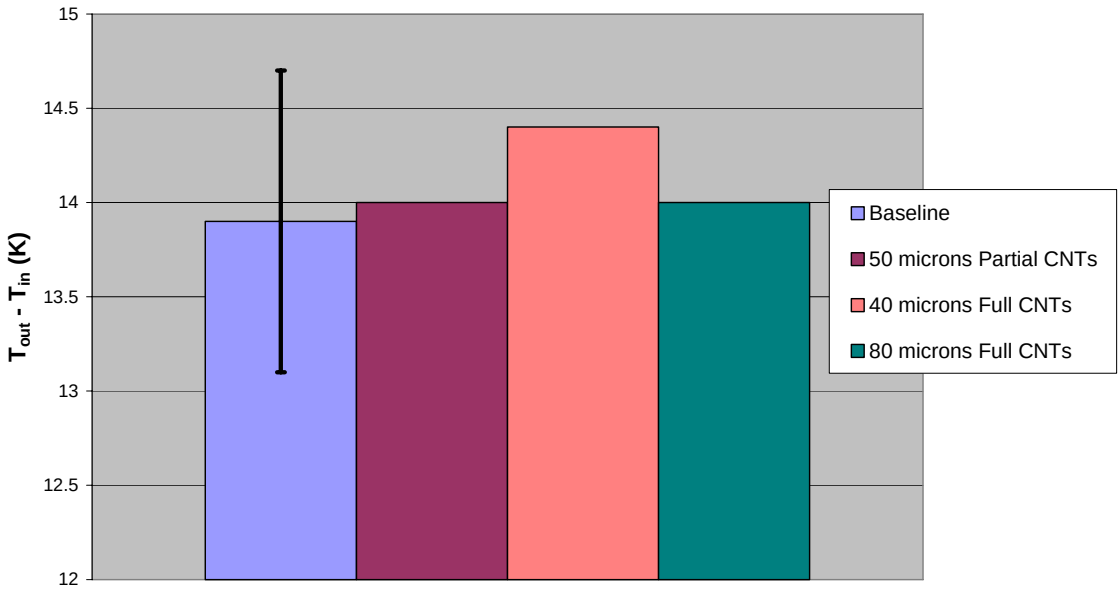

Figure 41: 30 W – 28 mL/min: steady-state water temperature rise with associated uncertainty band

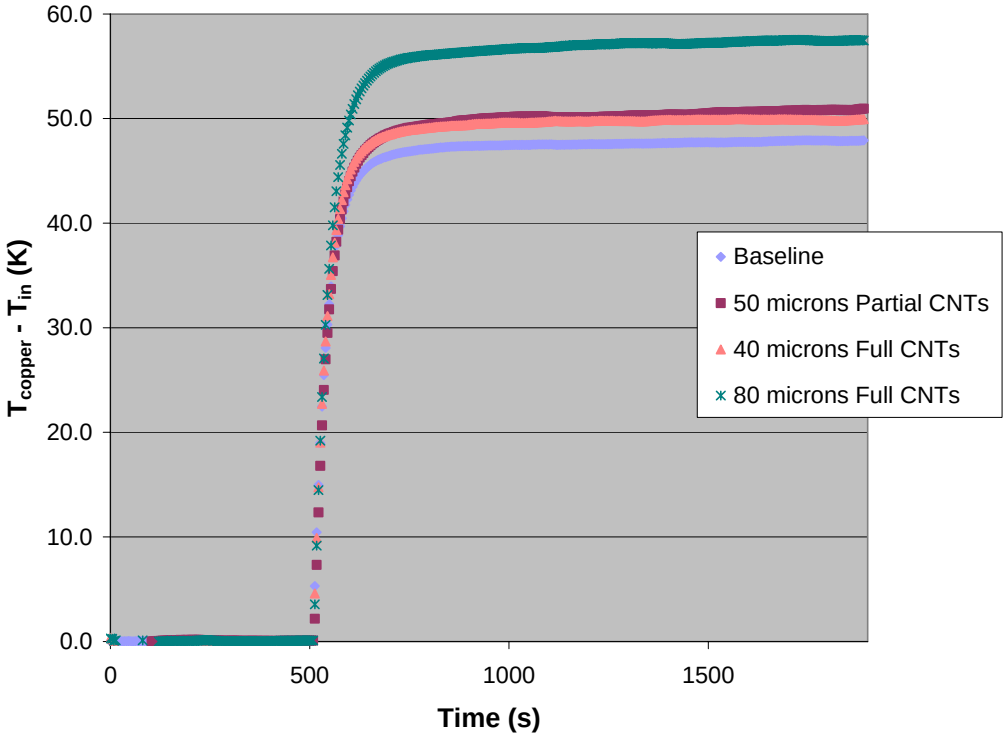

Figure 42: 30 W – 28 mL/min: transient heated region temperature rise

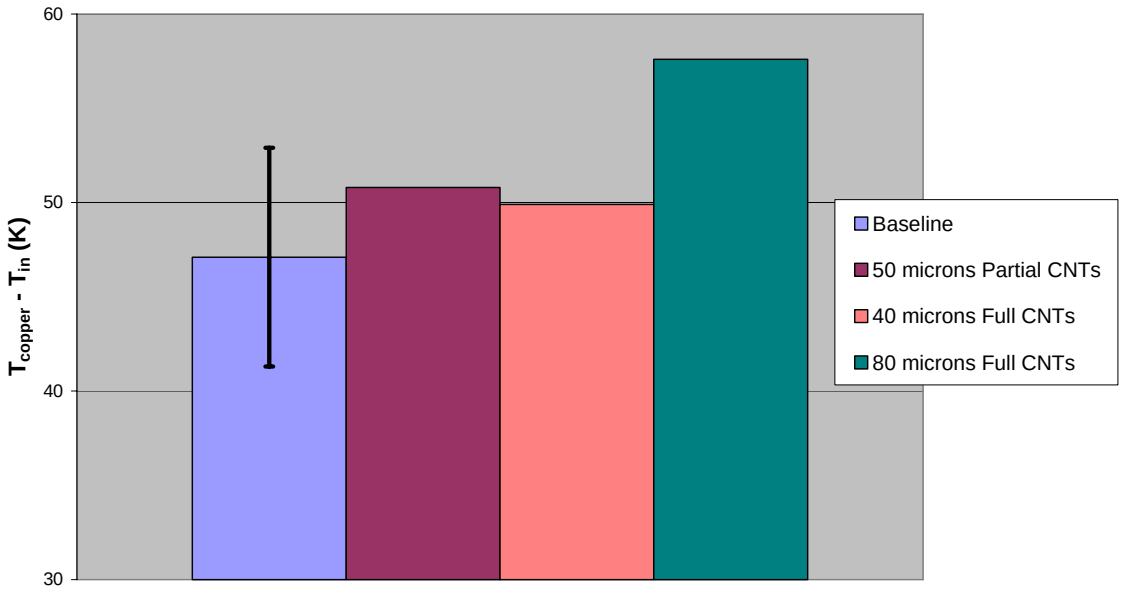

Figure 43: 30 W – 28 mL/min: steady-state heated region temperature rise with associated uncertainty band

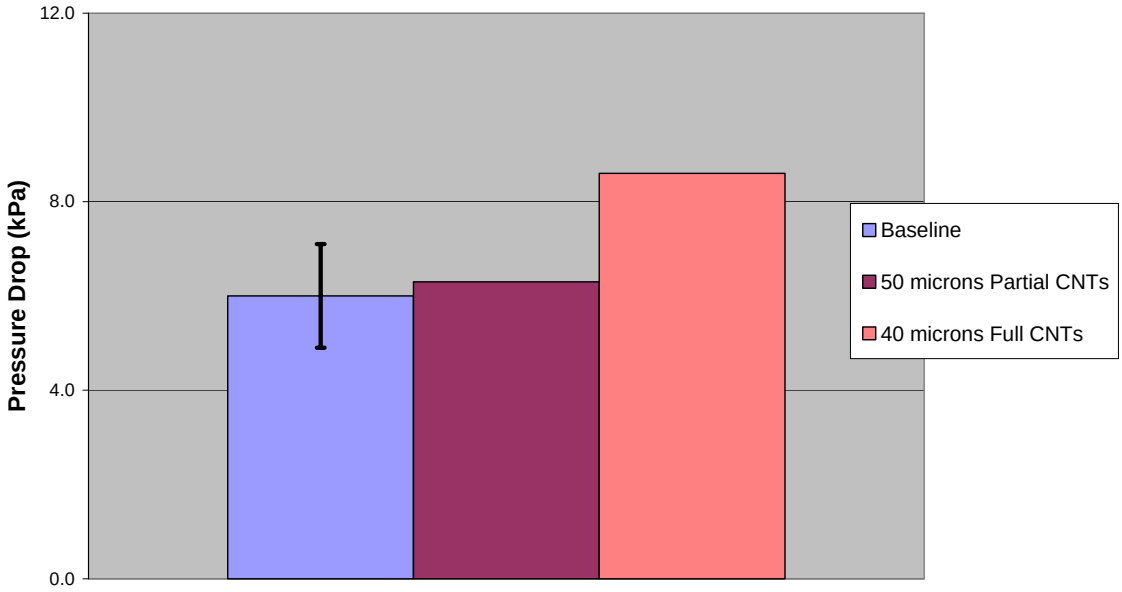

Figure 44: 30 W – 28 mL/min: steady-state total pressure drop with associated uncertainty band

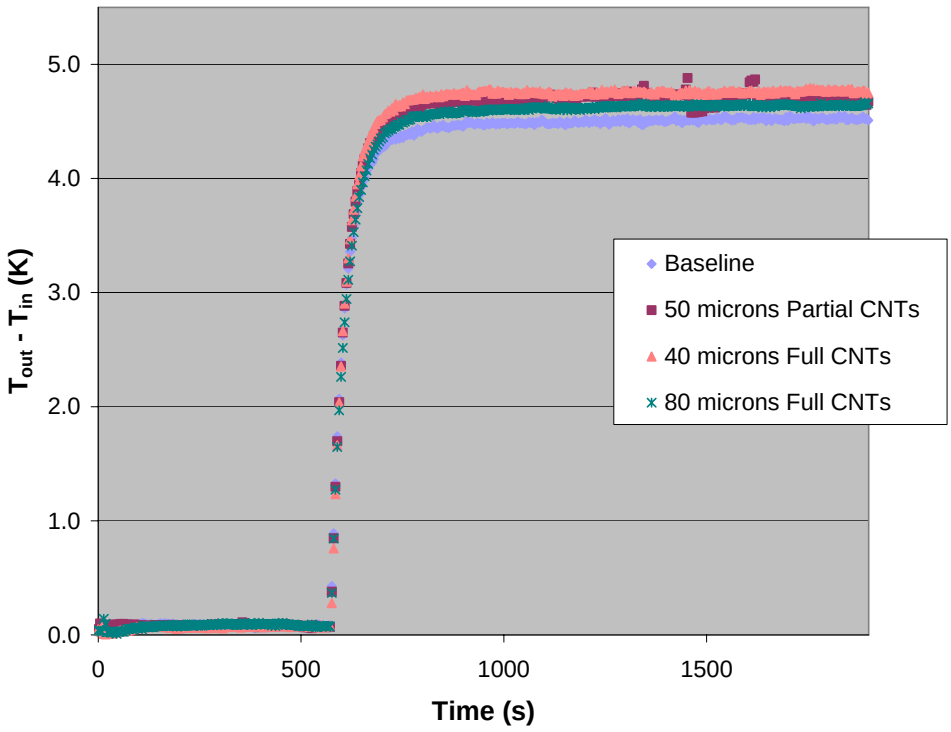

Figure 45: 10 W – 28 mL/min: transient water temperature rise

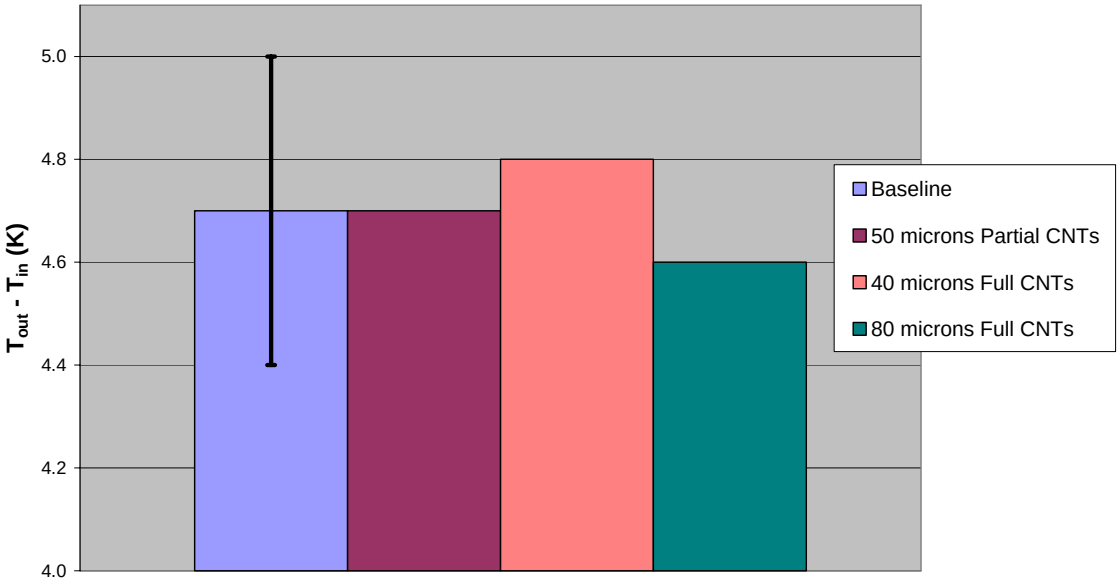

Figure 46: 10 W – 28 mL/min: steady-state water temperature rise with associated uncertainty band

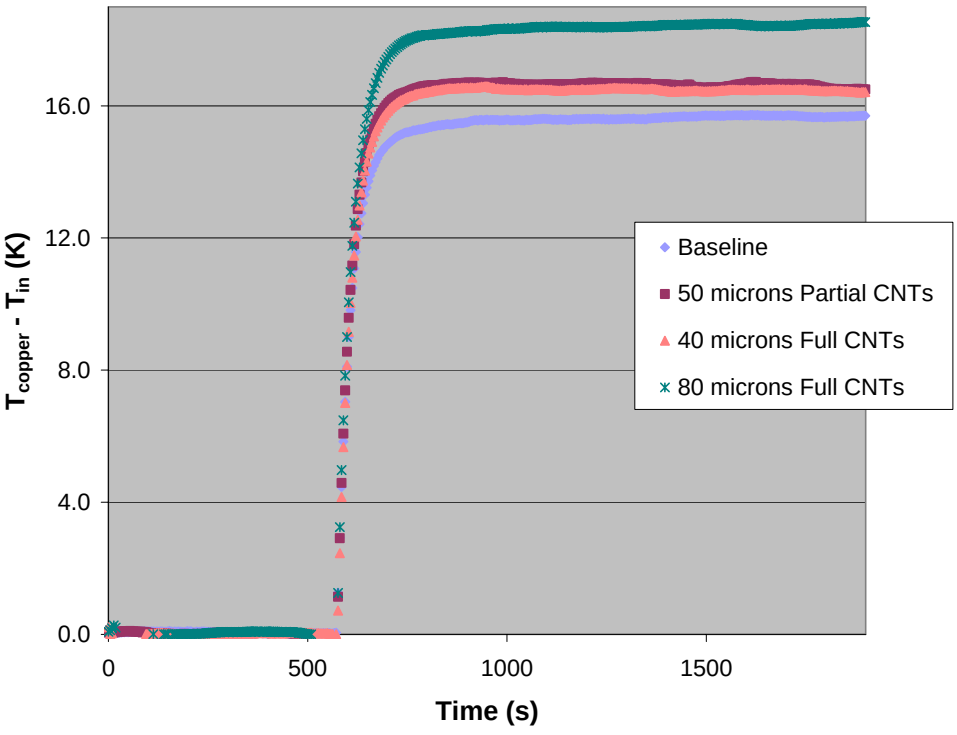

Figure 47: 10 W – 28 mL/min: transient heated region temperature rise

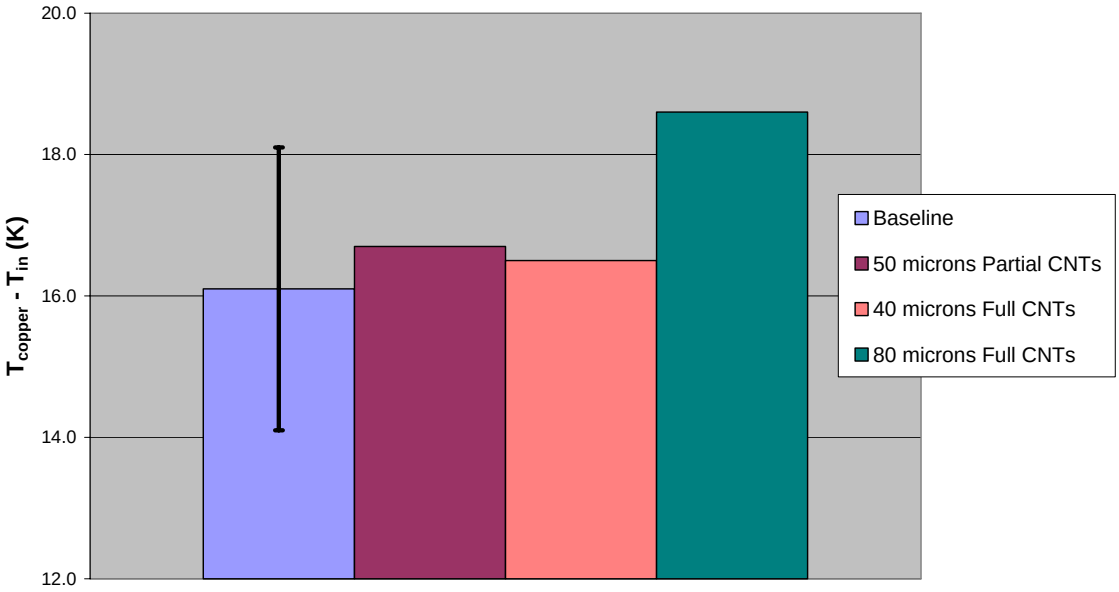

Figure 48: 10 W – 28 mL/min: steady-state heated region temperature rise with associated uncertainty band

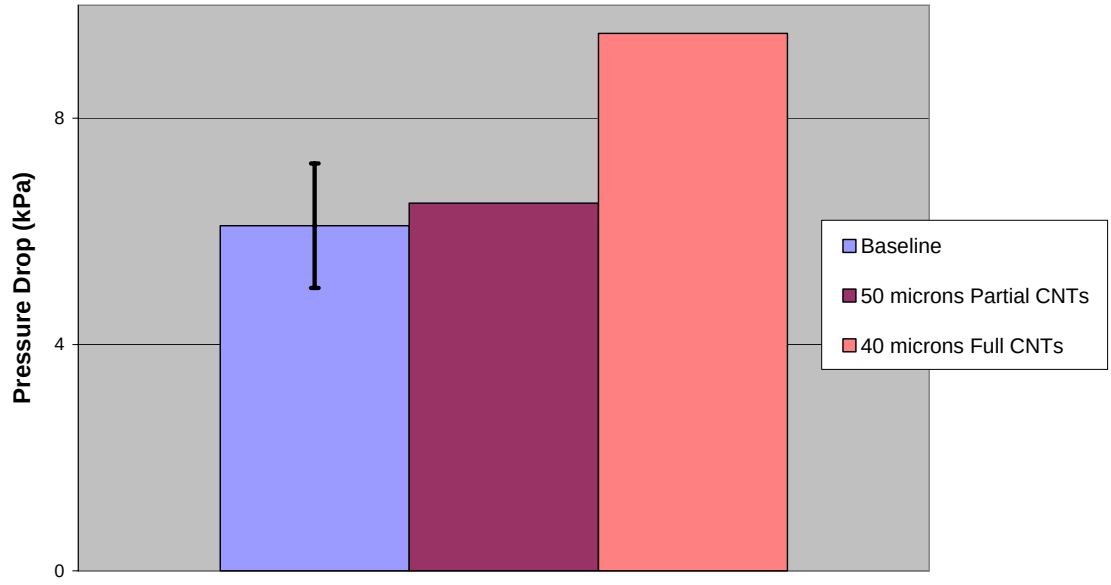

Figure 49: 10 W – 28 mL/min: steady-state total pressure drop with associated uncertainty band

3.4 Theoretical considerations

It may be expected that growing CNTs within a microchannel could increase heat transfer. Ideally, each CNT will act as a tiny pin-fin with axial thermal conductivity greater than diamond. CNTs could offer two mechanisms for improved heat transfer. They not only have a large aspect ratio, but a small diameter and pitch, which could lead to a large total surface area. Secondly, the large axial thermal conductivity should allow them to more effectively conduct heat away from the chip surface. The experimental results clearly show that using water as the working fluid is not beneficial. Therefore, these two mechanisms for heat transfer enhancement will be further outlined in the following sections to determine under what conditions incorporating CNTs in a microchannel would be beneficial.

3.4.1 Surface area effects

An idealized CNT configuration is presented in figure 50. In this configuration, the increase to surface area by including CNTs in a microchannel is investigated. A single channel was subdivided into a large number of smaller channels as a result of CNTs grown from the bottom to the top of the channel. A single CNT, 50 nm in diameter, acted as a channel wall. CNTs were at a 150 nm pitch, so that the working fluid flowed in between the gaps in the CNT array. The CNTs were assumed to be spaced to form channels, rather than in a pin-fin arrangement. Also, this analysis assumed the fluid remains in the continuum regime, was a single-phase, had a fully developed and laminar velocity profile, and wetted the CNTs. With this geometry and under these assumptions, the hydraulic diameter, defined in equation 17, is equal to $2*10^{-7}$ m. Therefore, the convective heat transfer coefficient, equation 19, equals $1.3*10^{8}$ $Wm^{-2}K^{-1}$, and consequential, the convection resistance, equation 11, equals $6.6*10^{-5}$ K/W.

$$h^* = \frac{Nu \cdot k^w}{D_h} \tag{15}$$

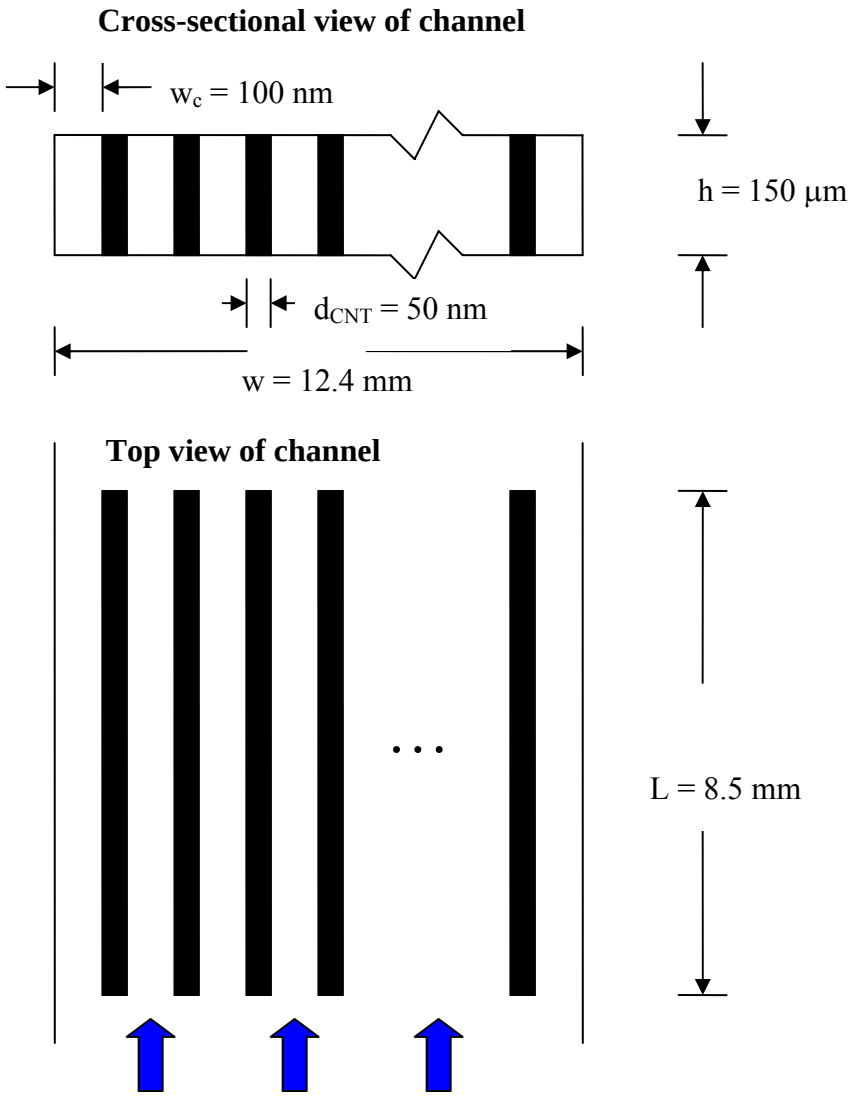

Figure 50: Idealized CNT microchannel geometry

As a result of the large surface area increase from the CNTs, the convective resistance is insignificant compared to the bulk flow resistance, which was calculated from equation 12 and is equal to 0.9 K/W. Therefore, the bulk flow resistance, and not the CNT surface area or thermal conductivity, becomes the limiting factor in single-phase, laminar flow, microchannel cooling.

Since the bulk flow resistance is based on the thermophysical properties of the fluid, investigating the thermal performance of several fluids is worthwhile to determine

the limits to heat transfer when the hydrophobic issue with CNTs is ignored. Although water did not enhance the thermal performance, which is attributed to the hydrophobic nature of the CNTs, there is a possibility that other fluids would wet the CNTs, or that a surfactant could be added to the water. With water as the working fluid, a 10 Wcm^{-2} heat flux and a 16 mL/min volumetric flow rate (0.26 g/s mass flow rate), water will experience a 10 K temperature rise. For the same heat flux and volumetric flow rate, air will experience a 31,700 K temperature rise. However, matching the pressure drop, rather than the volumetric flow rate, is a more appropriate metric for comparing different fluids. For this volumetric flow rate, water has a 2 GPa pressure drop. With a matching pressure drop, air will still have a 680 K temperature rise. Other fluids are analyzed in table 8. Water offers the lowest thermal resistance because of its desirable thermophysical properties: specific heat and thermal conductivity. Therefore, using surfactants, such as sodium dodecyl sulphate, could possibly allow water to wet the CNTs with only a minimum change to the thermophysical properties of water. However, water may still not wet the CNTs even in the presence of a surfactant. The surface of the CNT may naturally be very rough, and this would create a hydrophobic surface irregardless of the surface chemistry between water and a CNT.

On a final note, despite water having the lowest bulk thermal resistance of the fluids investigated, water still has a thermal resistance of 0.3 Kcm^2W^{-1}. Tuckerman and Pease, on the contrary, were able to obtain a 0.1 Kcm^2W^{-1} resistance using a silicon microchannel and water as the working fluid, while only creating a 0.35 MPa pressure drop [10]. Even if a fluid that wets the CNTs was used, CNTs do not grow in an optimal arrangement. For a fixed channel area, the addition of CNTs in a microchannel increases the convective heat transfer coefficient at the expense of an increasing pressure drop. Therefore, the large convective heat transfer coefficient that CNTs offer is larger than necessary, and CNTs do not enhance convective heat transfer.

Table 8: Bulk resistance for various fluids (ΔP = 2 GPa)

Property	Units	FC-72	FC-77	R-113	Silicone Oil	Air	Water
Density	kgm^{-3}	1680	1780	1510	950	1.17	997
Specific Heat	$Jkg^{-1}K^{-1}$	1050	1050	980	1630	1007	4179
Dynamic Viscosity	Nsm^{-2}	7.20E-4	1.44E-3	5.03E-4	2.90E-02	1.85E-05	8.91E-04
Boiling Point	°C	56	97	48	290	-	100
Bulk Resistance	Kcm^2W^{-1}	0.61	1.16	0.51	28.22	23.80	0.31

3.4.2 Thermal conductivity effects

Since the in situ growth of CNTs is not optimal for single-phase convective flows, growing CNTs in an optimal arrangement was investigated. Essentially, the CNTs were grown in bundles to form channel walls with a width of 200 μm, which is shown in figure 51. The high axial thermal conductivity of CNTs should increase the heat transfer compared to an optimally designed silicon microchannel. This investigation varies the channel wall thermal conductivity to determine the effects different channel wall thermally conductivities would have on the convective heat transfer. A resistor network was developed with resistances calculated from equations 20 to 26. The channel geometry was optimized by determining the resistances as functions of two non-dimensional geometric terms, α and β. The details of the optimization are taken from [47]. Single-phase, fully-developed, laminar flow, with a fixed pressure drop of 25 kPa, a fixed length of 1 cm and a fixed channel wall thickness of 200 μm was assumed. Figure 51 illustrates the geometry in consideration.

$$R_{Total} = R_{cond} + R_{constr} + R_{conv} + R_{bulk} \tag{20}$$

$$R_{cond} = \frac{t_{silicon}}{k_{silicon}} \tag{21}$$

$$R_{constr} = \frac{(1+\beta)}{\pi k_{CNT}} \ln\left[\frac{1}{\sin\left(\frac{\pi\beta}{2(1+\beta)}\right)}\right] \tag{22}$$

$$R_{conv} = \frac{1}{k^{w} Nu} \frac{(1+\beta)}{(1+2\alpha\eta_f)} \frac{2\alpha}{(1+\alpha)} \tag{23}$$

$$R_{bulk} = \frac{2L(1+\beta)}{c_p{}^{w} \mu^{w} \mathrm{Re}(1+\alpha)} \tag{24}$$

$$\alpha = \frac{H_c}{w_c} \tag{25}$$

$$\beta = \frac{w_w}{w_c} \tag{26}$$

Cross-sectional view of channel

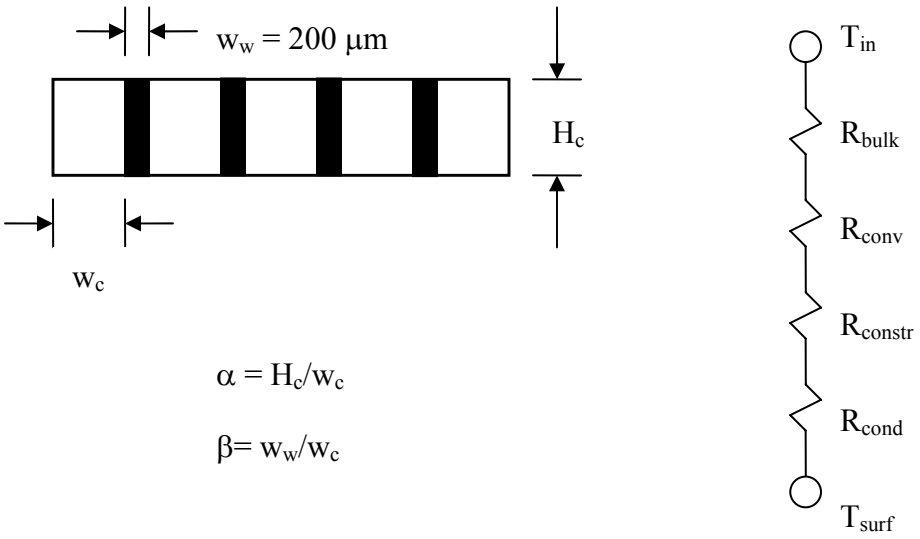

Figure 51: Channel geometry and resistor network for thermal optimization
The cross-section of the optimized channel is shown on the left. The thermal resistance network used for optimization is pictured on the right.

Identical to the earlier resistor network model, R_{cond} is due to the resistance through the silicon substrate, R_{conv} is the resistance of convection and R_{bulk} is the resistance due to the bulk temperature of the fluid increasing along the length of the channel. R_{constr}

accounts for two-dimensional heat transfer effects, in which the heat is constricted from the silicon substrate to the channel walls. The addition of R_{constr} in the thermal network assumes that all the heat is transferred to the channel fins before the heat is conducted to the fluid. This assumption is a conservative estimate of the thermal resistance but is still valid considering the surface area of the channel walls compared to the surface area of the channel base. The resistor network is represented pictorially in figure 51. It relates the temperature at the back surface of the silicon, to the inlet temperature of the working fluid.

Since the wall thickness, w_w, is fixed, the aspect ratio, α, was varied from 1 to 100 and channel height, H_c, was varied from 100 μm to 1200 μm. For a unique combination of α and H_c, the channel width, w_c, and β are predetermined. The optimization code calculated the total resistance for each combination of geometric parameters. The lowest total resistance was output, along with the corresponding geometric parameters. The channel thermal conductivity, which affects both R_{conv} and R_{constr}, was then adjusted and the code was run again. The thermal conductivities investigated in this study were 5, 50, 150, 200, 2000 and ∞ (numerical represented as 1E+8).

The 1200 μm tall channels had the lowest resistance, but only because they had the largest channel height of the heights that were investigated. The minimum resistance always corresponded to the largest H_c value. Therefore, the channel height was fixed at a specific value to further investigate the effects of channel wall thermal conductivity. For a given channel height, however, the code yielded an optimum aspect ratio that increases with increasing channel height. For channel heights between 100 μm and 800 μm, the aspect ratio scaled linearly with the channel height, so that the optimum channel width is 100 μm. For channel heights larger than 800 μm, the aspect ratio depends on the

thermal conductivity of the channel walls. When the channel height is fixed at 100 μm, with a channel wall thermal conductivity of 5 $Wm^{-1}K^{-1}$, the largest component of thermal resistance (56.8%) is due to the bulk fluid temperature rise. Convection is the second largest resistance (39.9%). For the same channel height, but with an infinite thermally conductive channel wall (represented as 10^8 $Wm^{-1}K^{-1}$), bulk resistance accounts for 60.2% of the total thermal resistance. Convection resistance is still the second largest and accounts for 38.7%. Therefore, highly conductive fins only marginally decrease the convective resistance. For a height of 100 μm, the total thermal resistance is insensitive to the fin thermal conductivity relative to other factors, predominately the channel height. As the channel height increases, the percentage of resistance due to convection decreases and the bulk resistance becomes the limiting factor.

Tables 9 to 12 list the optimized total resistance as a function of channel wall thermal conductivity and channel height. Corresponding chip temperature rise values are also presented for two separate heat fluxes; 100 Wcm^{-2} and 150 Wcm^{-2}. For channel heights between 100 μm and 800 μm, the total thermal resistance can be decreased more effectively by increasing the channel height, rather than by increasing the thermal conductivity of the channel walls. This result is attributed to the fin efficiency. A channel thermal conductivity of 50 $Wm^{-1}K^{-1}$ yields large enough fin efficiency so that minimal gains are made to the convective heat transfer by increasing the channel thermal conductivity. The convective heat transfer can be increased more effectively by increasing the channel surface area, i.e. using taller channels. Only when the channel height is above 800 μm does the effect of channel thermal conductivity become noticeable. However, even with a channel height of 1200 μm, channel walls consisting of silicon only have a 1-4 K higher chip temperature than channel walls consisting of CNTs. This analysis also ignores the economic factors of manufacturing and incorporating CNTs in a microchannel.

Table 9: Optimum thermal resistance for H_c = 100 μm

	Thermal Conductivity of Fins ($Wm^{-1}K^{-1}$)					
	5	50	150	200	2000	∞
Total Resistance (10^{-3} Km^2W^{-1})	0.1237	0.1175	0.1170	0.1170	0.1168	0.1168
Aspect Ratio	1	1	1	1	1	1
Chip Temperature Rise for 100 Wcm^{-2}	123.7	117.5	117.0	117.0	116.8	116.8
Chip Temperature Rise for 150 Wcm^{-2}	185.6	176.3	175.5	175.5	175.2	175.2

Table 10: Optimum thermal resistance for H_c = 400 μm

	Thermal Conductivity of Fins ($Wm^{-1}K^{-1}$)					
	5	50	150	200	2000	∞
Total Resistance (10^{-4} Km^2W^{-1})	0.4867	0.2970	0.2758	0.2730	0.2655	0.2646
Aspect Ratio	4	4	4	4	4	4
Chip Temperature Rise for 100 Wcm^{-2}	48.7	29.7	27.6	27.3	26.6	26.5
Chip Temperature Rise for 150 Wcm^{-2}	73.0	44.6	41.4	40.95	39.8	39.7

Table 11: Optimum thermal resistance for H_c = 800 μm

	Thermal Conductivity of Fins ($Wm^{-1}K^{-1}$)					
	5	50	150	200	2000	∞
Total Resistance (10^{-4} Km^2W^{-1})	0.3875	0.1925	0.1553	0.1499	0.1344	0.1326
Aspect Ratio	9	9	8	8	8	8
Chip Temperature Rise for 100 Wcm^{-2}	38.8	19.3	15.5	15.0	13.4	13.3
Chip Temperature Rise for 150 Wcm^{-2}	58.1	28.9	23.3	22.5	20.2	19.9

Table 12: Optimum thermal resistance for H_c = 1200 μm

	Thermal Conductivity of Fins ($Wm^{-1}K^{-1}$)					
	5	50	150	200	2000	∞
Total Resistance (10^{-4} Km^2W^{-1})	0.3496	0.1663	0.1234	0.1164	0.0940	0.0912
Aspect Ratio	14	14	13	13	12	12
Chip Temperature Rise for 100 Wcm^{-2}	35.0	16.6	12.3	11.6	9.4	9.1
Chip Temperature Rise for 150 Wcm^{-2}	52.4	24.9	18.5	17.5	14.1	13.7

CHAPTER 4

CONCLUSIONS AND RECOMMENDATIONS

4.1 Summary of findings

By incorporating CNTs into a silicon microchannel under single-phase, laminar flow, the CNTs cause an increase in pressure drop, as well as an increase in thermal resistance. The increase in pressure drop is attributed to CNTs impeding the flow, while the increase in thermal resistance is attributed to the contact resistance between the silicon and the CNTs, and the hydrophobic nature of CNTs. Also, if the CNTs are allowed to dry, due to capillary and van der Waals forces, the CNT structure appear to be permanently changed. Furthermore, even if a wetting fluid were used, the fluid properties are the limiting factor for heat transfer, as proved by theoretical predictions. The additional surface area that CNTs could potentially provide is not optimal for single-phase, laminar flows. Although the convective resistance is greatly reduced, the pressure drop increases. Finally, even with optimized channels, the high thermal conductivity of CNTs is irrelevant for microchannels. The thermal conductivity of silicon creates a large enough fin efficiency so that only a minimal gain in convective heat transfer is created by increasing the thermal conductivity of the channel wall. Highly thermally-conductive channel walls are only viable when the channel wall is greater than 800 μm. At these length scales, graphite, which has a thermal conductivity comparable to that of CNTs, could be used instead of CNTs.

4.2 Experimental refinement

After running several experiments, many possible changes were discovered that could be made to make the experiment runs more accurate, efficient, and simpler. Due to

time limits, equipment usage requirements and cost, these ideas were never incorporated in the current study. Although the current work is more than satisfactory for testing heat transfer capabilities of microchannels, this section serves as a recommendation for future experimental studies if there is a desire to further reduce the experimental uncertainty. The first improvement would be to replace the cartridge heater and copper block with an integrated heater fabricated directly on the backside of the sample. The integrated heater is formed by depositing platinum in a serpentine pattern to create a resistor. The platinum resistor is then thermally and electrically insulated by depositing a layer of silicon dioxide on the platinum. Contact pads are opened in the silicon dioxide, and the resistor is electrically connected to a chip package by wire bonding. Several issues with the copper block are then avoided. The thermal interface material between the heater and the sample is eliminated, the heat loss to the surroundings is reduced and no mechanical alignment is necessary between the sample and the heater. The drawback is that the microfabrication process time increases; therefore, an integrated heater may only be desirable when the number of samples used for testing is low, or the yield and through-put from the fabrication are high.

A second recommendation would be to only use D.C. power. Although D.C. power supplies are more expensive and generally larger than A.C. power supplies, fluctuations in the power are eliminated. These power fluctuations lead to fluctuations in the temperature measurements at steady-state, which lead to large precision uncertainties. To check the effects of using an AC power supply, a DC power supply was used to supply 10 W to a silicon device. 10 W was the maximum amount of power from the DC power supply; therefore, not all of the tests in this current study could be run using a DC power supply. The water temperature rise and heated region temperature rise values were experimentally comparable to the values measured using an AC power supply. However, the uncertainty (P=95) in the input power measurement was decreased from 0.3 W for an AC power supply to 0.001 W for a DC power supply. Since the fluctuations in input

power were a major source of uncertainty, a DC power supply could be used to reduce the experimental uncertainty. Another source of fluctuations in the steady-state values was caused by the pulsation due to the peristaltic pump. The dampener was able to eliminate the majority of the flow pulsation, but further steps could be made. A helium tank, controlled by a throttling valve, could be used to pressurize the water at the inlet. Helium should be used because it has a low solubility in water, and it is inert. Since the throttling valve can keep the pressure of the helium constant, a more uniform flow would develop. The helium could also be used to degas the water. Although vacuum degassing worked consistently, the decrease in water temperature during degassing is a major deterrence from using that particular method. By flowing helium through the water, the advection of the helium removes the dissolved air in the water. Helium can then be used to keep the water under a reduced environment until experiments are ready to be run. At that time, the helium would be used to drive the flow.

Another major issue with determining thermal performance of microchannels is accurately measuring the surface temperature. Although thermocouples can be considered common practice, there are issues associated with contact resistance and uncertainty in the spatial placement of the thermocouples that can make their use less desirable. As previously mentioned for an integrated heater, integrated temperature sensors can be patterned on the backside of the sample using the same method. However, instead of applying a voltage across the resistive element, the resistance of the element is measured. The measured resistance can then be calibrated to an absolute temperature. Therefore, precision placement of the temperature sensing element is obtainable, and the use of integrated temperature sensors lowers the contact resistance. The fabrication and use of integrated heaters and temperature sensors is further outlined in [48]. Again, the major shortcoming with this particular method of measuring surface temperature is the time necessary to calibrate the temperature sensors. If a large number of samples needs to be tested, each new sample would have to be individually calibrated, which is a

considerable amount of work. A second option for measuring the surface temperature is to use an infrared (IR) camera. Silicon is transparent in the near IR range, and water is opaque. Therefore, an IR camera could be used to measure the emissions due to temperature at the water-silicon interface. There is, however, a real-estate issue, in which the IR camera would have to make measurements on the same side as the heater. And so, an accurate measurement may not be possible because of the interference from the heater. The use of an IR camera to study the surface temperature is explained in [49].

4.3 Further investigations

From the channel optimization analysis, convective heat transfer is not the limiting factor for microchannel cooling. The bulk resistance is the major issue, and therefore, fluidic properties become the key component for single-phase, laminar microchannel cooling. CNTs, because of their high axial thermal conductivity and large surface area to volume ratio, could be well suited as the suspended solid in a nanofluid [50]. The other major resistance, which was determined through experiments, is the thermal resistance created by the TIM layer. The TIM layer resistance was three times the bulk resistance. Better TIMs are critical to get benefits from increased convective heat transfer performance for the current experiments.

Another way to improve the current implementation of CNTs is to reduce the pressure drop. A major detriment to the thermal performance of CNT enhanced microchannels was the increased flow resistance. For a pressure driven flow with a fixed pressure drop, the CNTs decreased the convective heat transfer resistance while increasing the bulk resistance. This resulted in a net increase in the total thermal resistance. Therefore, using positive displacement or electro-osmosis driven flows instead of a pressure driven flow may lead to thermal enhancements, because the pressure drop does not have as strong of a functional dependence on the hydraulic diameter. For non-pressure driven flows, the bulk resistance would not increase as much, and thus, the

decrease in convective heat transfer resistance may create a net decrease in the total resistance. In addition to using non-pressure driven flows, drag reducing polymers could also be used to reduce the pressure drop. [51] used polyethylene glycol in laminar electro-osmotic flows to reduce viscous drag by 50%.

Aside from using CNTs to improve single-phase, laminar microchannel cooling, CNTs can be used in other heat transfer technologies. For example, CNTs have been demonstrated to be effective as part of boiling enhancement structures [52]. Their large surface area to volume ratio may increase the number of nucleation sites, and their hydrophobic nature could potentially enhance the nucleation per unit area. Furthermore, CNTs may be well suited for stacked microchannel cooling. Stacked microchannels decrease the pressure drop because the fluid flows through multiple parallel paths. The optimum number of stacked microchannels for a maximum heat removal is a function of the thermal conductivity of the substrate. For silicon, the optimal number of stacked microchannels is two [48]. Since CNTs channel walls could replace the silicon channel walls, there may be an increase in the number of stacked channels used. Therefore, the pressure drop could be further reduced, while maintaining a similar thermal performance.

APPENDIX A

MICROFABRICATION

A.1 Wafer cleaning

Double-sided polished, 350 μm thick, 100 mm diameter silicon, <100> oriented wafers ordered from Montco Silicon Technologies were used to make the devices. Before any processes were carried out, a RCA (Radio Corporation of America) clean was done. The clean is a two-step process usually denoted as RCA I and RCA II. Table A.1 lists the process details. Essentially, the RCA I cleans the wafer of any organic residue. An intermittent wafer dip in hydrofluoric acid (HF) was done so that the native oxide layer on the silicon was etched, which in turn, removed any ions imbedded in the oxide. The RCA II then further cleaned the wafer of free ions.

Table A.1: RCA clean recipe

Step	Parameter	Process
RCA I	Ratio	5:1:1
	Chemicals	H_20:H_2O_2:NH_4OH
	Temperature (°C)	75
	Time (min)	15
Intermittent	Ratio	20:1
	Chemicals	H_20:HF
	Temperature (°C)	22
	Time (s)	10
RCA II	Ratio	6:1:1
	Chemicals	H_20:H_2O_2:HCl
	Temperature (°C)	75

Table A.1: continued

	Time (min)	15

A.2 Photolithography

Photolithography is the method of transferring an image from one medium to another using a polymer known as photoresist. Photoresist is generally comprised of three components: a resin base, a solvent to control the phase and viscosity of the resist, and a photo active compound (PAC) that changes the solubility of the resist in a specific solution once light at a specific wavelength is absorbed. Photolithography can be classified as either positive or negative based on its behavior once it is exposed to light. Whenever positive resist is exposed to light, the light breaks the bonds in the polymer and makes the exposed region soluble in a developer. Negative resist, on the other hand, becomes non-soluble in a developer once it is exposed to light because the light causes the polymers to cross-link.

There are normally five steps in a photolithography process: application, soft bake, exposure, development and hard bake. During the application step, the photoresist is deposited on the wafer using a pipette. The wafer is then spun on a CEE 100CB spinner at a specific rpm rate and for a certain amount of time. Both parameters, spin speed and time, control the resulting thickness of the resist. Spinning is used because the variations in resist thickness across the wafer are minimized. The next step is referred to as 'soft baking'. The wafer is placed in an oven so that the resist hardens. Essentially, the solvent that controls the phase and viscosity is evaporated. Then, the wafer is placed in the Karl Suss MA-6 (MA6) mask aligner. The mask aligner is an optical microscope that allows for precision alignment between a mask and the wafer and has an ultraviolet (UV) bulb that provides a certain intensity at a specific wavelength.

After the substrate has been exposed to UV light, the substrate is ready for development. The substrate is placed in a specific solvent, depending on what type of resist was used. The solvent will dissolve the exposed regions for positive resist or unexposed for negative resist.

Following the development step, a final hard bake is done. The hard bake hardens the resist so that the substrate does not damage other equipment in the clean room. Several machines use mechanical clamps to hold wafers in place, and uncured photoresist can cause the substrate to stick to the clamp.

Table A.2 outlines the recipes, in sequential order, that were used for all photolithography steps. There are some exceptions. First of all, both AZ 1500 and Shipley 1825 are positive resists; however, NR-9-8000 is negative, and so, the hard bake process step is performed before the development step. Also, the AZ 1500 was factory applied, so the photolithography process of this resist begins at the exposure step.

Table A.2: Photoresist recipes

		Photoresists		
Process Step	Parameters	AZ 1500	Shipley 1827	NR-9-8000
Moisture Bake	Temperature (°C)	-	115	110
	Time (s)	-	300	300
Application	Amount (g)	-	7	9
	Spin Speed (rpm)	-	4000	3000
	Spin Rate (rpm/s)	-	1000	1000
	Time (s)	-	60	30
Soft Bake	Temperature (°C)	-	115	110
	Time (min)	-	5	15
Exposure	Energy Flux (mJ/cm^2)	21.5	21.5	5.0

Table A.2: continued

	Wavelength (nm)	405	405	365
	Time (s)	7.5	8.5	35
	Alignment Gap (μm)	-	20	20
	Contact Type	Hard	Hard	Hard
Development	Developer	DI H_20: AZP4620 3:1	MF-319	RD6
	Time (s)	120	120	60
Hard Bake	Temperature (°C)	-	120	90
	Time (min)	-	30	2

A.3 Mask making

The AutoCAD drawings were exported as a *.ai file and sent to Pageworks, a document company. Pageworks created transparencies of the files using 5080 dots per inch (dpi) Herkules image setter. The transparencies were inspected under an optical microscope, and no pin holes were detected.

Mask blanks, purchased from Telic, were used to transfer the image on the transparencies to a hard mask through the photolithography procedure outlined above. The mask blanks are square, 0.6 mm thick, soda lime glass and measure 125 mm on a side. Chrome was sputtered on top of the glass, and then AZ 1500 photoresist was spun on top of the chrome.

The mask blank was placed in the MA6 on a standard wafer holder. The transparency was placed on top of the mask blank, and then soda lime glass was placed on top of the transparency to keep the transparency flat. The lamp test function of the MA6 was used to provide a blanket exposure. After the mask blank was exposed, it was placed in a plastic container with diluted AZ400K developer purchased from AZ Electronics. After the exposed photoresist had been dissolved, the mask blank was

removed and rinsed with DI water and dried with a nitrogen (N_2) air gun. Next, the mask blank was placed in a plastic container with CR-7S, chromium etchant. The unexposed photoresist acted as a mask for selected areas of the chrome, so that only the chrome in the photoresist developed regions was etched. The chrome was etched completely to expose the soda lime glass. This completes the image transfer process. A cleanup was then performed, which involves using acetone and other solvents to strip the remaining photoresist, followed by another DI water rinse and N_2 dry.

A.4 Oxide deposition

The wafers were cleaned after using the RCA process outlined in section A.1. After the cleaning, the wafer was then placed in the Unaxis, a Plasma Enhanced Chemical Vapor Deposition (PECVD) system. The Unaxis deposited silicon dioxide (SiO_2) on the wafers through a combination of specific gases and high temperature. The details of this process can be seen in table A.3. To increase throughput, four wafers were placed in the Unaxis each run. After both sides of the wafer had been deposited with SiO_2, the Nanospec, a refractometer, was used to measure the thickness of the oxide. The thicknesses for various runs are listed in table A.4.

After the oxide thickness had been determined, the first photolithography step (PR 1) was carried out using the mask shown in figure A.1. PR 1 uses the recipe for Shipley 1825 photoresist.

Table A.3: Unaxis PECVD process

Step Name	Parameter	Value
Initial	Pressure (Torr)	0.01
	Hold Time (s)	10
	Heat Exchanger Temperature (°C)	60
	Watlow Temperature (°C)	250

Table A.3: continued

Gas Stabilization	Time (s)	60
	Flow Rate of SiH_4 (sccm)	400
	Flow Rate of N_20 (sccm)	900
	Pressure (mTorr)	900
Deposition	Time (min)	28
	Rate (Å/s)	537.7
	Flow Rate of SiH_4 (sccm)	400
	Flow Rate of N_20 (sccm)	900
	Power (W)	25
Nitrogen Purge	Time (min)	5
	Pressure (mTorr)	100

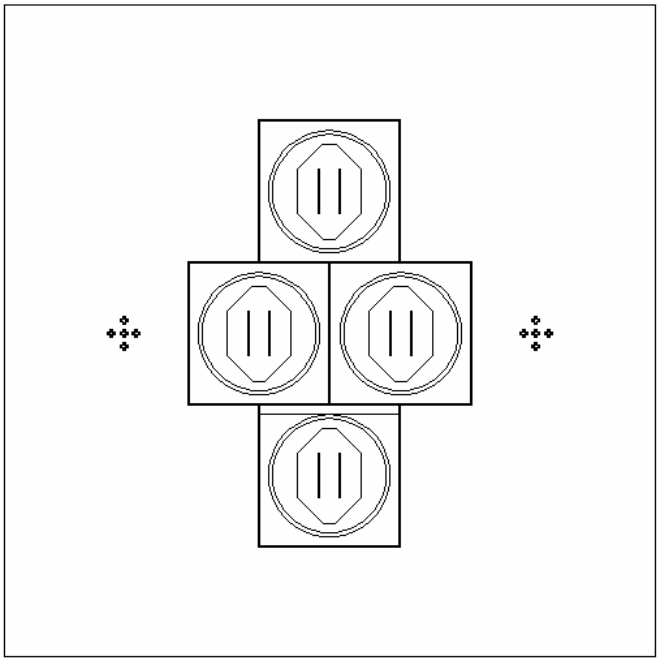

Figure A.1: Mask for PR 1

Table A.4 Silicon dioxide thicknesses

	Thickness (μm)	
Wafer	Front	Back
1	1.54	1.56
2	1.52	1.56
3	1.54	1.57
4	1.55	1.54

A.5 Etching

Following the hard bake of the PR 1 recipe, the wafers were once again placed in the Nanospec. Not only does the Nanospec list the thickness of various layers, but it also lists a fitting parameter to show how pure the layer is. Therefore, a check can be done to determine if the photoresist has been completely developed. The fit should be very close to the fit that was measured before the PR 1 process. After this checked had been made, the wafer was then mounted to a carrier wafer, which is simply another wafer of the same thickness. The wafer was attached to the carrier wafer using thermal grease. Since the wafer is thinner than standard silicon wafers, ~500 μm, the wafer may break during the etching process, and therefore, a carrier wafer was used to provide mechanical support. Furthermore, the thermal grease was used between the two wafers because heat removal occurs on the backside of the carrier wafer. The thermal grease lowers the thermal contact resistance between the wafer being etched and the carried wafer. If heat is not effectively removed, then the etching may not be uniform across the wafer.

The wafer was placed in the Plasma-Therm, an Inductively Coupled Plasma (ICP) machine to selectively remove the deposited SiO_2. The SiO_2 will act as a mask for the Si etching. The selectivity between Si and SiO_2 is two orders of magnitude greater than the selectivity between Si and photoresist. Therefore, the photoresist is used to pattern the

SiO_2 and the SiO_2 acts as a mask for the Si. The ICP uses two power sources, one to generate plasma and one to accelerate ions towards the surface of the wafer. The acceleration allows for anisotropic etching with a 3:1 selectivity between the SiO_2 and photoresist. The SiO_2 was removed through a combination of momentum transfer and chemical reaction. The gases along with the processing details are listed in Table A.5.

After the oxide etching step, several cleaning procedures were carried out in order to meet the strict usage requirements for the STS ICP. The STS ICP has the greatest selectivity of silicon over SiO_2 of all the ICPs in the clean room, and therefore, it is the most desirable for silicon etching. First, the wafer was separated from the carrier wafer with a razor blade, and acetone was used to remove the residual grease. Then, the protective photoresist that acted as a mask for the SiO_2 etching was removed by heating a solvent, Stripper 1165, on a hotplate to 70 °C. Next, a RCA II clean was used to remove ions, and finally, the wafer was remounted to the carrier wafer, again using thermal grease.

The wafer was then placed in the STS ICP. The process details are listed in table A.6. Similar to SiO_2 etching, silicon etching is done physically and chemically. In order to generate high aspect ratios or deep channels with straight walls, the Bosch process was used. This process is cyclic, in which a chemical, SF_6, is first used to etch the wafer, and then a polymer, C_4F_8, is deposited on the wafer.

Table A.5: Plasma Therm ICP SiO_2 etching

Step Name	Parameter	Value
Initial	Pressure (Torr)	0.01
	Hold Time (s)	10
	Heat Exchanger Temperature (°C)	60
Evacuation	Pressure (mTorr)	5

Table A.5: continued

	Time (s)	40
Gas Stabilization	Time (s)	30
	Flow Rate of H_2 (sccm)	2
	Flow Rate of CF_4 (sccm)	25
	Pressure (mTorr)	5
Deposition	Time (min)	16
	Flow Rate of H_2 (sccm)	2
	Flow Rate of CF_4 (sccm)	25
	RF Power 1 (W)	70
	RF Power 2 (W)	250
Pump Down	Time (min)	5
	Pressure (mTorr)	5

Table A.6: STS ICP Si etching

Step Name	**Parameter**	**Value**
Process Step	*General*	
	Phase Start	Passive
	Phase End	Etch
	Number of Cycles	180
	Etch Time per Cycle (s)	11
	Passivate Time per Cycle (s)	8
	Total Time (min)	57
	Pressure	
	Base Pressure (mTorr)	0.1
	Pressure Trip (mTorr)	94

Table A.6: continued

	APC Setting			68.4%	
	APC Mode			Manual	
	Gases				
		Etch		Passivate	
	Gas	Flow (sccm)	Tolerance (%)	Flow (sccm)	Tolerance (%)
	C_4F_8	0	50	100	50
	SF_6	130	50	0	5
	O_2	13	50	0	5
	Air	0	5	0	5
	R.F. Power				
				13.56 MHz Coil	13.56 MHz Platen
	Etching Power (W)			800	10
	Passivation Power (W)			600	0
	Tolerance (%)			50	50
	Matching Auto			On	On
	Matching Lead (%)			35	50
	Matching Tune (%)			45	50
	Helium Back-Side Cooling (HBC)				
	HBC Active			Yes	
	He Flow Pressure (mTorr)			1000	
	He Flow Tolerance (%)			25	
	He Max Flow (sccm)			40	
	He Min Flow (sccm)			10	

Table A.6: continued

	Helium Leak-Up Test	
	Test Active	Yes
	Time (s)	30
	Max Leak (mTorr/min)	20

A.6 Channel depth determination

Once again, several cleaning procedures were performed before the next major process step was carried out. The wafer was separated from the carrier again, and acetone was used to remove the thermal grease. The wafer was then placed in the Gastronics Asher to remove the residual C_4F_8 on the channel walls. The Asher generates oxygen plasma, which is a standard method for the removal of C_4F_8 and other polymers. The wafer was then placed into a plastic container holding hydrofluoric acid (HF). HF completely strips the wafer of the oxide mask that had been used. Ashing is done prior to the HF dip because HF reacts with C_4F_8 and causes C_4F_8 to harden. Hardened C_4F_8 cannot be removed from the side walls of the wafer.

At this point, channel depth measurements were conducted using the Tencor KLA profilometer. The results are summarized in table A.7. The notations are seen in figure A.2. South, West, East and North refer to the device on the wafer, with South being the wafer nearest the primary flat and West being the wafer nearest the secondary flat. Each device has three channels labeled left, center or right. Finally, the channel depth was measured at different locations on a specific channel. These locations are referred to as top, middle or bottom. As seen in table A.7, the channels are very consistent not only across a single device, but also across the entire wafer and from wafer to wafer. Finally, surface roughness at the bottom of the channel was measured and determined to be, through averaging, between 0.5 μm and 1 μm.

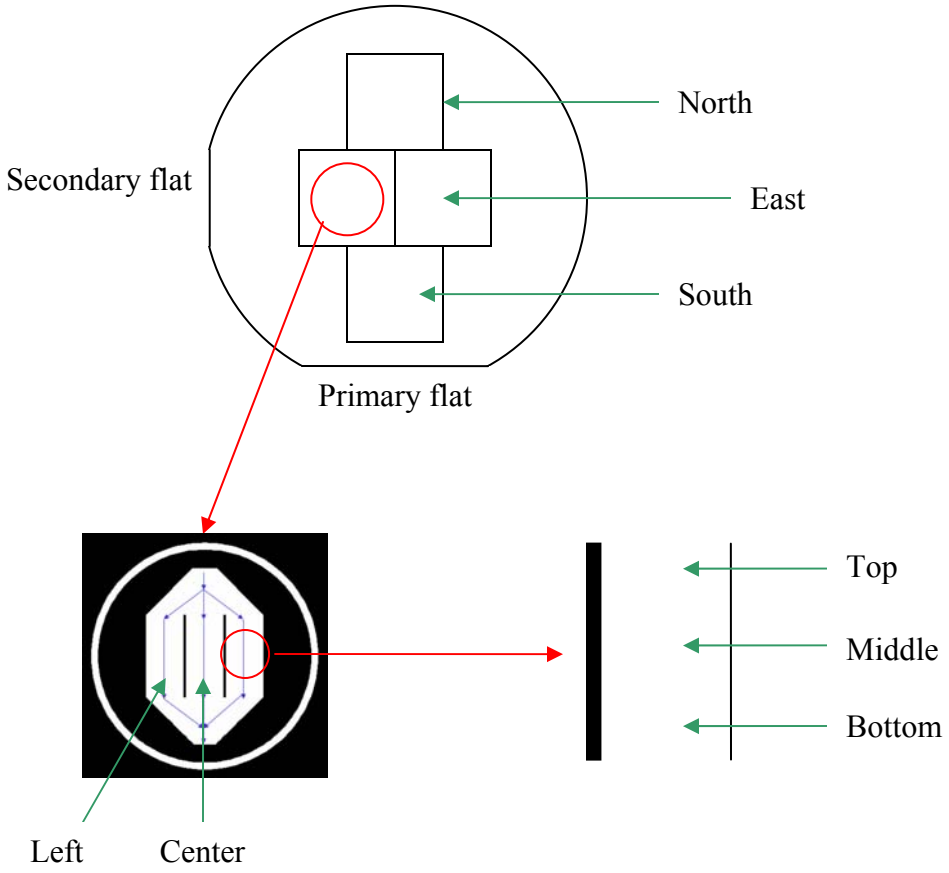

Figure A.2: Profilometry measurement locations

Table A.7: Channel depth uniformity

Wafer	Device	Channel	Location	Depth (μm)
1	West	Left	Middle	155.3
1	West	Left	Top	155.8
1	West	Center	Top	151.4
1	West	Center	Middle	150.9
1	West	Right	Middle	150.2
1	North	Left	Top	154.1
1	North	Center	Middle	149.1

Table A.7: continued

1	South	Center	Middle	149.9
1	East	Center	Middle	150.5
2	West	Center	Middle	154.2
2	North	Center	Middle	153.3
2	East	Center	Middle	154.2
2	South	Center	Middle	153.3
3	West	Center	Middle	149.7
3	North	Center	Middle	148.5
3	East	Center	Middle	147.8
3	South	Center	Middle	149.1

A.7 Metallization

If the wafer was to be used as a baseline wafer, i.e. with no CNT deposition, the following process steps were omitted, the wafer was diced and the cover plate was bonded, as described in section A.8 and A.9 respectively. Otherwise, the following steps were carried out to prepare the wafer for CNT growth.

Three different CNT growth recipes were conducted as an attempt to repeatedly grow tall CNTs. The first growth recipe involves the following steps. First, a layer of oxide was deposited on the silicon using the Unaxis. Then, the second photolithography step (PR 2) was carried out using the same recipe for Shipley 1827 and the mask seen in figure A.3. Afterwards, the wafer was placed back in the Plasma Therm ICP left chamber to etch selected areas of the oxide. This process deposited oxide only on the bottom surface of the channels.

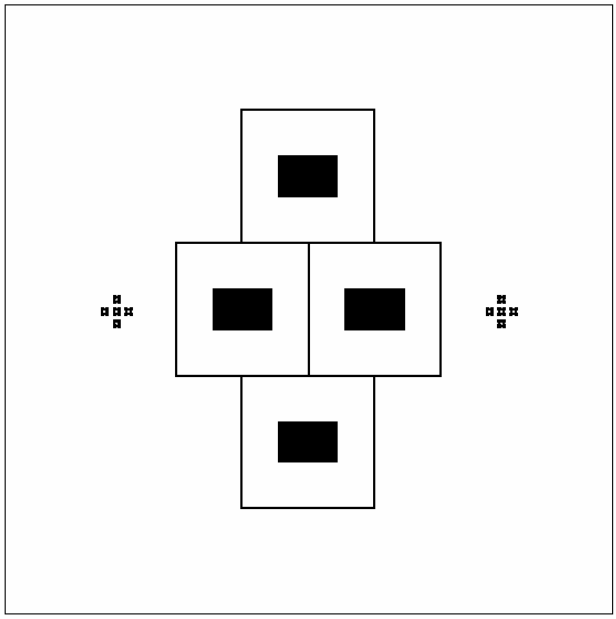

Figure A.3: Mask for PR 2 and PR 3

With the oxide layer deposited, PR 3 was carried out using the recipe for NR-9-8000 and the same mask as in PR 2. However, since negative resist was used, the recently deposited oxide was exposed, while the rest of the wafer was protected.

The wafer was then placed in the CVC electron beam evaporator (e-beam). The e-beam uses an electron beam to heat up a crucible containing metal. The metal evaporates and is deposited through a direct line of sight method. Therefore, the process is conducted under very low vacuum to lessen the probability that the metal vapor will collide with gas atoms inside the chamber. Also, since the metal is evaporating, the wafer is placed upside down and above the metal target. Using this process, iron, which acts as the catalysis for CNT growth, was deposited on the wafer. The resulting height of the CNTs is a function of the catalysis thickness; therefore, different iron thicknesses were investigated in order to optimize CNT height. Some samples had a 6.0 nm thick iron layer and others had a 10.0 nm thick iron layer. The parameters used for the e-beam can be seen in table A.8. After iron was deposited, the wafer was then cleaned with acetone. This processed is referred to as lift-off. Acetone dissolves the photoresist that is still on

the wafer, and thus, all the metal that was just deposited is 'lifted-off' except for the regions where the photoresist was developed.

The second CNT growth recipe omits the SiO_2 deposition and PR 3 was immediately carried out. The wafer was then placed in the e-beam, and aluminum was deposited on the wafer. Iron was then deposited on top of the aluminum. The lift-off process was again carried out, but now the aluminum and iron that was deposited on remaining photoresist was removed. The final CNT growth recipe is similar to the second recipe except instead of depositing aluminum, titanium was deposited. The deposition patterns for aluminum and titanium can also be seen in table A.8.

Table A.8: CVC e-beam evaporator process

Metal	Chamber Pressure (Torr)	Rate (Å/s)	Thickness (nm)
Iron (Fe)	$1.9*10^{-6}$	0.5	6.0 or 10.0
Titanium (Ti)	$1.9*10^{-6}$	0.5	20.0
Aluminum (Al)	$1.9*10^{-6}$	0.5	20.0

A.8 CNT deposition

After metallization, the wafer was diced in the Micro Thermal Systems lab using the Disco automatic dicing saw. A resin composite blade with a diamond edge was used to dice the wafers. The blade spins at 30,000 rpm and is capable of cutting the wafer in any direction, regardless of the crystalline structure. With the devices separated from each other, they were placed in the Easy Tube furnace in the Management and Metrology of MEMS Devices lab or in the Easy Tube furnace at the Georgia Technology Research Institute.

The Easy Tube is a sealed chamber that allows for simultaneous flow of four separate gases, while applying a high temperature to the chamber. The process parameters are listed in table A.9, where the flow of argon only occurred during the heat up and cool down phases, not during the actual growth. The temperature for all runs varied between 720 °C and 820 °C. Also, the process time varied between 10 and 45 minutes, and two acetylene flow rates were investigated.

Table A.9: CNT template recipe

Gas	Flow Rate (sccm)
Methane	1000
Hydrogen	500
Argon	500
Acetylene	100

A.9 Cover plate attachment

A quartz microscope slide purchased from Fisher Scientific was used as the cover plate. The slide was diced on the wafer dicing saw so that the slide had the same surface area as the device. In order to deliver the working fluid to the microchannel, inlet and outlet holes were drilled through the Pyrex. To do this, a square with the same dimensions as the quartz cover plate was drilled into a block of wood. The square hole in the wood held the quartz in place as the quartz was drilled. Then, modeling clay was used to form an enclosure around the perimeter of the quartz. Finally, water was deposited on top of the quartz, and the modeling clay prevented any leaks. Glass drilling was performed with special diamond tipped mandrel bits and with water as a lubricant. The drilling was done on a mill so that precision holes could be drilled.

To direct fluid from the flow loop to the holes in the cover plate, plastic tubing was fitted around a 6.5 mm long piece of glass capillary tubing so that only 1 mm of the glass capillary tubing was exposed. The glass capillary tubing was attached to the quartz cover plate using a Norland optical adhesive (NO68). The outer diameter of the capillary tube is the same as the inner diameter of the holes drilled in the quartz, so a small amount of N068 was placed around the perimeter of the exposed glass capillary tubing, and the capillary tubing was placed in the quartz hole. Since the quartz is 1 mm in thickness, the plastic tubing was pressed flush against the top of the Pyrex. NO68 hardens when it is exposed to UV light. Once the NO68 was applied and the parts properly set, a UV light was turned on and the sample was exposed for 5 minutes. The end result was a leak-proof seal.

The cover plate assembly was then attached to the silicon device using N068. Once again, a 5 minute exposure was used. NO68 requires a one week full-cure at room temperature after the 5 minute exposure; however, the cure was facilitated by heating the sample on a hotplate at 50 °C after it was exposured. The microfabrication is now complete and the devices are ready for testing.

A.10 PDMS cover plate manufacturing

Since growing CNTs inside a microchannel was difficult, as discussed in section 3.1.1, growing the CNTs on a flat silicon substrate and manufacturing the microchannels in the cover plate was considered. The only constraint on the cover plate material is that it needs to bond well to silicon. Polydimethylsiloxane (PDMS) not only bonds well to silicon, but using rapid prototyping techniques, PDMS can be easily molded [47]. A master mold was made in Solid-Edge CAD software. The file was then exported to the stereolithography machine in the Manufacturing Related Complex (MaRC) building. PDMS was then formed into a cover plate and bonded to a silicon substrate as outlined in [53]. Upon testing however, the deformation of PDMS made sustaining a constant

pressure drop difficult. As a result, the volumetric flow rate, and consequentially the system temperatures, varied greatly and no further investigations into using PDMS cover plates was made.

APPENDIX B

UNCERTAINTY ANALYSIS

The experimental measurements used to compare the various samples are the outlet temperature, heated region temperature and pressure drop. Therefore, only the variations in the system that cause fluctuations in these three quantities needed to be identified and analyzed for a complete uncertainty analysis of the experimental setup. The pressure drop will change as a result of variations in the volumetric flow rate and variations in the sample geometry. The height of the channel, surface roughness of the channel and the bonding of the channel vary from sample to sample and would cause variations in the pressure drop. Using equation 11, the channel pressure drop can be determined. The uncertainties in the mass flow rate and channel geometry can be propagated to find the uncertainty in the channel pressure drop measurement using equation B.1.

$$\delta R^2 = \left(\frac{\partial R}{\partial x_1}\delta x_1\right)^2 + \left(\frac{\partial R}{\partial x_2}\delta x_2\right)^2 + \ldots + \left(\frac{\partial R}{\partial x_N}\delta x_N\right)^2 \qquad \text{(B.1)}$$

R is the result of interest, i.e. the pressure drop, and x_1 through x_N are factors that R depends on, i.e. the mass flow rate and the geometry. δ represents the uncertainty of a particular parameter. The variations in the channel height were determined in section A.6. The uncertainty in the volumetric flow rate was determined by setting the rotameter to the desired flow rate and using a mass balance and a fixed time interval to measure the flow rate. The uncertainty was 0.5 mL/min for the 16 mL/min flow rates and 0.7 mL/min for the 28.4 mL/min. The uncertainty analysis for the pressure drop was extended to include the piping and manifolds by using the pressure results from the model and the

experimental measurement of the piping pressure drop. A loss coefficient was determined for the piping pressure drop and the manifolds. Using this loss coefficient the variations of volumetric flow rate could be determined. The geometric variations were negligible compared to the variations in the volumetric flow rate.

The outlet temperature and heated region temperature uncertainties were determined in a similar manner to the pressure drop variations. The outlet temperature is dependent on the volumetric flow rate and the input heat flux. The uncertainty in the input heat flux was determined by calculating the standard deviation of the input heat flux for all similar testing conditions. The heat input had an uncertainty of 0.3 W for the 10 W test cases and an uncertainty of 0.7 W for the 30 W test cases. The uncertainties in the volumetric flow rate and heat input were propagated using equation B.1, where R is given by equation B.2.

$$\Delta T_{water} = \frac{Q_{input}}{\dot{m} c_p^{\ w}} \tag{B.2}$$

Finally, the heated region temperature not only depends on the input heat flux and mass flow rate, but also on the channel geometry and the thickness of the TIM. The uncertainty in the TIM was determined by measuring the TIM thickness multiple times. The thickness of the TIM was measured to be 70 μm and the variation in TIM thickness was 14 μm. The uncertainty of the TIM thickness was largest contributor to the uncertainty of the heated region temperature measurement. The uncertainty in the heated region temperature measurement was determined by using equation B.1 again, where R is now given by the resistor network developed in section 3.3.2.

Once the uncertainty is determined for a particular quantity from equation B.1, the result is multiplied by a coverage factor to improve the confidence level. The in situ result from equation B.1 gives a 66% confidence, i.e. if the above experiment was repeated, the measured result would lay within the uncertainty bounds 66% of the time.

A 95% confidence level is achieved by multiplying the result from equation B.1 by a factor of two. A 99% confidence level is given by multiplying be a factor of three. The 95% confidence level for both the single-sample uncertainty and the comparison among samples uncertainty for all intermittent system parameters is given in table B.1. The single-sample uncertainty predicts the probability that the next data point for a given experimental run will vary inside the uncertainty bounds. The comparison uncertainty predicts the probability that a separate experimental run will have a mean value inside the uncertainty bounds.

Table B.1: Uncertainties (P=95)

10 W 16 mL/min				
Measurements	**Units**	**Average**	**Single-sample**	**Comparison**
$\dot{m}$	mL/min	15.7	-	0.5
T_{in}	K	296.2	0.2	0.8
Re	-	49	-	3
P	W	10.1	0.5	0.3
Q_{input}	W	9.5	0.2	0.3
$\Delta P_{channels}$	Pa	600	-	100
ΔP_{total}	kPa	3.0	0.1	0.4
ΔT_{water}	K	8.8	0.0	0.6
ΔT_{copper}	K	17.0	0.2	2.0
Resistances				
R_{TIM}	K/W	0.909	-	0.17
R_{cond}	K/W	0.013	-	0.0025
R_{conv}	K/W	0.803	-	0.026
R_{conv} with one manifold	K/W	0.599		0.026
R_{conv} with two manifolds	K/W	0.477		0.026
R_{bulk}	K/W	0.306	-	0.0097
Metrics				
Energy Ratio	-	0.91		0.06
Nu	-	5.4		2.0
h^*	W/m^2K	11000		4000

Table B.1: continued

30 W 16 mL/min				
Measurements	**Units**	**Average**	**Single-sample**	**Comparison**
$\dot{m}$	mL/min	15.7	-	0.5
T_{in}	K	296.1	0.2	0.8
Re	-	56	-	3
P	W	30.2	1.8	0.7
$Q_{in\_thermal}$	W	28.2	0.3	0.9
$\Delta P_{channels}$	Pa	500	-	60
ΔP_{total}	kPa	2.8	0.1	0.4
ΔT_{water}	K	24.7	0.2	1.8
ΔT_{copper}	K	50.1	0.5	6.2
Resistances				
R_{TIM}	K/W	0.909	-	0.17
R_{cond}	K/W	0.013	-	0.0025
R_{conv}	K/W	0.788	-	0.026
R_{conv} with one manifold	K/W	0.587		0.026
R_{conv} with two manifolds	K/W	0.468		0.026
R_{bulk}	K/W	0.307	-	0.0097
Metrics				
Energy Ratio	-	0.90		0.05
Nu	-	5.4		1.5
h^*	W/m^{2}K	11000		3000

30 W 28 mL/min				
Measurements	**Units**	**Average**	**Single-sample**	**Comparison**
$\dot{m}$	mL/min	28.4	-	0.7
T_{in}	K	296.1	0.2	0.8
Re	-	93	-	5
P	W	30.2	1.7	0.7
$Q_{in\_thermal}$	W	28.2	0.2	0.9
$\Delta P_{channels}$	Pa	1000	-	100
ΔP_{total}	kPa	6.0	0.2	1.1
ΔT_{water}	K	13.7	0.2	0.8
ΔT_{copper}	K	46.7	0.3	5.8

Table B.1: continued

Resistances				
R_{TIM}	K/W	0.909	-	0.17
R_{cond}	K/W	0.013	-	0.0025
R_{conv}	K/W	0.797	-	0.026
R_{conv} with one manifold	K/W	0.594		0.026
R_{conv} with two manifolds	K/W	0.473		0.026
R_{bulk}	K/W	0.169	-	0.0019
Metrics				
Energy Ratio	-	0.91		0.05
Nu	-	5.4		2.7
h^*	W/m^{2}K	11000		6000

10 W 28 mL/min				
Measurements	**Units**	**Average**	**Single-sample**	**Comparison**
$\dot{m}$	mL/min	28.4	-	0.7
T_{in}	K	296.1	0.154	0.8
Re	-	86	-	4
P	W	10.1	0.6	0.3
$Q_{in\_thermal}$	W	9.5	0.122	0.3
$\Delta P_{channels}$	Pa	1100	-	100
ΔP_{total}	kPa	6.1	0.2	1.1
ΔT_{water}	K		0.0	0.3
ΔT_{copper}	K		0.1	2.0
Resistances				
R_{TIM}	K/W	0.909	-	0.17
R_{cond}	K/W	0.013	-	0.0025
R_{conv}	K/W	0.806	-	0.026
R_{conv} with one manifold	K/W	0.601		0.026
R_{conv} with two manifolds	K/W	0.479		0.026
R_{bulk}	K/W	0.169	-	0.0019
Metrics				
Energy Ratio	-	0.92		0.05
Nu	-	5.4		3.7

Table B.1: continued

h^*	W/m^2K	11000		8000

APPENDIX C

CARBON NANOTUBE CHARACTERIZATION DETAILS

C.1 Carbon nanotube growth parameters

The height and orientation of the CNTs are a function of the catalyst thickness, hydrocarbon gas flow rates, growth time and the growth temperature. The adhesion strength to the surface is a function of the substrate material. One should note that there may be other potential parameters for the height, orientation and adhesion. For example, the adhesion strength may also depend on growth temperature and time. The main premise of this study is not to determine an optimal CNT growth recipe, and because of this, the above parameters are the only ones that were considered. Due to the previous work of Stephan Turano under the supervision of Jud Ready at GTRI and Erik Sunden under the advisement of Dr. Samuel Graham, a template recipe for CNT growth already existed for a silicon wafer with 500 nm of silicon dioxide deposited on the surface. All the parameter variations were modified from this template, which was previously described in section A.8.

C.2 Carbon nanotube orientation and height

In general, CNTs will self-align during growth so that their axes are normal to the surface as long as the density of growth nucleation sites is large enough. The reason behind aligned growth is due to the strong van der Waals interactions between adjacent nanotubes. If there are a high number of concurrently grown CNTs, they have to grow vertically because that is the only available free space for growth. Aligned growth was shown in figure 11. On the other hand, if the number of growth sites is low, the nanotubes may still be long from the perspective of their arc length, but their height (total vertical

distance above the surface) will be very low. The CNTs tend to create a 'spaghetti-like' bundle on the surface, which was shown figure 12.

Table C.1 lists the various combinations of parameters and the resulting height of the CNTs, where substrate condition refers to if the CNTs were grown on a plain wafer or if the CNTs were grown inside the microchannels with either partial coverage (p) or full coverage (f). All metal layers had a thickness of 20 nm. Furthermore, one sample initially had 20 nm of Al deposited on the surface. The sample was then set on a hotplate at 100 °C for 20 minutes so that the Al would oxidize. 10 nm of iron was then deposited on the oxidized Al layer. This sample is represented by the asterisk. The flow rates of methane, argon and hydrogen were constant. The accuracy of the height measurement is ±10 μm (P=95). The accuracy was determined based on the length scale associated with the magnification of the SEM images and the expected uncertainty from visually placing the software measurement markers.

On a final note, all tubes grown at 740 °C were grown in a chamber that could have been contaminated with o-ring pieces from the mass flow controllers. The results from these tests should not be used to determine correlations between the growth parameters because the data is not reliable. After the chamber was found to be contaminated, a new furnace was used. Finally, the parameters that resulted in the tallest CNTs inside the microchannel, approximately 80 μm, were a temperature of 820 °C and a time of 30 minutes.

Table C.1: CNT growth conditions and results

Substrate and Seed Layer	Catalysis Thickness (nm)	Growth Time (min)	Growth Temperature (°C)	Substrate Condition	CNT Height (μm)
Si – Al	10	20	740	non-etched	55-80
Si – Al	10	20	740	non-etched	50-70

Table C.1: continued

Si – Al	10	20	740	non-etched	90-136
Si – Al	10	20	720	non-etched	45
Si – Al*	10	20	720	non-etched	80
Si – Ti	10	20	740	non-etched	no tubes
Si - SiO_2 - Ti	10	20	740	non-etched	no tubes
Si – Ti – Al	10	20	740	non-etched	no tubes
Si - SiO_2	10	20	720	non-etched	160
Si - SiO_2	10	20	740	non-etched	130-190
Si - SiO_2	10	20	740	non-etched	90
Si - SiO_2	10	10	720	non-etched	85
Si – Al	10	20	740	etched (p)	40
Si – Al	10	20	740	etched (p)	30
Si - SiO_2	10	30	720	etched (p)	no tubes
Si - SiO_2	10	25	760	etched (p)	50
Si – Al	10	20	740	etched (f)	no tubes
Si – Al	10	20	740	etched (f)	no tubes
Si - SiO_2	10	10	720	etched (f)	2 (not aligned)
Si - SiO_2	10	20	720	etched (f)	40
Si - SiO_2	6	40	780	etched (f)	no tubes
Si - SiO_2	6	30	820	etched (f)	80
Si - SiO_2	6	30	820	etched (f)	40
Si - SiO_2	6	30	820	etched (f)	120

C.3 Carbon nanotube adhesion strength

As previously stated, the CNT adhesion strength to the surface is dependent on the substrate. Therefore, combinations of various substrates were used including, titanium-iron, aluminum-iron, titanium-aluminum-iron, and SiO_2-iron. The methodology behind using aluminum and titanium is that when these materials are subjected to high temperatures, silicon and these metals form a strong bond. Ideally, the strong bond between the metal seed layer and the silicon should translate into a strong bond between the CNT and the surface.

A simple experiment was run in which CNTs were grown on the aforementioned substrates. Since only two of the above processes, Si – SiO_2 and Si – Al, yielded CNTs, these were the only two samples that could be tested. The samples were then subjected to a shear stress, which was supplied by an air gun. The results are documented in figure C.1. The CNTs grown on the SiO_2 sample were easily dislodged from the substrate. However, the CNTs grown on Si – Al had no visible detachment from the surface. Based on the experiment, the samples with the metal seed layer have greater bond strength to the substrate than the samples grown on SiO_2.

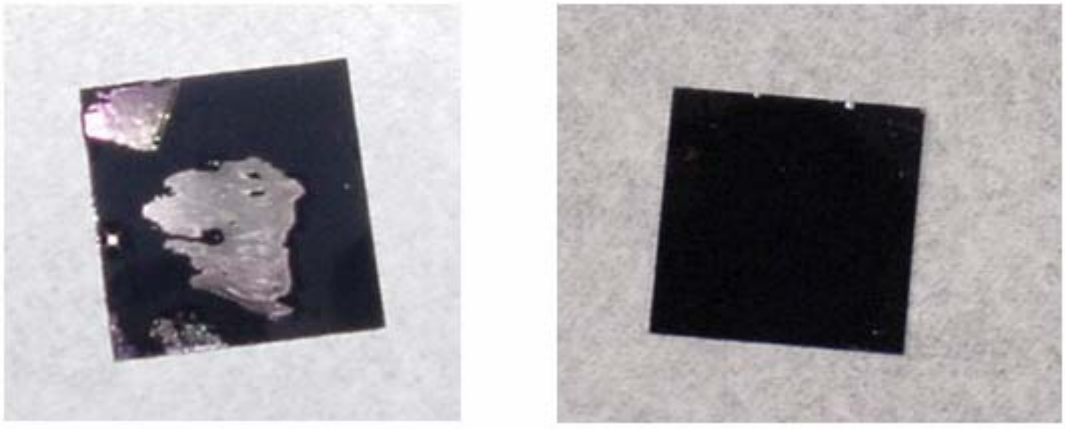

Figure C.1: CNT adhesion
The figure on the left has CNTs grown on SiO_2. The CNTs have been dislodged from the substrate. The sample on the right has CNTs grown on iron. The CNTs are visibly still intact.

APPENDIX D

THERMAL RESISTANCE OPTIMIZATION MATLAB CODE

```
%Carter Dietz
%Optimum Thermal Design
clear all;
close all;
clc;
format long;

%Constants
L = 1*10^-2;
t = 200*10^-6;
cp = 4180;
rho = 996.5;
mu = 857*10^-6;
k_water = 613*10^-3;
k_s = 148;
Ww = 200*10^-6;
P = 25*10^3;
R_cond = t/k_s;

%Parameters
alphb = 1:1:101; %Varying aspect ratios
alpha = alphb';
k_cnt = [5, 50, 150, 200, 2000, 10^8]; %Varying channel thermal conductivities

%Input channel height
Hc = 100*10^-6;

%Predetermined geometry based on above inputs
for i = 1:length(alpha)
   Wc(i) = Hc/alpha(i);
   beta(i) = Ww/Wc(i);
   R_total(i) = 0;
end


%Equations
for k = 1:length(k_cnt)
   R_total_old(k) = 10;
```

```
for i = 1:length(alpha)

    %Calculate bulk resistance
    D = (2*alpha(i)*Wc(i))/(1+alpha(i));
    diff = 1;
    V = 0.5;
    %Determine velocity by iterating
    while diff > 0.000001
       Re = (rho*V*D)/mu;
       f = 24*(1 - 1.3553*alpha(i)^-1 + 1.9467*alpha(i)^-2
       - 1.7012*alpha(i)^-3 + 0.9564*alpha(i)^-4 - 0.2537*alpha(i)^-5)/Re;
       if f < 0
          Vnew = V;
       else
          Vnew = sqrt((P*D)/(2*f*L*rho));
       end
       diff = abs(Vnew - V);
       V = Vnew;
    end
    if Re > 2200 || f < 0  || Re < 1
       R_bulk = 10;
    else
       R_bulk = (2*L*(1+beta(i)))/(cp*mu*Re*(1+alpha(i)));
    end

    %Calculate convective resistance
    Nu = 8.235*(1 - 2.0421*alpha(i)^-1 + 3.0853*alpha(i)^-2
    - 2.4765*alpha(i)^-3 + 1.0578*alpha(i)^-4 - 0.1861*alpha(i)^-5);
    if Nu < 0
       R_conv = 10;
    else
       h = Nu*k_water/D;
       m = sqrt((2*h)/(k_cnt(k)*Ww));
       eta = tanh(m*Hc)/(m*Hc);
       R_conv =
((1+beta(i))*2*alpha(i)*Wc(i))/(Nu*k_water*(1+2*alpha(i)*eta)*(1+alpha(i)));
    end

    %Calculate constriction resistance
    R_constr =
((1+beta(i))/(pi*k_cnt(k)))*log(1/sin((pi*beta(i))/(2*(1+beta(i)))))*Wc(i);

    %Calculate total resistance
    R_total(i) = R_bulk + R_conv + R_constr + R_cond;

    %Store minimum resistance
```

```
            if R_total(i) < R_total_old(k)
                Row(k) = i;
                R_total_old(k) = R_total(i);
            end
        end
end

%Output
for k = 1:length(k_cnt)
    Aspect(k) = alpha(Row(k));
end
Aspect
R_total_old'
```

REFERENCES

[1] http://www.intel.com.products/processor/itanium2/ (March 2007).

[2] International Technologies Roadmap for Semiconductors (2006). http://public.itrs.net/

[3] Koo, J., S. Im, E. S. Cho, R. S. Prasher, E. Wang, L. Jiang, A. Bari, D. Campion, D. Fogg, M. S. Kim, T. W. Kenny, J. G. Santiago, K. E. Goodson (2002). VLSI Hot Spot Cooling Using Two-Phase Microchannel Convection. *Proceedings of the ASME Process Industries Division*, Vol. 7, 13-19.

[4] Faulkner, D. J., R. Shekarriz (2003). Forced Convective Boiling in Microchannels for KW/cm^2 Electronics Cooling. *Proceedings of the 2003 ASME Summer Heat Transfer Conference*, Vol. 2, 329-336.

[5] Khan, N., D. Pinjala, K. C. Toh (2004). Pool Boiling Heat Transfer Enhancement by Surface Modification / Micro Structures for Electronics Cooling: A Review. *Proceedings of the 6th Packaging Technology Conference*, 273-280.

[6] Hegde, P. M. Z. Abdullah, K. N. Seetharamu, P. A. A. Narayana (2006). Counter and Parallel Two-Phase Flow Microchannel Heat Sinks for Electronics Cooling. *International Journal of Heat Exchangers*, Vol. 7, No. 1, 57-74.

[7] Nguyen, C. T., G. Roy, C. Gauthier, N. Galanis (2007). Heat Transfer Enhancement Using Al_2O_3-Water Nanofluid for an Electronic Liquid Cooling System. *Applied Thermal Engineering*, Vol. 27, No. 8-9, 1501-1506.

[8] Narumanchi, S. V. J., D. Bharathan, V. Hassani (2005). Comparison of Different Single-Phase Liquid Jet Impingement Cooling Configurations in the Context of the Thermal Management in Power Electronics. *Proceedings of the ASME/Pacific Rim Technical Conference and Exhibition on Integration and Packaging of MEMS, NEMS, and Electronic Systems: Advances in Electronic Packaging 2005*, Vol. A, 577-590.

[9] Narumanchi, S. A. Troshki, V. Hassani, D. Bharathan (2006). Numerical Simulations of Boiling Jet Impingement Cooling in Power Electronics. *Tenth Intersociety Conference on Thermal and Thermomechanical Phenomena and Emerging Technologies in Electronic Systems, ITherm 2006*, 204-214.

[10] Tuckerman, D. B., and R. F. Pease (1981). High Performance Heat Sinking for VLSI. *IEEE Electron Device Letters*, Vol. EDL-2, No. 5, 126-129.

[11] Wu, P. Y., and W. A. Little (1983). Measurement of Friction Factor for the Flow of Gases in Very Fine Channels Used for Microminiature Joule-Thompson Refrigerators. *Cryogenics*, Vol. 23, No. 5, 273-277.

[12] Pfaher, J. N., J. Harley, H. H. Bau, and J. Zemel (1991). Gas and Liquid Flow in Small Channels. *Micromechanical Sensors, Actuators and Systems*, ASME DSC-32, 49-60.

[13] Peng, X. F., G. P. Peterson (1996). Convective heat transfer and flow friction for water flow in microchannel structures. *International Journal of Heat and Mass Transfer*, Vol. 39, No.12, 2599-2608

[14] Xu, B., K. T. Ooi, N. T. Wong (2000). Experimental Investigation of Flow Friction for Liquid Flow in Microchannels. *International Communications in Heat and Mass Transfer*, Vol. 27, No. 8, 1165-1176.

[15] Lee, P., S. V. Garimella, D. Liu (2005). Investigation of Heat Transfer in Rectangular Microchannels. *International Journal of Heat and Mass Transfer*, Vol. 48, 1688-1704.

[16] Liu, D., S. V. Garimella (2004). Investigation of Liquid Flow in Microchannels. *Journal of Thermophysics and Heat Transfer*, Vol. 18, No. 1, 65-72.

[17] Iijima, S. (2002). Carbon Nanotubes: Past, Present, and Future. *Physica B: Condensed Matter*, Vol. 323, No. 1-4, 1-5.

[18] Dresselhaus, M. S., P. C. Eklund (2000). Phonons in Carbon Nanotubes. *Advances in Physics*, Vol. 49, No. 6, 705-814.

[19] Hone, J., M. Whitney, A. Zettl (1999). Thermal Conductivity of Single-Walled Carbon Nanotubes. *Synthetic Metals*, Vol. 103, No. 1-3, 2498-2499.

[20] Berber, S., Y. Kwon, D. Tomanek (2000). Unusually High Thermal Conductivity of Carbon Nanotubes. *Physical Review Letters*, Vol. 84, No. 20, 4613-4616.

[21] Hone, J., M. C. Llaguno, M. J. Biercuk, A. T. Johnson, B. Batlogg, Z. Benes, J. E. Fischer (2002). Thermal Properties of Carbon Nanotubes and Nanotube-Based Materials. *Applied Physics A: Materials Science and Processing*, Vol. 74, No. 3, 339-343.

[22] Fujii, M., X. Zhang, H. Xie, H. Ago, K. Takahashi, T. Ikuta, H. Abe, T. Shimizu (2005). Measuring the Thermal Conductivity of a Single Carbon Nanotube. *Physical Review Letters*, Vol. 95, No. 6, 1-4.

[23] Incropera, F. P., D. P. Dewitt (2002). *Fundamentals of Heat and Mass Transfer 5th Edition*, John Wiley & Sons, New York, 496.

[24] Fuchs, K. (1938). The Conductivity of Thin Metallic Films According to the Electron Theory of Metals. *Proceedings of Cambridge Philosophical Society*, Vol. 34, 100-108.

[25] Sondheimer, E. H. (1952). The Mean Free Path of Electrons in Metals. *Advances in Physics*, Vol. 1, 1-42.

[26] Yu, C., W. Jang, T. Hanrath, D. Kim, Z. Yao, B. Korgel, L. Shi, Z. L. Wang, D. Li, A. Majumdar (2003). Thermal and Thermoelectric Measurements of Low Dimensional Nanostructures. *Proceedings of the ASME Summer Heat Transfer Conference*, Vol. 1, 77-82.

[27] Shi, L., D. Li, C. Yu, W. Jang, D. Kim, Z. Yao, P. Kim, A. Majumdar (2003). Measuring Thermal and Thermoelectric Properties of One-Dimensional Nanostructures Using a Microfabricated Device. *Journal of Heat Transfer*, Vol. 125, No. 5, 881-888.

[28] Choi, T., D. Poulikakos, J. Tharian, U. Sennhauser (2006). Measurement of the Thermal Conductivity of Individual Carbon Nanotubes by the Four-Point Three-ω Method. *Nano Letters*, Vol. 6, No. 8, 1589-1593.

[29] Jakaboski, B. E., Y. Joshi, M. Rightley (2004). Forced Convection in a Microchannel Heat Sink Using Carbon Nanotubes for Heat Transfer Enhancement. *Proceedings of the ASME Heat Transfer Division - 2004*, Vol. 375, No. 2, 227-233.

[30] Mo, Z., J. Anderson, J. Liu (2004). Integrating Nano Carbontubes with Microchannel Cooler. *Proceedings of the Sixth IEEE CPMT Conference on High*

Density Microsystem Design and Packaging and Component Failure Analysis, 373-376.

[31] Mo, Z., R. Morjan, J. Anderson, E. E. B. Campbell, J. Liu (2005). Integrated Nanotube Microcooler for Microelectronics Applications. *Proceedings - 55th Electronic Components and Technology Conference*, Vol. 1, 51-54.

[32] Gjerde, K., T. Schurmann, K. B. K. Teo, M. Aono, W. I. Milne P. Boggild (2005). Functionalisation of Microfluidic Channels with In Situ Grown Carbon Nanotubes. *Materials Research Society Symposium Proceedings*, *Micro- and Nanosystems - Materials and Devices*, Vol. 872, 371-375.

[33] Joseph, P. C. Cottin-Bizonne, J. M. Benoit, C. Ybert, C. Journet, P. Tabeling, L. Bocquet (2006). Slippage of Water Past Superhydrophobic Carbon Nanotube Forests in Microchannels. *Physical Review Letters*, Vol. 97, No. 15, 156104-1 – 156104-4.

[34] Stadermann, M. A., D. McBrady, B. Dick, V. R. Reid, A. Noy, R. E. Synovec, O. Bakajin (2006). Ultrafast Gas Chromatography on Single-Wall Carbon Nanotube Stationary Phases in Microfabricated Channels. *Analytical Chemistry*, Vol. 78, No. 16, 5639-5644.

[35] Shah, R. K., and A.L. London (1978). *Laminar Flow Forced Convection in Ducts*, Academic, Press, New York.

[36] Incropera, F. P. (1999). *Liquid Cooling of Electronic Devices by Single-Phase Convection*, A. Bar-Cohen and A. D. Kraus, Eds., Wiley-Interscience, New York, 69-86, 151-160.

[37] Moffat, R. J. (1985). Using Uncertainty Analysis in the Planning of an Experiment. *Journal of Fluids Engineering*, Vol. 107, No. 2, 173-178.

[38] Moffat, R. J. (1982). Contributions to the Theory of Single-Sample Uncertainty Analysis. *Journal of Fluids Engineering*, Vol. 104, No. 2, 250-260.

[39] Abernethy, R. B., R. P. Benedict, R. B. Dowdell (1985). ASME Measurement Uncertainty. *Journal of Fluids Engineering*, Vol. 107, No. 2, 161-163.

[40] Kline, S. J. (1985). The Purposes of Uncertainty Analysis. *Journal of Fluids Engineering*, Vol. 107, No. 2, 153-160.

[41] Kline, S. J., and F. A. McClintock (1953). Describing Uncertainties in Single-Sample Experiments. *Mechanical Engineering*, Vol. 75, No. 1, 3-8.

[42] Eisenhart, C. (1968). Expression of the Uncertainties of Final Results. *Science*, Vol. 160, No. 3833, 1201-1204.

[43] Phillips, R.J., L. R. Glicksman, and R. Larson (1988). Forced-Convection, Liquid-Cooled, Microchannel Heat Sinks for High-Power-Density Microelectronics. *Cooling Technology for Electronic Equipment*, W. Aung, Ed., Hemisphere, New York, 295-316.

[44] Phillips, R. J. (1990). Microchannel Heat Sinks. *Advances in Thermal Modeling of Electronic Components and Systems*, A. Bar-Cohen and A. D. Kraus, Eds., Vol. 2, ASME Press, New York, 109-184.

[45] Hu, X. J., M. A. Panzer, K. E. Goodson (2007). Infrared Microscopy Thermal Characterization of Opposing Carbon Nanotube Arrays. *Journal of Heat Transfer*, Vol. 129, No. 1, 91-93.

[46] Huxtable, S. T., D. G. Cahill, S. Shenogin, L. Xue, R. Ozisik, P. Barone, M. Usrey, M. S. Strano, G. Siddons, M. Shim, P. Keblinski (2003). Interfacial Heat Flow in Carbon Nanotube Suspensions. *Nature Materials*, Vol. 2, No. 11, 731-734.

[47] Zhimin, W. and C. K. Fah (1997). The Optimum Thermal Design of Microchannel Heat Sinks. *Proceedings of the Electronic Packaging Technology Conference*, 123-129.

[48] Wei, Xiaojin (2004). Stacked Microchannel Heat Sinks for Liquid Cooling of Microelectronics Devices. Georgia Institute of Technology, Atlanta, Georgia, USA.

[49] Patil, V. A., V. Narayanan (2006). Spatially Resolved Temperature Measurement in Microchannels. *Microfluidics and Nanofluidics*, Vol. 2, No. 4, 291-300.

[50] Cherkasova A., J. Shan (2006). Thermal Conductivity Enhancement of Nanofluids. *NATO Science Series II: Mathematics, Physics and Chemistry*, V. N. Popov and P. Lambin, Eds., Vol. 222, Springer Netherlands, Dordrecht, 235-236.

[51] Chang, F.-M., H.-K. Tsao (2007). Drag Reduction in Electro-Osmosis of Polymer Solutions. *Applied Physics Letters*, Vol. 90, No. 19, 194105.

[52] Ahn, H.S., V. Sathyamurthi, N. Sinha, S. Lau, D. Banerjee (2006). Boiling Experiments on Vertically Aligned Carbon Nanotubes and Using Surface Micromachined Thin Film Thermocouple (TFT). *AIAA/ASME Joint Thermophysics and Heat Transfer Conference Proceedings*, 84-93.

[53] Jo, B., L. M. Van Lerberghe, K. M. Motsegood, D. J. Beebe (2000). Three-dimensional Micro-channel Fabrication in Polydimethylsiloxane (PDMS) Elastomer. *Journal of Microelectromechanical Systems*, Vol. 9, No. 1, 76-81.